Model Reduction for Nonlinear Dynamical Systems with Parametric Uncertainties

by

Yuxiang Beckett Zhou

Bachelor of Applied Science, Engineering Science, University of Toronto (2010)

Submitted to the Department of Aeronautics and Astronautics in partial fulfillment of the requirements for the degree of

Master of Science in Aeronautics and Astronautics

at the

MASSACHUSETTS INSTITUTE OF TECHNOLOGY

September 2012

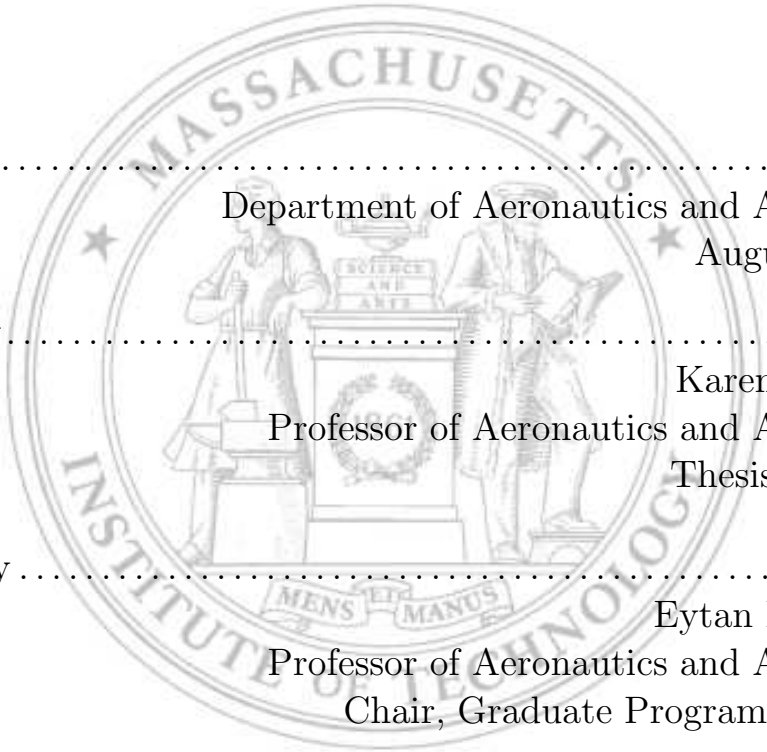

Author .....
Department of Aeronautics and Astronautics
August 23, 2012

Certified by .....
Karen E. Willcox
Professor of Aeronautics and Astronautics
Thesis Supervisor

Accepted by .....
Eytan H. Modiano
Professor of Aeronautics and Astronautics
Chair, Graduate Program Committee

Model Reduction for Nonlinear Dynamical Systems with Parametric Uncertainties

by

Yuxiang Beckett Zhou

Submitted to the Department of Aeronautics and Astronautics
on August 23, 2012, in partial fulfillment of the
requirements for the degree of
Master of Science in Aeronautics and Astronautics

Abstract

Nonlinear dynamical systems are known to be sensitive to input parameters. In this thesis, we apply model order reduction to an important class of such systems — one which exhibits limit cycle oscillations (LCOs) and Hopf-bifurcations. High-fidelity simulations for systems with LCOs are computationally intensive, precluding probabilistic analyses of these systems with uncertainties in the input parameters.

In this thesis, we employ a projection-based model redcution approach, in which the proper orthogonal decomposition (POD) is used to derive the reduced basis while the discrete empirical interpolation method (DEIM) is employed to approximate the nonlinear term such that the repeated online evaluations of the reduced-order model (ROM) is independent of the full-order model (FOM) dimension.

In problems where vastly different magnitudes exist in the unknowns variables, the original POD-DEIM approach results in large error in the smaller variables. In unsteady simulations, such error quickly accumulates over time, significantly reducing the accuracy of the ROM. The interpolatory nature of the DEIM also limits its accuracy in approximating highly oscillatory nonlinear terms. In this work, modifications to the existing methodology are proposed whereby scalar-valued POD modes are used in each variable of the state and the nonlinear term, and the pure interpolation of the DEIM approximation is also replaced by a regression via over-sampling of the nonlinear term. The modified methodology is applied to two nonlinear dynamical problems: a reacting flow model of a tubular reactor and an aeroelastic model of a cantilevered plate, both of which exhibit LCO and Hopf-bifurcation. Results indicate that in situations where the efficiency of the original POD-DEIM ROM is compromised by disparate magnitudes in unknown variables or by the need to include large sets of interpolation points, the modified POD-DEIM ROM accurately predicts the system responses in a small fraction of the FOM computational time.

Thesis Supervisor: Karen E. Willcox
Title: Professor of Aeronautics and Astronautics

Acknowledgments

First and foremost, I would like to express my sincere gratidude towards my advisor, Professor Karen Willcox. Over the past two years at MIT, she has provided me with continuous guidance, support and encouragement. I thank her for her kindness, understanding and generosity. It has been an honour and a privilege to work with a top-notch researcher in the model reduction community like her.

The full-order code of the aeroelastic test case in this work was provided by Dr. Bret Stanford of the Wright-Patterson Air Force Research Laboratory. I am deeply indebted to him for his invaluable assistance over the past two years. Thank you Bret, for helping me set up and modify so many different versions of the full-order code throughout this research and tirelessly answering all my questions on aeroelasticity.

Dr. Ngoc-Cuong Nguyen, thank you for sharing with me your expertise in reduced-order modeling and providing me with so many insightful suggestions for this research. I am also very grateful for all the helpful discussions I've had with Chad Lieberman and Dr. Tarek El Moselhy.

My graduate school experience has been enriched by a half-year academic visit at the University of Cambridge. I would like to thank Prof. Karen Willcox for supporting me on this visit financially and my host at Cambridge Dr. Jerome Jarrett for his hospitality.

I would also like to thank the fellow members of the ACDL, particularly Xun Huan, Dr. David Lazzara, Dr. Andrew March and Leo Ng for being such good pals. The past two years, as the life should be, has been full of ups and downs. Dr. Andrew March, thank you so much for helping me pick myself up when I hit the bottom. Thanks also goes to Nikola and Dorian of the GTL for the 'depressurizing beers' on Saturday nights.

To my parents Jimmy and Susan, thank you for your unconditional love and continuous support on my academic endeavour. Thank you for telling me that you were still very proud of me and reminding me what I came to MIT for during the darkest hours of my journey.

To my most faithful companion Olcia, my life outside of research would not have been so interesting and adventurous without you. Thank you for being there with me through this whole journey.

To three of my best friends Alexei, Ivana and Jovan, you know what they say: 'good friends are like stars — you don't always see them, but you know they're always there'.

To Sojourn Wei and Sarah Zhan, I was nearly 'burnt out' towards the very end of this journey, but our reunion in NYC reminded me of the old days. I suddenly remembered how far I have come from the way I was 10 years ago and how much I must excel, for myself and for the people who care about me. Thank you for that much needed extra shot of strength.

To everyone who has supported me in various ways over the past two years, I dedicate this thesis to you.

Contents

List of Figures

List of Tables

Chapter 1

Introduction

1.1 Motivation

It is known that the outputs or responses of many systems in science and engineering are sensitive to slight variations in input parameters such as initial conditions, system geometries and boundary forcing. A simplified example with viscous Burgers' equation shown by Xiu in [87] demonstrates exactly such sensitivity: a 10% variation in inflow boundary condition results in an $O(1)$ change in the position of the final steady-state solution.

Such sensitivities are particularly prevalent in nonlinear dynamical systems. An important class of such systems is one that exhibits limit cycle oscillations (LCO), in which the nonlinear mechanisms in the system 'arrests' the amplifying effect caused by initial disturbances, bringing it to a self-sustained oscillations. Many engineering systems exhibit LCO — a good representative in the area of aerospace engineering is the aeroelastic response of an airplane wing operating above its flutter speed subject to an initial disturbance. LCO has been experienced on both military aircraft such as F-16 and F-18 fighter jets [19] as well as civilian aircraft such as the Airbus passenger jets [30]. The 'initial disturbance' could be induced by a gust encounter or a sudden maneuver. The ensuing growth of vibrational amplitude is attenuated by the aerodynamic and/or structural nonlinearity, resulting in the wing structure oscillating in a sinusoidal manner at a finite amplitude. Even though the amplitude

of such oscillation may not be large enough to cause catastrophic structural failure, long-term exposure to LCO leads to structural fatigue which reduces the useful life of the structure [33]. LCO also affects the operation of the aircraft in that once developed, it tends to persist until the operating conditions are substantially altered. Moreover, LCO-induced motion not only results in a reduction in vehicle performance, but also affects the performance of the aircrew from the human-factors perspective [19]. Therefore, aeroelastic LCOs are generally considered an adverse effect in flight and must be avoided in the design process. To that end, both LCO amplitude and the location within the flight envelope where the onset of the LCO occurs must be accurately predicted.

However, this is not an easy task since aeroelastic LCO response is known to be extremely sensitive to the operating conditions as well as the geometric and material properties of the wing. Variations in structural parameters such as the thickness, bending and torsional stiffness of the wing result in variations in the natural frequencies of the wing structure. As noted by the studies performed by Thomas et al. on F-16 fighter jets in transonic flight [80], small changes in natural frequencies can lead to substantial changes in the LCO amplitude and more importantly, a shift in the Hopf bifurcation point manifesting in a reduction in flutter onset speed and altitude. This study also observed a significant reduction in aircraft performance due to LCO when slight modifications are made to the wingtip. Tang and Dowell [78] investigated numerically the aeroelastic response of a delta wing in subsonic flight and found strong effect of the angle of attack (AOA) on both the flutter boundary and LCO amplitude. This finding was confirmed by experimental studies performed by Bunton and Denegri [19]. Variations in the amount of control surface freeplay also affects the LCO response – two identical aircraft flying through the same trajectory may experience different magnitudes of LCO depending on the amount of freeplay as noted by [33]. Due to the nonlinear nature of the LCO response, they are typically not observed during wind tunnel tests (as the test prototypes are typically designed based on linear aeroelastic concepts), only to be unveiled through extensive flight tests which are both costly and dangerous [34, 31]. The safe flight envelopes thus

established are not permanent however, as each modification in aircraft configuration invalidates the previously acquired flutter and LCO information, requiring the flight tests to be repeated. It is evident from these studies that it is essential to incorporate the variations or uncertainties in the system parameters not only in the initial design process of an aerial vehicle but also throughout its service life.

This however, proves to be a tremendous undertaking. As noted by many researchers, simulations of aeroelastic LCO can be computationally expenesive even in the deterministic setting due to the need to solve large systems of nonlinear equations in both the fluid and structural domain at each time step [34, 31, 66]. In addition, many time steps are typically required in an unsteady simulation before the limit cycle fully develops. This is especially true for systems with configurations close to the Hopf bifurcation point where the convergence towards a stable limit cycle can be extremely slow. This challenge is magnified when the system is studied under multi-query uncertainty quantification (UQ) or optimization settings as noted by a number of studies such as [12, 88, 2].

As a result, aeronautical designs that accurately account for LCO are rare in literature. Often in practice, an empirical flutter safety margin is imposed. All U.S. military aircraft must satisfy a 15% flutter margin, a requirement dating back to the 1960s [66]. For civilian aircraft, a 20% flutter margin must be demonstrated, as imposed by the Federal Aviation Administration (FAA) [7, 68]. Such conservatism is testimonial to our lack of confidence in the level of fidelity of our model and inability to adequately account for the uncertain environment in which the aerial vehicle will operate. In the design and optimization of novel and unconventional aerial vehicles with superior fuel-efficiency (i.e. light weight), such constraint will likely drive the design process. A rational and reliable method to adjust such constraint will likely result in substantial gains in performance of the new design. Therefore, efficient computational methods are urgently needed to enable aeroelastic designs under uncertainty.

The above exposition focuses on the LCO phenomenon that occurs in the aeronautical context. However, LCO also exists in many other nonlinear dynamical systems.

Another area where LCOs are frequently observed is chemically reacting flows [16, 43]. It is often of interest to predict the maximum oscillatory temperature attained at certain locations within the reactor (for example, the exit) under different flow and reaction parameters. The LCO responses of reacting flows are known to be sensitive to these input parameters. Hence all the computational difficulties previously discussed in the aeroelastic LCO also exist in the case of reacting flows, requiring efficient numerical methods to accelerate multi-query or time-sensitive tasks such as optimal or real-time control of the reaction.

To alleviate the aforementioned computational burdens, model order reduction techniques may be applied to construct efficient low-dimensional approximations of the large-scale systems. In this work, we apply reduced order modeling to the two particular nonlinear dynamical applications discussed above: aeroelastic and reacting flow LCOs with the ultimate aim of accelerating the process of design and control.

Note that this work focuses on problems exhibiting LCO as it is a good representative of nonlinear dynamical responses that include important dynamics such as autonomous solutions and Hopf bifurcations which are sensitive to input parameters. It should be stressed however, that the methods presented in this work are applicable to general nonlinear dynamical problems.

1.2 Review of Existing Model Reduction Techniques

1.2.1 Projection-Based Model Reduction

In this work, we focus on projection-based reduced-order models (ROM) in which the governing equations of the system are projected onto a low-dimensional subspace spanned by a small set of basis functions via Galerkin projection. It has been shown that in many cases, most of the system information and characteristics can be efficiently represented by linear combinations of only a small number of basis functions, making it possible to accurately capture the input-output relationship of a large-scale full-order model (FOM) via a reduced system with significantly fewer unknowns.

The first essential ingredient of all projection-based model reduction techniques is the construction of the basis functions. To that end, a number of methods have been developed such as balanced truncation [57, 58, 42], Krylov-subspace methods [35, 38, 41], reduced-basis methods [63, 64] and proper orthogonal decomposition (POD) [73, 46]. Originally, the Krylov-subspace methods and balanced truncation were developed for linear time-invariant problems by the controls community, although recent years have seen much progress on the extensions of these methods to nonlinear problems, mostly in nonlinear circuits [14, 28].

Both reduced-basis methods and POD are 'snapshot-based' methods; that is, the bases are derived from a set of the state solutions (the snapshots) obtained by solving the FOM at selected points in its input parameter space. For the reduced-basis method, the particular set of parameters at which the solution snapshots are generated is obtained via a greedy algorithm in which the snapshots are adaptively added to the reduced basis so as to minimize the maximum error bound of the output. The snapshots are then orthonormalized using a Gram-Schmidt process and used directly as reduced basis. Much work has been done on this method, most notably in [65, 56, 85, 84].

As opposed to using the snapshot set as the reduced basis directly, POD (also knowns as the Karhunen-Lòeve expansion) [73, 46] applies singular value decomposition (SVD) to the snapshot set and retain the dominant left singular vectors corresponding to the largest singular values as reduced basis. The basis thus extracted is optimal in the sense that, for the same number of basis functions, no other bases can represent the given snapshot set with lower least-squares error than the POD basis. POD coupled with Galerkin projection (henceforth referred to as the 'POD-Galerkin' approach) has been applied successfully to many large-scale model reduction problems. In this thesis, the construction of ROM will be based on the POD-Galerkin approach.

There are a number of factors that affect the effectiveness of POD-based model reduction, first of which is the efficient sampling of the parameter space. Since it derives the basis vectors from a set of snapshots, the quality of the POD reduced-

order model depends strongly on the snapshots collected in the sampling process. Snapshot sets must contain sufficient information about the essential dynamics of the FOM. Primitive sampling schemes such as random sampling and uniform sampling are not always optimal as they may miss important regions of the parameter space and become too computationally expensive for problems with high input parameter dimensions. To address this issue, a number of more sophisticated sampling techniques have been developed in the model reduction community. Bui-Thanh et al. [18] proposed a model-constrained sampling technique in which the computations for the locations of the samples in the parameter space are formulated as an optimization problem. This method is very similar to the greedy sampling method developed by the researchers in the reduced-basis community [65, 56, 85, 84] and has been shown to scale well to problems with large number of input parameters. A number of advanced sampling methods (some specifically tailored towards certain applications) are mentioned in the review by [36]. For problems with small numbers of input parameters, uniform sampling remains a popular method of generating snapshot sets in many applications. For the work in this thesis, we will employ such technique in sampling. However, we stress that it is possible to combine the model reduction methodology presented in this thesis with one of the more advanced sampling techniques discussed above to obtain more accurate ROMs.

The second factor, which is more relevant to the particular type of problems considered in this work is the efficient treatment of nonlinearities. Reduced-basis and POD methods have been successfully applied to PDEs that are at most quadratically nonlinear in state, such as the Euler and Navier-Stokes equations [51, 69, 79, 15], since the special structures of the nonlinear terms in these equations allows for precomputations of reduced matrices, resulting in ROMs whose evaluations are independent of the dimensions of the FOM. However, for general non-polynomial nonlinearities, projection-based model reduction methods become inefficient and the attainable speed-up over the FOM is significantly reduced. This is due to the fact that to compute the reduced nonlinear term, one must first reconstruct the full-order state solution from the basis vectors, evaluate the full-order nonlinear term before pro-

jecting it onto a reduced subspace again. All of these operations are dependent on the dimension of the FOM. Similar inefficiency exists in the formation of reduced Jacobian. Therefore, for problems with general nonlinear terms, although the POD-Galerkin approach may result in ROMs with significantly reduced dimensions, the computational cost of evaluating the ROMs is still a function of the FOM dimension. Such inefficiencies have been noted by many researchers [8, 61, 37, 24] who have deviced a number of techniques to address the nonlinearity issue in the projection-based model reductions. A more detailed review of some of these techniques will be provided in the next section.

Despite of these challenges, model reduction employing the POD-Galerkin approach has been applied to many areas of computational engineering such as fluid mechanics and aerodynamics [51, 69, 79], structural mechanics [52, 49], circuit analysis [83, 44], reactive flows [74, 72], optimal control [50, 13] and even option pricing [26].

In the particular context of the aeroelastic applications relevant to this thesis, [22] and [86] applied POD to linearized aerodynamic and structural models to investigate the effects of compressor blade mistuning in turbomachinery. Dowell et al. [34] applied POD to model the LCO of an airfoil with plunging and pitching degrees of freedom and control surface freeplay in transonic flow modeled by Euler equations. POD-based model reduction is applied to the aerodynamic domain only, in which the special structure of the nonlinearity in the governing equations allows the efficiency of the POD-Galerkin ROM to be preserved. Both flutter boundary and LCO amplitudes at different operating conditions were predicted using ROM. In this study, accuracy and speed-up of the ROM with respect to the FOM was not presented. The ROM results were qualitatively found to be in good agreement with experimental results. More recently, the POD-Galerkin approach has also been applied to model the aeroealstic response of complete fighter jet configurations in [54] and [1], where ROM adaptation method based on interpolation in a tangent space to a Grassmann manifold was developed to 'correct' the precomputed ROMs to new operating conditions. However, since both the aerodynamic and structural models

were linearized about some equilibrium points, nonlinearities that trouble the POD-Galerkin method were not present. This also means aeroelastic LCO behaviors could not be modeled by the ROM. Computational speed-up between factors of 10 and 16 were reported. It is particularly worthy to note in these works that the results of the ROMs, constructed on linearized aeroelastic models, were not only compared to their FOM counterparts (for which the agreement was found to be excellent), but were also compared to the a FOM consisting of a *fully nonlinear* aero-structural model. Significant discrepancies were reported. Certainly, it is not fair to compare the FOM and ROM constructed based on models with different levels of fidelity. However, this comparison does serve to highlight the need to have a ROM that can be computed efficiently in the presence of nonlinearities such that these important effects can be adequately modeled. Beran et al. applied the POD-Galerkin method to model the aeroelastic LCO response of nonlinear panels in transonic and supersonic flow regimes [11, 55]. The structural nonlinearity was modeled by the von Kármán strain. The FOM with over 65,000 degrees of freedom was adequately represented using a ROM with only 10 basis vectors. Although this corresponds to a 4 order-of-magnitude reduction in system dimension, the speed-up achieved by the ROM is only a factor of 4. In the design under uncertainties context, Stanford and Beran [75] applied POD in conjunction with spectral element method in time to accelerate the realiability-based optimization of a cantilevered nonlinear plate in supersonic flow. As in [11] and [55], although the POD-based method succeeded in accelerating the model evaluations and hence the optimization process, the true efficiency of the ROM was not realized due to the lack of specialized methods to handle the nonlinearities.

1.2.2 Treatments for Nonlinearities

As mentioned in the previous section, the degradation of efficiency that the POD-Galerkin approach suffers from is due to computational costs of forming the reduced nonlinear term and Jacobian being functions of the FOM dimension rather than being proporitional to the number of reduced variables. This deficiency has been noted by a number of researchers. Specifically, in [24] and [37] detailed analysis of operation

counts are presented and in [24] it has been shown that vanilla POD-Galerkin can be even slower than the FOM due to such computations at each iteration of each time step. To overcome this computational bottleneck, a number of procedures have been developed to recover the efficiency of projection-based model reductions for nonlinear problems.

Missing Point Estimation (MPE) was developed by Astrid et al. in [6] to improve the efficiency of the POD-Galerkin model reduction of a nonlinear computational fluid dynamic (CFD) model for a glass melting feeder. The basic idea behind MPE is to select a subset of semi-discretized governing equations corresponding to a number of grid points and apply the Galerkin projections for these equations only. In particular, a restricted POD basis is formed by extracting the rows of the standard POD basis vectors corresponding to the selected grid points. Subsequently, the subset of governing equations are projected onto the subspace spanned by these restricted POD basis vectors. An key ingredient is then the choice of the aforementioned grid points. To that end, two algorithms are presented in [6], based on the criterion of limiting the condition number growth of the restricted POD basis matrix. Via such construction, the formations of the computationally expensive full-order nonlinear term and Jacobian as well as their respective projections to the reduced forms at each time step can be avoided. Aside from the application considered in [6] and related publications such as [5] and [4], the MPE technique has also been applied to model electrical circuits [83], subsurface flow [20] and steady aerodynamics [82].

Other techniques aim to provide efficient approximations specifically for the nonlinear terms. For weakly nonlinear problems, an effective approach is the trajectory piecewise-linear (TPWL) method by Rewienski and White [67], in which the nonlinear function is approximated by a piecewise-linear function obtained by linearizing the system at selected points along its trajectory. This method has been applied in conjunction with the POD-Galerkin projection to many problems in nonlinear circuit simulations [9, 83]. However, for highly nonlinear problems, it is difficult to approximate the nonlinear term accuractely with a piecewise-linear representation without involving a large number linearized models along the trajectory. Furthermore, the se-

lections of the training trajectories and linearization points remain an ad-hoc process [39].

It is also possible to approximate the nonlinear term by a linear combination of its basis vectors for which the expansion coefficients are determined using a small set of interpolation points. This is the basic idea behind the methods such as the Empirical Interpolation Method (EIM) [8] and the Best Point Interpolation Method (BPIM) [62]. The set of basis vectors for the nonlinear terms can be generated using the same method as the state basis. By using a small number of interpolation points, the nonlinear term only needs to be evaluated over a subset of spatial grid points, allowing the ROM to recover its efficiency. EIM and BPIM have been developed for the same purpose but they differ in the algorithm with which the locations of the interpolation points (interpolation indices) are selected. In EIM, a 'greedy' selection process is employed to iteratively build the set of interpolation indices in such a way that the n-th interpolation point is placed at the spatial location where the approximation error of the n-th basis vector using the first $n-1$ interpolation points and basis vectors is the greatest. In constrast, BPIM builds the interpolation indices by solving an n-dimensional optimization problem to minimize the least-squares error between each of the collected nonlinear snapshots and their approximation using n interpolation points. Therefore, these n points thus obtained are the 'best' interpolation points to minimize the approximation error over all of the snapshots. It should be noted that although the BPIM method results in a set of points that are 'optimal', the nonlinear constrained optimization problem that must be solved makes it significantly more expensive to compute than the sub-optimal greedy procedure in EIM, with only marginal improvement in approximation error, as reported in [37, 8]. Both EIM and BPIM have been applied to many problems governed by nonlinear PDEs, such as [77, 40, 61]. Galbally et al. [37] applied both POD-EIM and POD-BPIM approaches to Bayesian inference in a highly nonlinear combustion problem governed by a convection-diffusion-reaction (CDR) PDE. Very recently, the same POD-BPIM framework was used by Kalashnikova and Barone in [47] to construct ROM for a nonlinear time-dependent CDR model of a tubular reactor known to exhibit bifurcation

and LCO – the same application as the first model problem considered in this thesis.

The discrete variant of the EIM, the Discrete Empirical Interpolation Method (DEIM) was introduced by Chaturantabut and Sorensen in [24] to be used with the POD-Galerkin approach on the semi-discretized systems. This is in contrast to the EIM and BPIM, whose formulations are based on a continuous framework, although all three are implemented in a fully discrete setting. The POD-DEIM model reduction methodology has been successfully applied to many engineering problems such as multi-phase flow [23], neuron modeling [48], reactive flow [17], and MEMS switch modeling [45]. Note that since DEIM operates at the semi-discrete level, it can be more easily applied to existing FOM codes than its continuous counterpart, the EIM. For this adaptability, we opt to use the POD-DEIM framework in this thesis.

1.3 Thesis Scope and Objectives

In this thesis, we study model reductions using the POD-DEIM methodology for nonlinear dynamical systems. A particular focus is placed on an important class of such systems involving LCOs as it is a good representative of nonlinear dynamical responses that includes complex dynamics such as autonomous solutions and Hopf bifurcations which are sensitive to input parameters.

In most cases, LCOs are typically caused by nonlinear interactions amongst multiple unknown variables in the problem. Therefore, the models for problems with LCO are typically vector-valued PDEs. In many applications, it is not always possible to nondimensionalize the problem such that all the unknown variables are on the same order of magnitude. Furthermore, existing FOM codes are not always nondimensionalized. As shown in the following chapters, the relative magnitudes of the different unknown variables have a strong effect on the accuracy of the standard POD-based ROMs using 'unified' modes containing all unknown variables. An obvious solution for this issue is to use individual POD basis for each unknown variable. However whether this will lead to an unacceptable increase in the number of DEIM points is an open question.

In addition, POD-DEIM has so far only been applied to PDEs with nonlinear terms that have 'componentwise' dependence on the state as referred to by the original paper [24]. In other words, the nonlinear term at the i-th grid point is only a function of the state at that point. There exists a wide range of problems, particularly in structural mechanics where the nonlinear term at each grid point may depend on the state solution at multiple nodes in its neighourhood. The number of state solutions that must be reconstructed at each time step for the evaluation of the nonlinear term may be significantly greater than the number of DEIM interpolation points, due to the nodal connectivity. For aeroelastic LCO problems having nonlinear structural terms with such 'noncomponentwise' dependence on the state, whether the POD-DEIM can still be used for efficient model reduction remains to be seen.

Finally, the highly dynamic and oscillatory nature of many LCO problems pose additional difficulties in approximating the nonlinear term using an interpolatory method such as DEIM. Can POD-DEIM be modified to handle such challenging problems?

All of the above are important research questions from the methodological standpoint that must be addressed in order to improve the versatility and efficiency of the POD-DEIM methodology for nonlinear dynamical systems.

From the applications standpoint, as discussed in Section 1.1, considerations for aeroelastic LCO have a significant influence in the design and operation of aerial vehicles. However, aircraft designs that accurately account for LCO are rare due to their computational costs and sensitivities to model parameteres. Therefore, it is expected that ROM will serve as an enabling technology towards UQ of aeroelastic LCO as well as designs of safer and more efficient aerial vehicles. The works of Stanford and Beran in [75] and Beran et al. in [11] and [55] have already made solid steps in this direction by applying POD-based ROM to accelerate the analysis and design for aerostructural systems exhibiting LCOs. As noted previously, these works employ the vanilla POD-Galerkin approach which do not fully realize the efficiency of the ROM in presence of nonlinearity. It is expected that the computational speed-up can be significantly improved using the POD-DEIM methodology.

In [24] where the methodology was originally proposed, POD-DEIM was applied to model the LCO response in the FitzHugh-Nagumo system with *fixed* parameters. By applying the POD-DEIM to the aeroelastic model problem with multiple uncertain input parameters, we aim to demonstrate the efficacy of the method for complex uncertain nonlinear dynamics involving LCOs and bifurcations.

In summary, the objectives of this thesis are to improve the POD-DEIM methodology to address more challenging nonlinear dynamical problems with following features:

- Vector-valued PDEs with different orders of magnitudes in each unknown variable
- Noncomponentwise dependence of nonlinear terms on state
- Complicated nonlinear terms that are difficult to approximate using the existing DEIM approach

In particular, we demonstrate the efficacy of the improved POD-DEIM methodology in handling complex uncertain nonlinear dynamics via two model problems: a CDR model of a tubular reactor and an aeroelastic model of a cantilevered wing, both of which possess Hopf bifurcation and exhibit LCO behavior.

1.4 Thesis Outline

The remainder of this thesis is organized as follows. In Chapter 2, the problem formulation of the current POD-DEIM model reduction methodology is first presented along with an online-offline computational procedure. Then a modified POD-DEIM methodology is proposed combining the ideas of 'scalar-valued' POD modes and oversampling of DEIM points. In Chapter 3, the original POD-DEIM methodology is first demonstrated for a 1-D CDR model of a tubular reactor with a variable Damköhler number and equal magnitudes between the two unknown variables. The difference in magnitudes is then increased while maintaining the same LCO response, and the

performances of the original and modified POD-DEIM methods are compared. The purpose of this chapter is to illustrate how to apply both POD-DEIM methodologies to a simple problem and investigate their relative performances for vector-valued PDEs with large difference in magnitudes between different unknown variables. It also demonstrates the ability of the POD-DEIM approach in characterizing uncertain dynamics (by accurately predicting the bifurcation diagram, for example) with limited number of samples. In Chapter 4, the modified POD-DEIM methodology is applied to a more challenging problem involving the LCO response of a nonlinear plate in supersonic flow. ROMs constructed using POD-DEIM are applied to enable efficient computations of both the LCO response and the flutter boundary. Up to three uncertain input parameters are considered in this problem. Finally, the conclusions and recommendations for future work are presented in Chapter 5.

Chapter 2

Nonlinear Model Reduction using Proper Orthogonal Decomposition and Discrete Empirical Interpolation Method

This chapter presents a projection-based model reduction methodology based on the proper orthogonal decomposition (POD) and the discrete empirical interpolation method (DEIM), for nonlinear dynamical systems with parametric uncertainties. Section 2.1.1 presents the model reduction using Galerkin projection and the POD method for the generation of reduced basis vectors. The inefficiency of the POD-Galerkin method for nonlinear problems is also discussed at the end of this section. To address this issue, Section 2.1.2 introduces the DEIM technique for the reduction of nonlinear terms. An efficient offline-online model reduction procedure using the POD-DEIM methodology is presented in Section 2.1.3. To address the challenges discussed in Section 1.3 (namely, vector-valued PDEs having highly oscillatory nonlinear terms with noncomponentwise dependence on the state), two modifications to the current POD-DEIM methodology are introduced in Section 2.2. The use of scalar-valued POD modes is discussed in Section 2.2.1 and the DEIM approximation

with over-sampling is presented in Section 2.2.2.

2.1 Problem Formulation

Consider a dynamical system governed by a time-dependent nonlinear PDE with parametric uncertainty. Its spatial discretization leads to to the following system of N nonlinear ODEs:

$$\frac{d\mathbf{u}(t;\boldsymbol{\mu})}{dt} = \mathbf{R}(\mathbf{u}(t;\boldsymbol{\mu}), t; \boldsymbol{\mu}) \tag{2.1}$$

with initial conditions

$$\mathbf{u}(t=0;\boldsymbol{\mu}) = \mathbf{u}^0, \tag{2.2}$$

where

$$\mathbf{R}(\mathbf{u}(t;\boldsymbol{\mu}), t; \boldsymbol{\mu}) = \mathbf{A}\mathbf{u}(t;\boldsymbol{\mu}) + \mathbf{f}(\mathbf{u}(t;\boldsymbol{\mu}), t; \boldsymbol{\mu}), \tag{2.3}$$

and $\mathbf{u}^0$ is the initial state, $t \in \mathbb{R}^+$ is the time, $\mathbf{u} \in \mathbb{R}^N$ is the discrete state vector of dimension N, $\boldsymbol{\mu} \in \mathbb{R}^{N_p}$ is the vector of N_p uncertain (input) parameters, $\mathbf{R}(\mathbf{u}, t; \boldsymbol{\mu}) \in \mathbb{R}^N$ is the nonlinear residual, $\mathbf{A} \in \mathbb{R}^{N\times N}$ is a constant matrix arising from the discretization of linear differential operators in space, and $\mathbf{f}(\mathbf{u}, t; \boldsymbol{\mu}) : \mathbb{R}^N \times \mathbb{R}^+ \times \mathbb{R}^{N_p} \mapsto \mathbb{R}^N$ is a nonlinear function of state and input parameters. The Jacobian of the nonlinear residual is:

$$\mathbf{J}(\mathbf{u}(t;\boldsymbol{\mu}), t; \boldsymbol{\mu}) = \frac{\partial \mathbf{R}(\mathbf{u}(t;\boldsymbol{\mu}), t; \boldsymbol{\mu})}{\partial \mathbf{u}} = \mathbf{A} + \mathbf{J}^{\mathbf{f}}(\mathbf{u}(t;\boldsymbol{\mu}), t; \boldsymbol{\mu}), \tag{2.4}$$

where

$$\mathbf{J}^{\mathbf{f}} \equiv \frac{\partial \mathbf{f}}{\partial \mathbf{u}}. \tag{2.5}$$

For a finite difference discretization of a vector-valued PDE, the dimension N is the product of the number spatial grid points (N_x) and the number of unknown variables (N_v), which can be extremely large for high-fidelity simulations. Moreover, for nonlinear dynamical systems, which are the focus of this work, implicit time integration schemes are often used. This leads to a system of nonlinear equations that must be solved at each time step (using Newton's method, for example), requiring the

computationally expensive formation and inversion of the $N \times N$ Jacobian at each sub-iteration. In addition, each forward evaluation of the model may involve many hundreds of time steps before important time-asymptotic system behaviors such as limit cycle oscillations begin to emerge. As a result, performing uncertainty propagation/quantification, which requires the evaluations of many thousands of realizations, is computationally intractable. To alleviate this computational burden, we introduce a projection-based model reduction methodology in the following sections.

2.1.1 Projection-Based Model Reduction via Proper Orthgonal Decomposition (POD)

The first step in deriving the projection-based ROM is to express the state $\mathbf{u}(t;\boldsymbol{\mu})$ by a linear combination of K basis vectors, where $K \ll N$:

$$\mathbf{u}(t;\boldsymbol{\mu}) \approx \sum_{i=0}^{K} \tilde{u}_i(t;\boldsymbol{\mu})\boldsymbol{\phi}_i \tag{2.6}$$

In matrix form:

$$\mathbf{u} \approx \boldsymbol{\Phi}\mathbf{u}_r \tag{2.7}$$

where

$$\boldsymbol{\Phi} = [\boldsymbol{\phi}_1, \boldsymbol{\phi}_2, \ldots, \boldsymbol{\phi}_K] \in \mathbb{R}^{N\times K}, \quad \mathbf{u}_r = [\tilde{u}_1, \tilde{u}_2, \ldots, \tilde{u}_K] \in \mathbb{R}^{K\times 1} \tag{2.8}$$

where $\mathbf{u}_r \in \mathbb{R}^{K\times 1}$ is the 'reduced' state vector or vector of modal amplitudes and $\boldsymbol{\Phi} \in \mathbb{R}^{N\times K}$ is a matrix that contains K orthonormal basis vectors $\{\boldsymbol{\phi}_i\}_{i=1}^{K}$ in its columns. Note that to simplify the notation, we omit t and $\boldsymbol{\mu}$ in (2.7) and from this point on, with the understanding that both $\mathbf{u}$ and $\mathbf{u}_r$ are functions of t and $\boldsymbol{\mu}$. Substituting the expansion (2.7) into the governing equation (2.1):

$$\boldsymbol{\Phi}\frac{d\mathbf{u}_r}{dt} = \mathbf{A}\boldsymbol{\Phi}\mathbf{u}_r + \mathbf{f}(\boldsymbol{\Phi}\mathbf{u}_r, t;\boldsymbol{\mu}) = \mathbf{R}(\boldsymbol{\Phi}\mathbf{u}_r, t;\boldsymbol{\mu}) \tag{2.9}$$

This results in an overdetermined system of N equations and K unknowns. To arrive at a reduced system of K equations, we require the nonlinear residual to

be orthogonal to a left subspace via projection. For Galerkin projection, this left subspace is spanned by the columns of the matrix $\mathbf{\Phi} = \{\boldsymbol{\phi}_i\}_{i=1}^{K}$. That is to say, $\mathbf{\Phi}^T\mathbf{R}(\mathbf{\Phi}\mathbf{u}_r, t; \boldsymbol{\mu}) = 0$. In the specific context of (2.9):

$$\frac{d\mathbf{u}_r}{dt} = \underbrace{\mathbf{\Phi}^T\mathbf{A}\mathbf{\Phi}}_{\mathbf{A}_r}\mathbf{u}_r + \underbrace{\mathbf{\Phi}^T\mathbf{f}(\mathbf{\Phi}\mathbf{u}_r; \boldsymbol{\mu})}_{\mathbf{f}_r} \tag{2.10}$$

where $\mathbf{A}_r = \mathbf{\Phi}^T\mathbf{A}\mathbf{\Phi} \in \mathbb{R}^{K\times K}$ and $\mathbf{f}_r = \mathbf{\Phi}^T\mathbf{f}(\mathbf{\Phi}\mathbf{u}_r; \boldsymbol{\mu}) \in \mathbb{R}^{K\times 1}$. The initial condition (2.2) is also projected onto the reduced basis:

$$\mathbf{u}_r(t=0) = \mathbf{\Phi}^T\mathbf{u}^0 \tag{2.11}$$

Similarly, the reduced Jacobian is:

$$\mathbf{J}_r(\mathbf{u}, t; \boldsymbol{\mu}) = \mathbf{A}_r + \mathbf{\Phi}^T\mathbf{J}^{\mathbf{f}}(\mathbf{u}, t; \boldsymbol{\mu})\mathbf{\Phi} \tag{2.12}$$

Since $K \ll N$, we have thus projected the large-scale governing equation (2.1) onto a low-dimensional subspace, resulting in a system of ODEs with significantly smaller number of unknowns. Certainly, the quality of such ROM is strongly dependent upon the set of basis vectors $\{\boldsymbol{\phi}_i\}_{i=1}^{K}$ used for projection. As discussed in Section 1.2.1, there are a number of methods that can be used to construct these basis vectors. In this work, we use the proper orthogonal decomposition (POD) method. POD, also knowns as the Karhunen-Lòeve expansion, derives the basis vectors from an emsemble of state solutions (or 'snapshots') obtained by solving the FOM at selected points in its parametric input space. For model reduction of dynamical problems, the unsteady simulations are either run for a prescribed number of time steps or until a final state of interest is fully developed (steady state or stable LCO, for example). Therefore at each parameter value, unsteady solution snapshots may be saved either at every time step or intermittently at certain time intervals. All of these snapshots are then compiled into a snapshot matrix. We denote $\mathbb{U} \in \mathbb{R}^{N\times n_s}$ as the snapshot matrix which contain as column vectors all n_s solution snapshots: $\mathbb{U} = \{\boldsymbol{u}_i\}_{i=1}^{n_s}$. POD formulates the generation of basis vectors as a minimization problem. In particular, the K basis

vectors $\boldsymbol{\Phi} = \{\boldsymbol{\phi}_i\}_{i=1}^K$ are derived such that the sum of the least-squares approximation errors of the n_s snapshots is minimized:

$$\boldsymbol{\Phi} = \arg\min_{\{\boldsymbol{\varphi}_i\}_i^K} \sum_{j=1}^{n_s} \|\boldsymbol{u}_j - \sum_{j=1}^{K} (\boldsymbol{u}_j^T \boldsymbol{\varphi}_i)\boldsymbol{\varphi}_i\|_2^2, \tag{2.13}$$

$$\text{subject to } \boldsymbol{\varphi}_i^T \boldsymbol{\varphi}_j = \delta_{ij}, \text{ for } 1 \leq i, j \leq K, \tag{2.14}$$

where δ_{ij} is the Kronecker delta. Here we assume that the state dimension of the problem is larger than the total number of snapshots: $N > n_s$. It can be shown that the solution to the minimization problem (2.14) is given by the left singular vectors of the snapshot matrix $\mathbb{U}$. We express the singular value decomposition (SVD) of $\mathbb{U}$ as follows:

$$\mathbb{U} = \boldsymbol{V}\boldsymbol{\Sigma}\boldsymbol{W}^T \tag{2.15}$$

where $\boldsymbol{V} = [\boldsymbol{v}_1, \ldots, \boldsymbol{v}_{n_s}]$ and $\boldsymbol{\Sigma} = diag(\sigma_1, \ldots, \sigma_{n_s})$, $\sigma_1 \geq \sigma_2 \geq \ldots \geq \sigma_K \geq \ldots \geq \sigma_{n_s} \geq 0$. The POD modes are the first K dominant left singular vectors of the snapshot matrix: $\boldsymbol{\Phi} = \{\boldsymbol{\phi}_i\}_{i=1}^K = \{\boldsymbol{v}_i\}_{i=1}^K$. The sum of the least-squares errors in approximating the n_s snapshots using these K POD modes is given by

$$\varepsilon_{POD} = \sum_{j=1}^{n_s} \|\boldsymbol{u}_j - \sum_{j=1}^{K} (\boldsymbol{u}_j^T \boldsymbol{\phi}_i)\boldsymbol{\phi}_i\|_2^2 = \sum_{i=k+1}^{n_s} \sigma_i^2 \tag{2.16}$$

This error can be thought of as the 'omitted energy' of the snapshots due to the truncation of POD basis $\boldsymbol{\Phi} = \{\boldsymbol{\phi}_i\}_{i=1}^K$ from $\boldsymbol{V} = \{\boldsymbol{v}_i\}_{i=1}^{n_s}$, with $\sum_{i=1}^{n_s} \sigma_i^2$ being the 'total energy' of the snapshots. This provides guidance in the determination of K: the number of POD basis vectors to retain from the set of left singular vectors. In particular, K is chosen as the smallest integer such that the 'relative omitted energy' Ω is less than a certain threshold:

$$\Omega = 1 - \frac{\sum_{i=1}^{K} \sigma_i^2}{\sum_{i=1}^{n_s} \sigma_i^2} < \epsilon \tag{2.17}$$

Note that this criterion does not provide any indication on the accuracy of the resultant POD-Galerkin ROM when it is solved at an input parameter value that has

not been sampled — solutions at a new point in the parameter space may not be in the span of the original snapshot matrix $\mathbb{U}$. As discussed in Section 1.2.1, advanced sampling techniques such as [18] can be used to construct $\mathbb{U}$ such that the resultant POD basis accurately approximates the entire solution space. For the work presented here, we use the simple uniform sampling method. However, the methodology presented here can be combined with more advanced sampling techniques to obtain more accurate ROMs.

Although the ROM thus constructed results in a system of equations of reduced dimension K, the computational cost of integrating the POD-Galerkin ROM (2.10) forward in time is still a function of the FOM dimension N. This inefficiency can be understood by examining the reduced nonlinear term $\mathbf{f}_r$ and reduced Jacobian $\mathbf{J}_r$:

$$\mathbf{f}_r(\mathbf{u}, t; \boldsymbol{\mu}) = \underbrace{\boldsymbol{\Phi}^T}_{K\times N} \underbrace{\mathbf{f}(\boldsymbol{\Phi}\mathbf{u}_r, t; \boldsymbol{\mu})}_{N\times 1} \tag{2.18}$$

$$\mathbf{J}_r(\mathbf{u}, t; \boldsymbol{\mu}) = \mathbf{A}_r + \underbrace{\boldsymbol{\Phi}^T}_{K\times N} \underbrace{\mathbf{J}^{\mathbf{f}}(\mathbf{u}, t; \boldsymbol{\mu})}_{N\times N} \underbrace{\boldsymbol{\Phi}}_{N\times K} \tag{2.19}$$

For the reduced nonlinear term, the inefficiency arises from three sources. First, the full-order state solution must be reconstructed from the $N \times K$ basis vectors via the expansion $\boldsymbol{\Phi}\mathbf{u}_r$. Then the full-order nonlinear term is evaluated from the reconstructed state at all of its N components. Finally, another matrix-vector multiplication involving the $K \times N$ matrix $\boldsymbol{\Phi}^T$ is required to project the nonlinear term onto the reduced basis. Similar inefficiency can be observed in the evaluation of the reduced Jacobian in which the full $N \times N$ Jacobian of the nonlinear term $\mathbf{J}^{\mathbf{f}}$ must be constructed before being projected onto to the reduced basis. Therefore, even though $\mathbf{f}_r$ and $\mathbf{J}_r$ themselves are of low dimensions, the computational costs involved in forming them are still dependent on the FOM dimension N. Such inefficiency is particularly problematic for nonlinear dynamical problems solved using implicit time-marching methods which require the evaluation of the nonlinear Jacobian multiple times at each time step.

A method capable of computing $\mathbf{f}_r$ and $\mathbf{J}_r$ at a computational cost that is inde-

pendent of N is therefore required to fully realize the efficiency of the POD-based ROM.

2.1.2 Discrete Empirical Interpolation Method (DEIM)

To avoid full evaluations of the nonlinear term and Jacobian matrix, the Empirical Interpolation Method (EIM) was proposed in [8] to approximate these terms via interpolation over a subset of points that are independent of the large-scale FOM dimension N. In this work, we use the Discrete Empirical Interpolation Method (DEIM), the discrete variant of the EIM, introduced by Chaturantabut and Sorensen in [24].

The first step of the DEIM is to approximate the nonlinear term $\mathbf{f}(\mathbf{\Phi}\mathbf{u}_r, t; \boldsymbol{\mu})$ using a separate set of basis vectors $\mathbf{\Psi}$ that are different from those used for the state:

$$\mathbf{f}(\mathbf{u}, t; \boldsymbol{\mu}) \approx \mathbf{\Psi}\mathbf{c}(t; \boldsymbol{\mu}) \tag{2.20}$$

where $\mathbf{\Psi} = [\boldsymbol{\psi}_1, \boldsymbol{\psi}_2, \ldots, \boldsymbol{\psi}_M] \in \mathbb{R}^{N \times M}, M \ll N$ are the basis vectors for the nonlinear term and $\mathbf{c} \in \mathbb{R}^{M \times 1}$ the vector of expansion coefficients. The basis vectors $\mathbf{\Psi} = \{\boldsymbol{\psi}_i\}_{i=1}^{M}$ are derived from the snapshots of the nonlinear term $\mathbb{F} = \{\mathbf{f}_i\}_{i=1}^{n_s}$, using the same POD method as described for constructing the state basis vectors $\mathbf{\Phi} = \{\boldsymbol{\phi}_i\}_{i=1}^{K}$. The collection of these nonlinear snapshots do not incur additional computational cost in sampling because the nonlinear terms are already evaluated during the sampling of state snapshots $\mathbb{U}$. Note that (2.20) represents an overdetermined system. To compute $\mathbf{c}$ at a computational cost independent of N, we select M interpolation points of $\mathbf{f}$ and enforce equality for the corresponding system of equations in (2.20). This results in an $M \times M$ system from which the coefficient vector $\mathbf{c}$ can be uniquely determined:

$$\mathbf{f}_{\vec{\mathbf{z}}}(\mathbf{u}_{\vec{\mathbf{z}}'}, t; \boldsymbol{\mu}) = \mathbf{\Psi}_{\vec{\mathbf{z}}}\mathbf{c}(t; \boldsymbol{\mu}) \tag{2.21}$$

where $\vec{\mathbf{z}} = [z_1, \ldots, z_M]^T \in \mathbb{R}^{M \times 1}$ is a vector containing M interpolation indicies, $\mathbf{f}_{\vec{\mathbf{z}}} \in \mathbb{R}^{M \times 1}$ is the nonlinear term evaluated at these M interpolation points, and

$\mathbf{\Psi}_{\vec{\mathbf{z}}} \in \mathbb{R}^{M \times M}$ is the corresponding M rows of $\mathbf{\Psi}$.

For nonlinear problems that do not have componentwise dependence on the state, there may be multiple state components that must be reconstructed for the evaluation of a single component of the nonlinear term. For example, in structures problems, the nonlinear force at a given interpolation index $\mathbf{f}_{z_i}$ is determined by multiple generalized displacements (i.e. the state) at all the neighbouring elements. Therefore, for a general nonlinear term with noncomponentwise state dependence, the set of the indices of the state components that must be evaluated in order to compute the M interpolation points $\mathbf{f}_{\vec{\mathbf{z}}}$ is different (and typically larger in size) than $\vec{\mathbf{z}}$. We denote $\vec{\mathbf{z}}'$ as such a set of $M' \geq M$ indices of the state components, and $\mathbf{u}_{\vec{\mathbf{z}}'}$ as the state evaluated at these M' points. $\vec{\mathbf{z}}'$ can typically be derived from $\vec{\mathbf{z}}$ based on the nodal connectivity of the discretized structure. The support of state on the nonlinear term is often local; that is, $M \leq M' \ll N$. Therefore, the DEIM approximation presented next is still efficient.

Solving $\mathbf{c}$ from (2.21) and substituting it into the expansion (2.20), we obtain the DEIM approximation of the nonlinear term:

$$\mathbf{f}(\mathbf{u}, t; \boldsymbol{\mu}) \approx \mathbf{\Psi} \mathbf{\Psi}_{\vec{\mathbf{z}}}^{-1} \mathbf{f}_{\vec{\mathbf{z}}}(\mathbf{u}_{\vec{\mathbf{z}}'}, t; \boldsymbol{\mu}) \tag{2.22}$$

Projecting this approximation onto the reduced basis via (2.18) to obtain the DEIM approximation of the reduced nonlinear term:

$$\mathbf{f}_r(\mathbf{u}_r, t; \boldsymbol{\mu}) = \underbrace{\mathbf{\Phi}^T \mathbf{\Psi} \mathbf{\Psi}_{\vec{\mathbf{z}}}^{-1}}_{K \times M} \underbrace{\mathbf{f}_{\vec{\mathbf{z}}}(\mathbf{\Phi}_{\vec{\mathbf{z}}'} \mathbf{u}_r, t; \boldsymbol{\mu})}_{M \times 1} \tag{2.23}$$

where $\mathbf{u}_{\vec{\mathbf{z}}'} = \mathbf{\Phi}_{\vec{\mathbf{z}}'} \mathbf{u}_r$ is the state evaluated at M' points specified by $\vec{\mathbf{z}}'$ and $\mathbf{\Phi}_{\vec{\mathbf{z}}'} \in \mathbb{R}^{M' \times K}$ contains the corresponding M' rows of $\mathbf{\Phi}$. The DEIM approximation of the reduced Jacobian can be derived from (2.23):

$$\mathbf{J}_r(\mathbf{u}_r, t; \boldsymbol{\mu}) = \underbrace{\mathbf{A}_r}_{K \times K} + \underbrace{\mathbf{\Phi}^T \mathbf{\Psi} \mathbf{\Psi}_{\vec{\mathbf{z}}}^{-1}}_{K \times M} \underbrace{\mathbf{J}^{\mathbf{f}}_{\vec{\mathbf{z}}, \vec{\mathbf{z}}'}(\mathbf{\Phi}_{\vec{\mathbf{z}}'} \mathbf{u}_r, t; \boldsymbol{\mu})}_{M \times M'} \underbrace{\mathbf{\Phi}_{\vec{\mathbf{z}}'}}_{M' \times K} \tag{2.24}$$

where $\mathbf{J^f}_{\vec{\mathbf{z}},\vec{\mathbf{z}}'}$ denotes the Jacobian of the nonlinear term $\mathbf{J^f} \equiv \frac{\partial \mathbf{f}}{\partial \mathbf{u}}$ evaluated at M rows prescribed by $\vec{\mathbf{z}}$ and M' columns prescribed by $\vec{\mathbf{z}}'$. Note that the dimensions of all the matrices in (2.23) and (2.24) are independent of N. DEIM therefore allows evaluation of the reduced nonlinear term and reduced Jacobian at computational costs that are only functions of K, M and M'. We defer the presentation of an efficient offline-online procedure using such POD-DEIM methodology to the next subsection.

For the remainder of this section, we present and briefly discuss the algorithm with which the set of interpolation indices $\vec{\mathbf{z}}$ is selected. The original point selection algorithm was proposed in [8] for the reduced-basis-EIM framework. For this work, we adopt the discrete variant of this algorithm, proposed by Chaturantabut and Sorensen in [24] for semi-discrete systems. To keep our discussion self-contained, we briefly summarize this point selection procedure in Algorithm 1. For detailed discussions including DEIM error bounds, please refer to [24]. In this algorithm, a 'greedy' selection process is employed to iteratively build the set of interpolation indices in such a way that the i-th interpolation point is placed at the spatial location where the approximation error ($|\mathbf{r}|$) of the i-th basis vector $\boldsymbol{\psi}_i$ using the first $i-1$ interpolation points $\{z_j\}_{j=1}^{i-1}, \forall\, 2 \leq i \leq M$ and basis vectors $\{\boldsymbol{\psi}_j\}_{j=1}^{i-1}, \forall\, 2 \leq i \leq M$ is the greatest.

Algorithm 1: DEIM interpolation point selection algorithm

INPUT: $\{\boldsymbol{\psi}_i\}_{i=1}^{M} \in \mathbb{R}^{N\times M}$

$[|\rho|, z_1] = max\{|\boldsymbol{\psi}_1|\}$

$\boldsymbol{\Psi} = [\boldsymbol{\psi}_1], \vec{\mathbf{z}} = [z_1]$

for *i = 2 to M* **do**

  Solve $\boldsymbol{\Psi}_{\vec{\mathbf{z}}}\mathbf{c} = (\boldsymbol{\psi}_i)_{\vec{\mathbf{z}}}$ for $\mathbf{c}$

  $\mathbf{r} = \boldsymbol{\psi}_i - \boldsymbol{\Psi}\mathbf{c}$

  $[|\rho|, z_i] = max\{|\mathbf{r}|\}$

  $\boldsymbol{\Psi} \leftarrow [\boldsymbol{\Psi}, \boldsymbol{\psi}_i], \vec{\mathbf{z}} \leftarrow [\vec{\mathbf{z}}, z_i]$

end

OUTPUT: $\vec{\mathbf{z}} = [z_1, \ldots, z_M]^T \in \mathbb{R}^{M\times 1}$

2.1.3 Offline-Online Algorithm

The ROM of the large-scale nonlinear dynamical system (2.1) constructed via the POD-DEIM metholodgy can be expressed as:

$$\frac{d\mathbf{u}_r}{dt} = \underbrace{\mathbf{A}_r}_{K\times K}\mathbf{u}_r + \underbrace{\mathbf{B}_r}_{K\times M}\underbrace{\mathbf{f}_{\vec{\mathbf{z}}}(\underbrace{\boldsymbol{\Phi}_{\vec{\mathbf{z}}'}\mathbf{u}_r}_{M'\times 1}, t; \boldsymbol{\mu})}_{M\times 1} \tag{2.25}$$

with initial condition:

$$\mathbf{u}_r(t=0) = \boldsymbol{\Phi}^T\mathbf{u}^0 \tag{2.26}$$

and the corresponding reduced Jacobian:

$$\mathbf{J}_r(\mathbf{u}_r, t; \boldsymbol{\mu}) = \underbrace{\mathbf{A}_r}_{K\times K} + \underbrace{\mathbf{B}_r}_{K\times M}\underbrace{\mathbf{J}^{\mathbf{f}}{}_{\vec{\mathbf{z}},\vec{\mathbf{z}}'}(\underbrace{\boldsymbol{\Phi}_{\vec{\mathbf{z}}'}\mathbf{u}_r}_{M'\times 1}, t; \boldsymbol{\mu})}_{M\times M'}\underbrace{\boldsymbol{\Phi}_{\vec{\mathbf{z}}'}}_{M'\times K} \tag{2.27}$$

where $\mathbf{A}_r = \boldsymbol{\Phi}^T\mathbf{A}\boldsymbol{\Phi} \in \mathbb{R}^{K\times K}$ and $\mathbf{B}_r = \boldsymbol{\Phi}^T\boldsymbol{\Psi}\boldsymbol{\Psi}_{\vec{\mathbf{z}}}^{-1} \in \mathbb{R}^{K\times M}$ are parameter-independent matricies: they are constant in time and do not depend on the input parameters $\boldsymbol{\mu}$.

Therefore they only need to be computed once as soon as the basis vectors of the state and nonlinear term have been computed via POD. The collection of snapshots of the state ($\mathbb{U}$) and of the nonlinear term ($\mathbb{F}$), the generation of the corresponding basis vectors $\mathbf{\Phi}$ and $\mathbf{\Psi}$, the selection of the interpolation indices $\vec{\mathbf{z}}$, as well as the precomputations of $\mathbf{A}_r$ and $\mathbf{B}_r$ matrices can all be performed in an 'offline' phase.

The ROM constructed with such 'one-off' offline process enables efficient multi-query 'online' computations for which the complexities are independent of the FOM dimension N. Given a specific set of input parameters $\boldsymbol{\mu}^*$ and projected initial condition $\mathbf{u}_r(t=0)$, the reduced system (2.25) can be integrated forward in time. Here we assume that an implicit time-marching scheme is used, which results in a system of nonlinear equations to be solved at each time step, requiring multiple evaluations and inversions of the reduced Jacobian. In the online phase, to compute the reduced nonlinear term $\mathbf{f}_r(\mathbf{u}_r, t; \boldsymbol{\mu}) = \mathbf{B}_r \mathbf{f}_{\vec{\mathbf{z}}}(\mathbf{\Phi}_{\vec{\mathbf{z}}'} \mathbf{u}_r, t; \boldsymbol{\mu})$, one must first carry out the partial reconstruction of the state vector $\mathbf{u}_{\vec{\mathbf{z}}'} = \mathbf{\Phi}_{\vec{\mathbf{z}}'} \mathbf{u}_r$ at a cost of $O(M'K)$ floating point operations (flops) before using it to evaluate the M components of $\mathbf{f}_{\vec{\mathbf{z}}}$, which is then multiplied with the $\mathbf{B}_r$ matrix at a cost of $O(KM)$ flops. Likewise, the online computation of the reduced Jacobian of the nonlinear term $\mathbf{J}^{\mathbf{f}}{}_r(\mathbf{u}_r, t; \boldsymbol{\mu}) = \mathbf{B}_r \mathbf{J}^{\mathbf{f}}{}_{\vec{\mathbf{z}},\vec{\mathbf{z}}'}(\mathbf{\Phi}_{\vec{\mathbf{z}}'} \mathbf{u}_r, t; \boldsymbol{\mu}) \mathbf{\Phi}_{\vec{\mathbf{z}}'}$ consists of three steps: partial evaluation of the Jacobian $\mathbf{J}^{\mathbf{f}}$ at only M rows and M' columns as required by $\vec{\mathbf{z}}$ and $\vec{\mathbf{z}}'$ in order to form $\mathbf{J}^{\mathbf{f}}{}_{\vec{\mathbf{z}},\vec{\mathbf{z}}'}$, multiplication between $\mathbf{J}^{\mathbf{f}}{}_{\vec{\mathbf{z}},\vec{\mathbf{z}}'}$ and $\mathbf{\Phi}_{\vec{\mathbf{z}}'}$ at a cost of $O(MM'K)$ flops, before right-multiplying the result with $\mathbf{B}_r$ at a cost of $O(MK^2)$ flops. The inversion of the $K \times K$ reduced Jacobian $\mathbf{J}_r$ can be performed at a cost of $O(K^3)$ flops. Therefore, the computational cost of the repeated online evaluation of the ROM (2.25) constructed with the POD-DEIM methodology is only a function of $K, M, M' \ll N$.

The convergence of such online computation can be monitored by evaluating the $K \times 1$ residual vector. For problems that experience LCO, time history of the state $\mathbf{u}_{z^*}$ at a particular spatial location z^* can also be computed on-the-fly via an inexpensive partial reconstruction $\mathbf{u}_{z^*} = \mathbf{\Phi}_{z^*} \mathbf{u}_r$, which is simply a dot product with $O(K)$ flops. The computation is terminated if the time history shows satisfactory convergence of the limit cycle amplitude.

The offline-online procedure described above are summarized in Algorithm 2 and 3 below:

Algorithm 2: Offline Stage: Sampling, construction of basis vectors and pre-computation of parameter-independent matrices

---

Offline Stage

1. Sample the input parameter space to form the snapshot matrices $\mathbb{U} = \{\mathbf{u}_i\}_{i=1}^{n_s}$ and $\mathbb{F} = \{\mathbf{f}_i\}_{i=1}^{n_s}$ for the state and nonlinear term, respectively.

2. Using the POD method as presented in Section 2.1.1, compute the state basis vectors $\boldsymbol{\Phi} = \{\boldsymbol{\phi}_i\}_{i=1}^{K}$ from $\mathbb{U}$ and the nonlinear basis vectors $\boldsymbol{\Psi} = \{\boldsymbol{\psi}_i\}_{i=1}^{M}$ from $\mathbb{F}$.

   K and M are determined based on a prescribed 'relative omitted energy' tolerance, as shown on (2.17).

3. Compute the M interpolation indices $\vec{\mathbf{z}} = [z_1, \ldots, z_M]^T$ using the point selection procedure described in Algorithm 1; Infer the corresponding indices for the state $\vec{\mathbf{z}}'$ from $\vec{\mathbf{z}}$ based on nodal connectivity of the problem.

4. Form $\boldsymbol{\Psi}_{\vec{\mathbf{z}}}$ by extracting M rows of $\boldsymbol{\Psi}$ as specified by $\vec{\mathbf{z}}$;
   Form $\boldsymbol{\Phi}_{\vec{\mathbf{z}}'}$ by extracting M' rows of $\boldsymbol{\Phi}$ as specified by $\vec{\mathbf{z}}'$.

5. Precompute parameter independent matrices $\mathbf{A}_r = \boldsymbol{\Phi}^T \mathbf{A} \boldsymbol{\Phi}$ and $\mathbf{B}_r = \boldsymbol{\Phi}^T \boldsymbol{\Psi} \boldsymbol{\Psi}_{\vec{\mathbf{z}}}^{-1}$.

Algorithm 3: Online Stage: evaluating ROM at a particular set of input parameters $\boldsymbol{\mu}^*$

Online Stage

1. Determine the particular set of input parameters $\boldsymbol{\mu}^*$ for which the ROM is to be evaluated and obtain the reduced initial condition via projection $\mathbf{u}_r(t=0) = \boldsymbol{\Phi}^T \mathbf{u}^0$.

2. Evaluate $\mathbf{f}_r(\mathbf{u}_r, t; \boldsymbol{\mu}^*) = \mathbf{B}_r \mathbf{f}_{\vec{\mathbf{z}}}(\boldsymbol{\Phi}_{\vec{\mathbf{z}}'} \mathbf{u}_r, t; \boldsymbol{\mu}^*)$ and $\mathbf{J}_r(\mathbf{u}_r, t; \boldsymbol{\mu}^*) = \mathbf{A}_r + \mathbf{B}_r \mathbf{J}^{\mathbf{f}}{}_{\vec{\mathbf{z}},\vec{\mathbf{z}}'}(\boldsymbol{\Phi}_{\vec{\mathbf{z}}'} \mathbf{u}_r, t; \boldsymbol{\mu}^*) \boldsymbol{\Phi}_{\vec{\mathbf{z}}'}$ given $\mathbf{u}_r$ and $\boldsymbol{\mu}^*$.

3. Solve ROM (2.25) forward in time using $\mathbf{f}_r$ and $\mathbf{J}_r$.

4. Compute residual and reconstruct state at selected location(s) of interest to monitor convergence.

5. Repeat Step 2-4 until either steady state or LCO has been reached.

2.2 A Modified POD-DEIM Methodology

The last section presents the POD-DEIM model reduction methodology as proposed in [24] with generalizations for vector valued PDEs and nonlinear terms with non-componentwise dependence on state.

For a vector-valued PDE with N_v unknown variables, the $N \times 1$ state vector typically consists of a concatenation of N_v vectors each containing the N_x nodal values, such that $N = N_v N_x$. In other words, all the unknown quantities at all spatial grid points are 'lumped' together forming a 'globalized' solution vector. Therefore for vector-valued PDEs, oftentimes a single globalized set of $N \times K$ POD modes is used to represent all the unknown variables, as presented in the previous section. This is referred to as the 'vector-valued POD modes' by researchers in [69] and [47]. An

alternative is to separate the globalized snapshot matrix into N_v smaller snapshot matrices, one for each unknown variable. An individual set of 'variable-separated POD basis' is then constructed for each of the N_v variables from their corresponding snapshot matrices. These are referred to as the 'scalar-valued POD basis' in [69] and [47].

The relative merits of the two approaches depend on the specific problems to which they are applied. Some have shown that scalar-valued POD modes allow more accurate approximations for each unknown variable [47, 23], while others have used globalized or vector-valued modes with remarkable success [37, 17]. For problems in which the variables are governed by dynamics with disparate time scales, scale-valued POD modes should be used. Another key factor that determines whether the scalar-valued basis should be used in place of vector-valued basis is whether the variables have drastically different orders of magnitude. As demonstrated in Chapter 3, this can significantly reduce the accuracy of the ROM constructed using vector-valued POD modes.

Next we extend the POD-DEIM methodology to include scalar-valued POD modes. Note that depending on the problem, one may use scalar-valued POD modes for either or both of state and nonlinear term.

2.2.1 Scalar-valued POD modes

Separate the snapshot matrices for the state ($\mathbb{U}$) and the nonlinear term ($\mathbb{F}$) each into N_v smaller scalar-valued matrices grouped by unknown variables.

$$\mathbb{U} = [\mathbb{U}^1, \mathbb{U}^2, \ldots, \mathbb{U}^{N_v}], \quad \mathbb{U}^i \in \mathbb{R}^{N_x \times n_s} \tag{2.28}$$

$$\mathbb{F} = [\mathbb{F}^1, \mathbb{F}^2, \ldots, \mathbb{F}^{N_v}], \quad \mathbb{F}^i \in \mathbb{R}^{N_x \times n_s} \tag{2.29}$$

where $\mathbb{U}^i$ and $\mathbb{F}^i$ contain n_s snapshots of the i-th state variable and i-th variable of the nonlinear term respectively, each evaluated at N_x grid points in space. Using the

POD method, generate a set of basis vectors for each scalar-valued snapshot matrix:

$$\tilde{\mathbf{\Phi}} = diag\{\mathbf{\Phi}^1, \mathbf{\Phi}^2, \ldots, \mathbf{\Phi}^{N_v}\}, \quad \mathbf{\Phi}^i \in \mathbb{R}^{N_x \times K_i} \tag{2.30}$$

$$\tilde{\mathbf{\Psi}} = diag\{\mathbf{\Psi}^1, \mathbf{\Psi}^2, \ldots, \mathbf{\Psi}^{N_v}\}, \quad \mathbf{\Psi}^i \in \mathbb{R}^{N_x \times M_i} \tag{2.31}$$

where $\mathbf{\Phi}^i$ contains as columns the K_i scalar-valued POD basis vectors for the i-th state variable generated from $\mathbb{U}^i$ and $\mathbf{\Psi}^i$ contains as columns the M_i scalar-valued POD basis vectors for the i-th variable of the nonlinear term generated from $\mathbb{F}^i$. Furthermore, $\tilde{\mathbf{\Phi}} \in \mathbb{R}^{N \times \tilde{K}}$ with $\tilde{K} = \sum_{i=1}^{N_v} K_i$ and $\tilde{\mathbf{\Psi}} \in \mathbb{R}^{N \times \tilde{M}}$ with $\tilde{M} = \sum_{i=1}^{N_v} M_i$. Note that the numbers of state POD modes for each variable do not have to be the same. Instead, they are determined by the 'relative omitted energy' criterion for each variable as described in Section 2.1.1. The same applies to the POD modes for the nonlinear term. Each unknown variable in the state and nonlinear term can then be approximated individually using these scalar-valued POD modes as follows:

$$\mathbf{u}^i \approx \mathbf{\Phi}^i \mathbf{u}_r^i, \quad i = 1, \ldots, N_v \tag{2.32}$$

$$\mathbf{f}^i \approx \mathbf{\Psi}^i \mathbf{c}^i, \quad i = 1, \ldots, N_v \tag{2.33}$$

where $\mathbf{u}^i \in \mathbb{R}^{N_x \times 1}$ is the discretized state evaluated at N_x grid points corresponding to the i-th state variable in the PDE. $\mathbf{f}^i \in \mathbb{R}^{N_x \times 1}$ is the discretized nonlinear term evaluated at N_x grid points corresponding to the i-th nonlinear term in the PDE. $\mathbf{u}_r^i$ and $\mathbf{c}^i$ are the expansion coefficients of corresponding discretized state and nonlinear terms. Note that here both the state and nonlinear term can be re-assembled in the 'vector-valued' form such that:

$$\mathbf{u} \approx \tilde{\mathbf{\Phi}} \mathbf{u}_r \tag{2.34}$$

$$\mathbf{f} \approx \tilde{\mathbf{\Psi}} \mathbf{c} \tag{2.35}$$

where

$$\mathbf{u} = \begin{bmatrix} \mathbf{u}^1 \\ \vdots \\ \mathbf{u}^{N_v} \end{bmatrix} \in \mathbb{R}^{N\times 1}, \quad \mathbf{u}_r = \begin{bmatrix} \mathbf{u}_r^1 \\ \vdots \\ \mathbf{u}_r^{N_v} \end{bmatrix} \in \mathbb{R}^{\tilde{K}\times 1} \tag{2.36}$$

and

$$\mathbf{f} = \begin{bmatrix} \mathbf{f}^1 \\ \vdots \\ \mathbf{f}^{N_v} \end{bmatrix} \in \mathbb{R}^{N\times 1}, \quad \mathbf{c} = \begin{bmatrix} \mathbf{c}^1 \\ \vdots \\ \mathbf{c}^{N_v} \end{bmatrix} \in \mathbb{R}^{\tilde{M}\times 1} \tag{2.37}$$

To determine the expansion coefficients $\mathbf{c}^i$ for each nonlinear variable, DEIM interpolation point selection algorithm from Section 2.1.2 is applied to each scalar POD basis for the nonlinear term $\mathbf{\Psi}^i, i = 1, \ldots, N_v$, generating N_v sets of interpolation indices $\{\vec{\mathbf{z}}_i\}_{i=1}^{N_v} \in \mathbb{R}^{M_i\times 1}$. Note that the $\vec{\mathbf{z}}_i$ indices are 'local' indices within $\mathbf{f}^i$, ranging from 1 to N_x (instead of from 1 to $N = N_x N_v$ in the case of global POD modes). In order to compute the M_i components of $\mathbf{f}^i$, one must determine based on the nodal connectivity of the problem, the indices of the state components that must be reconstructed. It is important to note in this case that *all* N_v state variables situated around these M_i points may be required for such computations — not only the i-th one. We determine all necessary indices of all the state variables, translate them into 'global' index and concatenate them together: $\vec{\mathbf{z}}_i \mapsto (\vec{\mathbf{z}}_i')_g$, where the subscript g denotes 'global'. This translation allows us to express the reconstruction of state components across all N_v variables necessary to compute $\mathbf{f}^i_{\vec{\mathbf{z}}_i}$ succinctly as $\tilde{\mathbf{\Phi}}_{(\vec{\mathbf{z}}_i')_g}\mathbf{u}_r$. The DEIM approximation of $\mathbf{f}^i$ can then be expressed as follows:

$$\mathbf{f}^i \;\approx\; \mathbf{\Psi}^i(\mathbf{\Psi}^i_{\vec{\mathbf{z}}_i})^{-1}\mathbf{f}^i_{\vec{\mathbf{z}}_i}(\tilde{\mathbf{\Phi}}_{(\vec{\mathbf{z}}_i')_g}\mathbf{u}_r) \tag{2.38}$$

where $\mathbf{f}^i_{\vec{\mathbf{z}}_i} \in \mathbb{R}^{M_i\times 1}$ contains M_i components of $\mathbf{f}^i$ specified by $\vec{\mathbf{z}}_i$ and $\mathbf{\Psi}^i_{\vec{\mathbf{z}}_i}$ contains the corresponding M_i rows of $\mathbf{\Psi}^i$.

Before applying (2.34), (2.35) and (2.38) to the POD-DEIM ROM (2.25), attention must be paid to the increase of computational cost due to this approach. Firstly, the total number of DEIM points is now $\tilde{M} = \sum_{i=1}^{N_v} M_i$, typically much greater than

the M points in the approach using 'vector-valued POD modes' discussed in Section 2.1.2. Secondly, the set of indices of all the state variables that must be reconstructed online to compute $\mathbf{f}^i_{\vec{\mathbf{z}}_i}, i = 1, \ldots, N_v$ is now $(\vec{\mathbf{z}}')_g = \bigcup_{i=1}^{N_v} (\vec{\mathbf{z}}'_i)_g$. Although certain points in $\{\vec{\mathbf{z}}_i\}_{i=1}^{N_v}$ may be spatially close enough to one another that they partially share the same support of the state, the set $(\vec{\mathbf{z}}')_g$ typically still may represent a substantial portion of the FOM dimension N. This is particularly true for problems in which the nonlinear term at a given grid point is a function of the state solution at many adjacent grid points, such as problems in nonlinear structures, as will be seen in Chapter 5. For such problems, the need to 'almost' fully reconstruct the state solution significantly compromises the efficiency of the POD-DEIM ROM.

Furthermore, within each variable, the nonlinear term may be highly oscillatory, making it difficult to approximate using an interpolatory method like DEIM. This results in the need to use large numbers of DEIM points in each variable of the nonlinear term ($\tilde{M} \sim N$), which again gives rise to the abovementioned increase in computational cost.

2.2.2 Over-sampling

In the DEIM procedure described thus far (including the scalar-valued approach in (2.38)), the expansion coefficients $\mathbf{c}^i$ of the nonlinear basis vectors are determined uniquely by having exactly M_i DEIM modes and M_i interpolation points. Instead of enforcing the approximation for $\mathbf{f}^i$ to be exact at the interpolation indicies $\vec{\mathbf{z}}_i$, one may evaluate each nonlinear variable $\mathbf{f}^i$ at more sample points, and in so doing obtain more sample points ($\hat{M}_i$) than the number of POD modes (M_i) within each nonlinear variable:

$$\mathbf{f}^i_{\hat{\mathbf{z}}_i} \in \mathbb{R}^{\hat{M}_i \times 1}, \quad \mathbf{\Psi}^i_{\hat{\mathbf{z}}_i} \in \mathbb{R}^{\hat{M}_i \times M_i}, \quad M_i < \hat{M}_i \ll N \tag{2.39}$$

where $\mathbf{f}^i_{\hat{\mathbf{z}}_i}$ is a vector of $\hat{M}_i$ components of the i-th nonlinear variable and $\mathbf{\Psi}^i_{\hat{\mathbf{z}}_i}$ contains $\hat{M}_i$ rows of the scalar-valued POD basis matrix $\mathbf{\Psi}^i$ with M_i basis vectors of the i-th nonlinear variable. This results in an overdetermined system for the expansion

coefficients $\mathbf{c}^i$:

$$\underset{\mathbf{c}^i}{\operatorname{argmin}} \|\boldsymbol{\Psi}^i_{\hat{\mathbf{z}}_i}\mathbf{c}^i - \mathbf{f}^i_{\hat{\mathbf{z}}_i}\|_2 \qquad \Rightarrow \qquad \mathbf{c}^i = (\boldsymbol{\Psi}^i_{\hat{\mathbf{z}}_i})^+\mathbf{f}^i_{\hat{\mathbf{z}}_i}, \quad i = 1, \ldots, N_v \tag{2.40}$$

$$\Rightarrow \qquad \mathbf{f}^i \approx \boldsymbol{\Psi}^i(\boldsymbol{\Psi}^i_{\hat{\mathbf{z}}_i})^+\mathbf{f}^i_{\hat{\mathbf{z}}_i} \tag{2.41}$$

Therefore, the pure interpolation of the original DEIM approximation has been replaced by a least-squares regression via over-sampling of the nonlinear term. Note that for a purely interpolatory method, although the approximation of $\mathbf{f}^i$ is exact at the interpolation points, the error can still be large *between* these points if the nonlinear term is highly oscillatory [81], and increasing the number of interpolation points does not necessarily reduce the approximation error [71]. In unsteady simulations where such error can accumulate over time, this is unacceptable. A regression with over-sampling on the other hand, minimizes the approximation error over all components of $\mathbf{f}^i$ in a least-squares sense [81]. It is also known to be less sensitive to perturbations in sample points. This can be particularly advantageous for the current methodology in which sample points in $\mathbf{f}^i$ are affected by the errors in the reconstruction of necessary state components.

However, attention must be paid to ensure such over-sampling is performed efficiently — blindly increasing the sample points in each nonlinear variable will cause the computational cost to grow quickly, compromising the efficiency of the ROM. Note that typically, to compute a single nonlinear variable at a given grid point $\mathbf{f}^i_{z^*_i}$, all other $N_v - 1$ nonlinear variables ($\mathbf{f}^j_{z^*_j}, j = 1, \ldots, N_v, j \neq i$) must also be computed (as is the case in nonlinear structures, for example). However, using the original DEIM approximation, the additional $N_v - 1$ values ($\mathbf{f}^j_{z^*_j}, j = 1, \ldots, N_v, j \neq i$) computed for the i-th nonlinear variable are not used in the approximation of other $N_v - 1$ nonlinear variables $\{\mathbf{f}^j\}_{j=1,j\neq i}^{N_v}$. The idea behind this modification is to utilize the extra information provided by the other $N_v - 1$ nonlinear variables that are previously not used. To that end, we perform 'node-based' selection rather than the previously discussed 'index-based' selection. In short, we select sample points of the nonlinear term by the entire information available at a given node. More specifically, if one nonlinear

variable is selected at a particular node, then all other $N_v - 1$ nonlinear variables residing on the same node are also selected as sample points. The sample indices of all N_v nonlinear variables are now the same and is the union of $\vec{\mathbf{z}}_i, i = 1, \ldots, N_v$:

$$\hat{\mathbf{z}} = \bigcup_{i=1}^{N_v} \vec{\mathbf{z}}_i \in \mathbb{R}^{\hat{M}\times 1} \tag{2.42}$$

By doing so, there are more sample points ($\hat{M}$) than the number of POD modes (M_i) within each nonlinear variable:

$$\mathbf{f}^i_{\hat{\mathbf{z}}} \in \mathbb{R}^{\hat{M}\times 1}, \quad \boldsymbol{\Psi}^i_{\hat{\mathbf{z}}} \in \mathbb{R}^{\hat{M}\times M_i}, \quad M_i < \hat{M} \ll N \tag{2.43}$$

where $\mathbf{f}^i_{\hat{\mathbf{z}}}$ is a vector of $\hat{M}$ components of the i-th nonlinear variable and $\boldsymbol{\Psi}^i_{\hat{\mathbf{z}}}$ contains $\hat{M}$ rows of the scalar-valued POD basis matrix $\boldsymbol{\Psi}^i$ with M_i basis vectors of the i-th nonlinear variable. This results in an overdetermined system for the expansion coefficients $\mathbf{c}^i$:

$$\underset{\mathbf{c}^i}{\operatorname{argmin}} \|\boldsymbol{\Psi}^i_{\hat{\mathbf{z}}}\mathbf{c}^i - \mathbf{f}^i_{\hat{\mathbf{z}}}\|_2 \qquad \Rightarrow \qquad \mathbf{c}^i = (\boldsymbol{\Psi}^i_{\hat{\mathbf{z}}})^+ \mathbf{f}^i_{\hat{\mathbf{z}}}, \quad i = 1, \ldots, N_v \tag{2.44}$$

$$\Rightarrow \qquad \mathbf{f}^i \approx \boldsymbol{\Psi}^i (\boldsymbol{\Psi}^i_{\hat{\mathbf{z}}})^+ \mathbf{f}^i_{\hat{\mathbf{z}}} \tag{2.45}$$

The modified POD-DEIM ROM with scalar-valued POD modes and over-sampling is:

$$\frac{d\mathbf{u}_r}{dt} = \underbrace{\hat{\mathbf{A}}_r}_{\tilde{K}\times\tilde{K}} \mathbf{u}_r + \underbrace{\hat{\mathbf{B}}_r}_{\tilde{K}\times N_v\hat{M}} \underbrace{\mathbf{f}_{\hat{\mathbf{z}}}(\underbrace{\tilde{\boldsymbol{\Phi}}_{(\hat{\mathbf{z}}')_g}\mathbf{u}_r}_{\hat{M}'\times 1}, t; \boldsymbol{\mu})}_{N_v\hat{M}\times 1} \tag{2.46}$$

where

$$\hat{\mathbf{A}}_r = \tilde{\boldsymbol{\Phi}}^T \mathbf{A} \tilde{\boldsymbol{\Phi}} \in \mathbb{R}^{\tilde{K}\times\tilde{K}}, \tag{2.47}$$

$$\hat{\mathbf{B}}_r = \tilde{\boldsymbol{\Phi}}^T diag\{\boldsymbol{\Psi}^1(\boldsymbol{\Psi}^1_{\hat{\mathbf{z}}})^+, \boldsymbol{\Psi}^2(\boldsymbol{\Psi}^2_{\hat{\mathbf{z}}})^+, \ldots, \boldsymbol{\Psi}^{N_v}(\boldsymbol{\Psi}^{N_v}_{\hat{\mathbf{z}}})^+\} \in \mathbb{R}^{\tilde{K}\times N_v\hat{M}} \tag{2.48}$$

$$\mathbf{f}_{\hat{\mathbf{z}}} = \begin{bmatrix} \mathbf{f}^1_{\hat{\mathbf{z}}} \\ \vdots \\ \mathbf{f}^{N_v}_{\hat{\mathbf{z}}} \end{bmatrix} \in \mathbb{R}^{N_v\hat{M}\times 1} \tag{2.49}$$

and $(\hat{\mathbf{z}}')_g$ contains the global indices of the all the state variables that must be reconstructed online as determined from $\hat{\mathbf{z}}$ based on nodal connectivity. The reduced Jacobian of the nonlinear term is:

$$\mathbf{J^f}_r = \underbrace{\hat{\mathbf{B}}_r}_{\tilde{K}\times N_v\hat{M}} \underbrace{\mathbf{J^f}_{\hat{\mathbf{z}},(\hat{\mathbf{z}}')_g}(\underbrace{\tilde{\boldsymbol{\Phi}}_{(\hat{\mathbf{z}}')_g}\mathbf{u}_r}_{\hat{M}'\times 1}, t; \boldsymbol{\mu})\, \tilde{\boldsymbol{\Phi}}_{(\hat{\mathbf{z}}')_g}}_{N_v\hat{M}\times\hat{M}'} \tag{2.50}$$

Note that both $\hat{\mathbf{A}}_r$ and $\hat{\mathbf{B}}_r$ can be constructed during an offline stage as described in Section 2.1.3. Including the complete nodal information does not incur any additional computational cost from the original DEIM approximation with the same number of interpolation points because all N_v components of the nonlinear term at a given node must be computed as long as one of them is required. Therefore, the $N_v\hat{M}$ components of $\mathbf{f}_{\hat{\mathbf{z}}}$ are computed at the same cost of computing just $\hat{M}$ components.

In (2.46), the compuational cost of the matrix-vector multiplication $\hat{\mathbf{B}}_r\mathbf{f}_{\hat{\mathbf{z}}}$ is a factor of N_v higher than the original POD-DEIM ROM in (2.25). A similar increase in computational cost can be seen in the online evaluation of $\mathbf{J^f}_r$ by (2.50). Such increase is typically moderate when the total number of variables N_v is small. For problems with large N_v, instead of employing one set of POD modes for each variable, one may group the variables with similar orders of magnitudes and use one scalar-valued POD basis for each of these groups. This however, requires some prior knowledges of the problem.

Chapter 3

Limit Cycle Oscillations in a Tubular Reactor

This chapter applies the original and modified POD-DEIM model reduction methodologies presented in Chapter 2 to a 1-D tubular reactor model which exhibits limit cycle oscillations (LCO). The problem set-up is described in Section 3.1.1 while the numerical method used to solve the governing equations forward in time to obtain time-asymptotic outputs such as LCO amplitudes and equilibrium positions is presented in Section 3.1.2. In Section 3.2, two reduced-order models of the system are derived using the original and modified POD-DEIM model reduction approaches. The performances of these two reduced-order models are assessed in Section 3.3 via two test cases. In the first one, the full-order system with equal magnitudes in both unknown variables is considered, whereas the second test case involves unknown variables with disparate magnitudes.

3.1 Full Order Model

In [43], Heinemann and Poore investigated the dynamics of a 1-D non-adiabatic tubular reactor with a single $A \rightarrow B$ reaction and axial mixing. In particular, they discovered multiple regions in the input parameter space that exhibit Hopf-bifurcation and limit cycle oscillations.

3.1.1 Governing Equations

The coupled system of time-dependent convection-diffusion-reaction (CDR) equations that governs the dynamics of the tubular reactor described above can be expressed in dimensionless form as follows:

$$\begin{aligned} \frac{\partial y}{\partial \tau} &= \frac{1}{Pe}\frac{\partial^2 y}{\partial s^2} - \frac{\partial y}{\partial s} - \mathcal{D} f(y,\theta), \\ \frac{\partial \theta}{\partial \tau} &= \frac{1}{Pe}\frac{\partial^2 \theta}{\partial s^2} - \frac{\partial \theta}{\partial s} - \beta(\theta - \theta_0) + \frac{B\mathcal{D}}{\mu} f(y,\theta) \end{aligned} \quad , \qquad s \in (0,1),\ \tau \geq 0 \qquad (3.1)$$

with Arrhenius type nonlinear reaction term: $f(y,\theta) = ye^{\gamma - \frac{\gamma}{\theta}}$. s and τ are the non-dimensional length and time respectively. y and θ represent the non-dimensional concentration and temperature respectively. Pe is the Péclet number. γ, B, β and θ_0 are known constants of the system. $\mathcal{D}$ is the Damköhler number which controls the dynamics of the system as will be seen. For this work, we have introduced an additional scaling parameter μ which controls the relative magnitudes between the concentration and temperature variables — when $\mu = 1$, the two state variables have equal magnitude of $O(1)$. Derivation of the system above from the dimensional form and its detailed analysis under parametric variations can be found in [43]. Robin boundary condition is imposed at the left boundary ($s = 0$) while the Neumann condition is given at the right boundary ($s = 1$):

$$\begin{aligned} \left.\frac{\partial y}{\partial s}\right|_{s=0} &= Pe(y|_{s=0} - \mu) \\ \left.\frac{\partial \theta}{\partial s}\right|_{s=0} &= Pe(\theta|_{s=0} - 1) \\ \left.\frac{\partial y}{\partial s}\right|_{s=1} &= 0 \\ \left.\frac{\partial \theta}{\partial s}\right|_{s=1} &= 0 \end{aligned} \quad , \qquad \tau \geq 0 \qquad (3.2)$$

The initial conditions are:

$$y(s, \tau = 0) = y_{in}, \quad \theta(s, \tau = 0) = \theta_{in}, \quad s \in [0,1] \qquad (3.3)$$

Note that in this problem, the Damköhler number $\mathcal{D}$ acts as an important control parameter for the system response. In particular, it is shown in [43] that when $Pe = 5$, $\gamma = 25$, $B = 0.5$, $\beta = 2.5$ and $\theta_0 = 1$, the system exhibits a Hopf-bifurcation with respect to $\mathcal{D}$ in the range $\mathcal{D} \in [0.16, 0.17]$; that is, there exists a critical Damköhler number $\mathcal{D}^* = 0.165$ such that for $\mathcal{D} < \mathcal{D}^*$ the unsteady solution eventually converges to a non-trivial steady state, as shown on Figure 3-1(a). For $\mathcal{D} > \mathcal{D}^*$, as shown on Figure 3-1(b), the system will tend towards a stable limit cycle, oscillating about a non-trivial equilibrium position, the amplitude of which is controlled by $\mathcal{D}$. In this work, we take the LCO amplitude to be the amplitude of the temperature oscillation at the reactor exit: $\theta(s = 1, t)$. Such system responses can be summarized by a bifurcation diagram as shown on Figure 3-2 where a Hopf-bifurcation about $\mathcal{D}^* = 0.165$ can be observed.

Note that to generate such a response curve, the governing equations (3.1), (3.2) and (3.3) must be solved forward in time so that time-asymptotic outputs such as LCO amplitudes and equilibrium solutions can be obtained. In the next subsection, we present the necessary numerical methods for solving this system of equations.

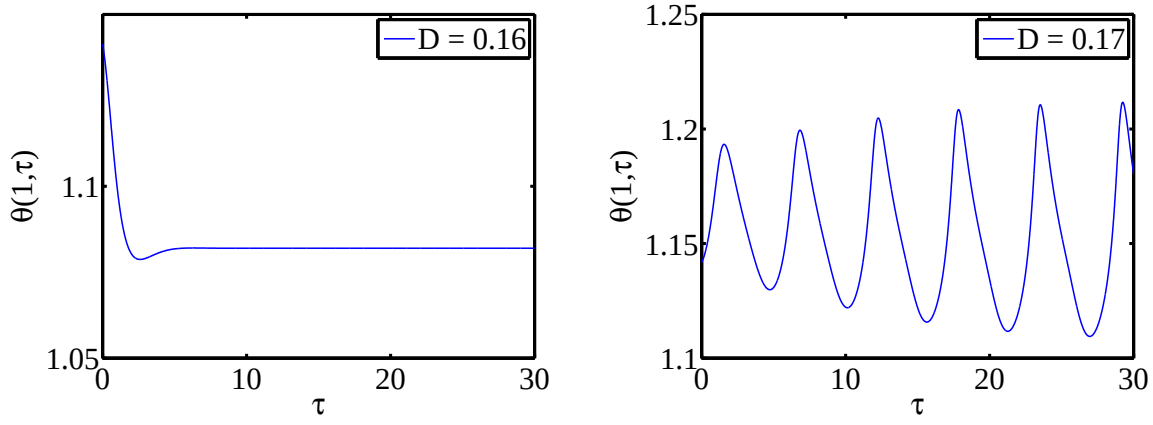

(a) $\mathcal{D} < \mathcal{D}^*$ (b) $\mathcal{D} > \mathcal{D}^*$

Figure 3-1: Time histories of exit temperature in the steady-state regime (a) and LCO regime (b)

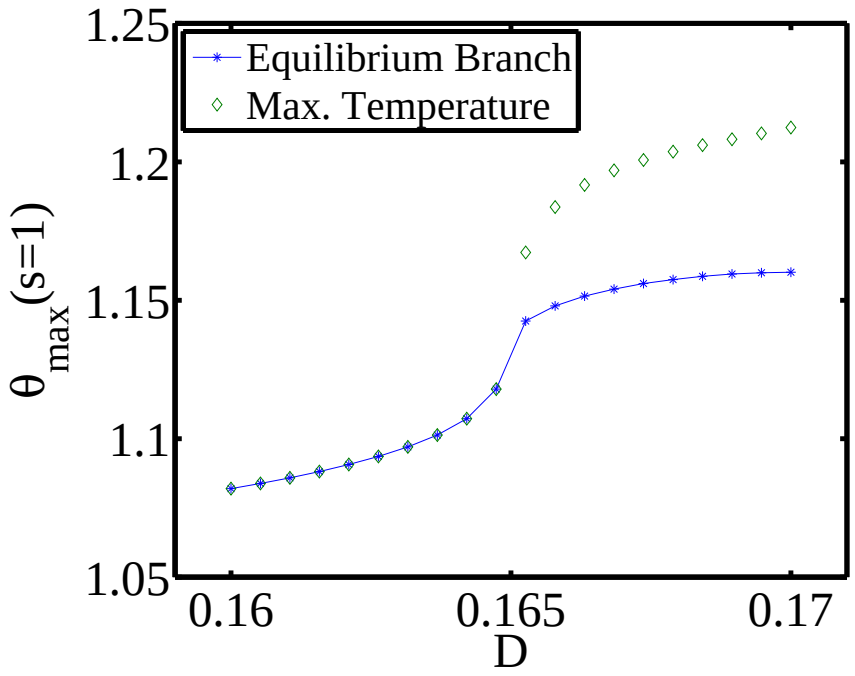

Figure 3-2: Bifurcation diagram of the tubular reactor model with respect to the Damköhler number $\mathcal{D}$ for $Pe = 5$, $\gamma = 25$, $B = 0.5$, $\beta = 2.5$ and $\theta_0 = 1$. The LCO amplitude at a given $\mathcal{D}$ value is the difference between the maximum exit temperature (green diamond) and the equilibrium position (blue asterisk). For $\mathcal{D} < 0.165$, the maximum exit temperatures and the equilibrium positions coinside, signifying steady state solutions. For $\mathcal{D} > 0.165$, stable oscillatory solutions with increasing LCO amplitudes are obtained.

3.1.2 Solution Method

The problem is discretized in the spatial domain with a resolution $\Delta s = \frac{1}{N+1}$, where N is the number of interior grid points. Furthermore, a discretized state vector $\boldsymbol{u}$ containing the concentration and temperature evaluated at the interior grid points is defined such that

$$\boldsymbol{u}(\tau) = \begin{bmatrix} \boldsymbol{y}(\tau) \\ \boldsymbol{\theta}(\tau) \end{bmatrix} \in \mathbb{R}^{2N\times 1}, \quad \text{with} \quad \boldsymbol{y} = \begin{bmatrix} y_1(\tau) \\ \vdots \\ y_N(\tau) \end{bmatrix} \in \mathbb{R}^{N\times 1}, \quad \text{and} \quad \boldsymbol{\theta} = \begin{bmatrix} \theta_1(\tau) \\ \vdots \\ \theta_N(\tau) \end{bmatrix} \in \mathbb{R}^{N\times 1}$$

where $y_i(\tau) = y(s_i, \tau)$ and $\theta_i(\tau) = \theta(s_i, \tau)$, with $s_i = i\Delta s$. To approximate the diffusion and convection terms, second-order centered difference is applied in the interior of the domain. Second-order forward and backward difference schemes are used for the inflow and outflow boundary conditions respectively. The semi-discrete form of the governing equations can be written as follows:

$$\frac{d\boldsymbol{u}}{d\tau} = \boldsymbol{A}\boldsymbol{u} + \boldsymbol{b} + \boldsymbol{F}(\boldsymbol{u}; \mathcal{D}) = \boldsymbol{R}(\boldsymbol{u}, \tau; \mathcal{D}) \tag{3.4}$$

where

$$\boldsymbol{A} = \begin{bmatrix} \boldsymbol{A^D} - \boldsymbol{A^C} & \boldsymbol{0} \\ \boldsymbol{0} & \boldsymbol{A^D} - \boldsymbol{A^C} - \beta\boldsymbol{I} \end{bmatrix} \in \mathbb{R}^{2N\times 2N}$$

with

$$\boldsymbol{A^D} = \frac{1}{Pe(\Delta s)^2} \begin{bmatrix} A^D_{1,1} & A^D_{1,2} & & & \\ 1 & -2 & 1 & & \\ & \ddots & \ddots & \ddots & \\ & & 1 & -2 & 1 \\ & & & A^D_{N,N-1} & A^D_{N,N} \end{bmatrix} \in \mathbb{R}^{N\times N}$$

$$\boldsymbol{A^C} = \frac{1}{2\Delta s}\begin{bmatrix} A^C_{1,1} & A^C_{1,2} & & & \\ -1 & 0 & 1 & & \\ & \ddots & \ddots & \ddots & \\ & & -1 & 0 & 1 \\ & & & A^C_{N,N-1} & A^C_{N,N} \end{bmatrix} \in \mathbb{R}^{N\times N}$$

$$A^D_{1,1} = \frac{4}{3+2Pe\Delta s} - 2 \qquad A^C_{1,1} = \frac{4}{3+2Pe\Delta s}$$
$$A^D_{1,2} = -\frac{1}{3+2Pe\Delta s} + 1 \qquad A^C_{1,2} = -\frac{1}{3+2Pe\Delta s} - 1$$
$$A^D_{N,N-1} = \frac{2}{3} \qquad A^C_{N,N-1} = \frac{4}{3}$$
$$A^D_{N,N} = -\frac{2}{3} \qquad A^C_{N,N} = -\frac{4}{3}$$

$$\boldsymbol{b} = \begin{bmatrix} \boldsymbol{b}_y \\ \boldsymbol{b}_\theta \end{bmatrix} \in \mathbb{R}^{2N\times 1}, \quad \text{with} \quad \boldsymbol{b}_y = \begin{bmatrix} b_0\mu \\ 0 \\ \vdots \\ 0 \end{bmatrix} \in \mathbb{R}^{N\times 1}, \quad \boldsymbol{b}_\theta = \begin{bmatrix} b_0 \\ \beta\theta_0 \\ \vdots \\ \beta\theta_0 \end{bmatrix} \in \mathbb{R}^{N\times 1}$$

$$\text{and} \quad b_0 = \frac{2+Pe\Delta s}{\Delta s(3+2Pe\Delta s)}$$

$$\boldsymbol{F}(\boldsymbol{u}) = \begin{bmatrix} -\mathcal{D}\boldsymbol{f}(\boldsymbol{u}) \\ \frac{B\mathcal{D}}{\mu}\boldsymbol{f}(\boldsymbol{u}) \end{bmatrix} \in \mathbb{R}^{2N\times 1}, \quad \text{with} \quad \boldsymbol{f}(\boldsymbol{u}) = \begin{bmatrix} f(y_1,\theta_1) \\ \vdots \\ f(y_N,\theta_N) \end{bmatrix} \in \mathbb{R}^{N\times 1},$$

$$\text{and} \quad f(y_i,\theta_i) = y_i e^{\gamma - \frac{\gamma}{\theta_i}}$$

Note that $A^D_{1,1}$, $A^D_{1,2}$, $A^D_{N,N-1}$, $A^D_{N,N}$, $A^C_{1,1}$, $A^C_{1,2}$, $A^C_{N,N-1}$, $A^C_{N,N}$, and b_0 arise due to one-sided finite-difference approximations at the two boundaries. The system of ordinary differential equations (ODEs) (3.4) can be integrated forward in time using any time-marching schemes. In this work, the explicit fourth-order Runge-Kutta (RK-4)

method with a constant stepsize $\Delta\tau$ is used:

$$\begin{aligned}
\bar{\boldsymbol{u}}_{n+\frac{1}{2}} &= \boldsymbol{u}_n + \frac{1}{2}\Delta\tau \boldsymbol{R}_n && (3.5)\\
\hat{\boldsymbol{u}}_{n+\frac{1}{2}} &= \boldsymbol{u}_n + \frac{1}{2}\Delta\tau \bar{\boldsymbol{R}}_{n+\frac{1}{2}} && (3.6)\\
\tilde{\boldsymbol{u}}_{n+1} &= \boldsymbol{u}_n + \frac{1}{2}\Delta\tau \hat{\boldsymbol{R}}_{n+\frac{1}{2}} && (3.7)\\
\boldsymbol{u}_{n+1} &= \boldsymbol{u}_n + \frac{1}{6}\Delta\tau[\boldsymbol{R}_n + 2(\bar{\boldsymbol{R}}_{n+\frac{1}{2}} + \hat{\boldsymbol{R}}_{n+\frac{1}{2}}) + \tilde{\boldsymbol{R}}_{n+1}] && (3.8)
\end{aligned}$$

where

$$\begin{aligned}
\boldsymbol{R}_n &= \boldsymbol{R}(\boldsymbol{u}_n, n\Delta\tau) && (3.9)\\
\bar{\boldsymbol{R}}_{n+\frac{1}{2}} &= \boldsymbol{R}\left(\bar{\boldsymbol{u}}_{n+\frac{1}{2}}, (n+\frac{1}{2})\Delta\tau\right) && (3.10)\\
\hat{\boldsymbol{R}}_{n+\frac{1}{2}} &= \boldsymbol{R}\left(\hat{\boldsymbol{u}}_{n+\frac{1}{2}}, (n+\frac{1}{2})\Delta\tau\right) && (3.11)\\
\tilde{\boldsymbol{R}}_{n+1} &= \boldsymbol{R}\left(\tilde{\boldsymbol{u}}_{n+1}, (n+1)\Delta\tau\right). && (3.12)
\end{aligned}$$

Starting with the initial conditions

$$\boldsymbol{u}_0 = \begin{bmatrix} \boldsymbol{y}_{in} \\ \boldsymbol{\theta}_{in} \end{bmatrix}, \tag{3.13}$$

the solution is time-integrated until the time-asymptotic behaviours such as steady states and LCO solutions are suitably established. To that end, a convergence criterion is imposed such that the absolute differences between the last and the second-last peaks as well as the last and third-last peaks of the exit temperature history is below a certain tolerance ϵ_{LCO}. For this study, $\epsilon_{LCO} = 10^{-3}$ is used. Note that the semi-discrete system (3.4) is of dimension $2N$ and that to evolve the solution forward in time using the RK-4 scheme, the nonlinear residual must be evaluated 4 times at each time level.

3.2 POD-DEIM Reduced Order Model

In this section, we apply both the original and modified POD-DEIM model reduction methodologies to the full-order model (FOM) in Section 3.1.2. Note that the POD-based reduced-order models (ROM) of this particular tubular reactor system have previously been studied by Beran et al. in [10] using the POD-Galerkin approach and Kalashnikova and Barone in [47] using POD with the best point interpolation method (BPIM).

3.2.1 Original POD-DEIM methodology

In this section, the offline-online model reduction strategy outlined in Section 2.1.3 is applied to the semi-discrete form of the governing equations (3.4), employing the original POD-DEIM approach. Firstly, the snapshot matrices $\mathbb{U} = \{\boldsymbol{u}_i\}_{i=1}^{n_s}$ for the state and $\mathbb{F} = \{\boldsymbol{F}_i\}_{i=1}^{n_s}$ for the nonlinear term are formed by performing the FOM simulations at selected values of the Damköhler number within its range of variations $\mathcal{D} \in [\mathcal{D}_{min}, \mathcal{D}_{max}]$. Using the POD method presented in Section 2.1.1, the state basis vectors $\boldsymbol{\Phi} = \{\boldsymbol{\phi}_i\}_{i=1}^{K}$ are computed from $\mathbb{U}$ and the nonlinear basis vectors $\boldsymbol{\Psi} = \{\boldsymbol{\psi}_i\}_{i=1}^{M}$ from $\mathbb{F}$, in which $K, M \ll 2N$ are determined based on their respective prescribed 'relative omitted energy' tolerances, as shown on (2.17). Next, the M interpolation indices $\vec{\mathbf{z}} = [z_1, \ldots, z_M]^T$ are computed using the point selection procedure described in Algorithm 1 in Section 2.1.2. The corresponding M' indices of $\vec{\mathbf{z}}' \in \mathbb{R}^{M' \times 1}$ for the state are then derived from $\vec{\mathbf{z}}$ based on nodal connectivity of the problem. In this particular problem, the nonlinear reaction term at a given grid point depends on both state components at that point. Therefore, $M' \leq 2M$. The equality holds only when *all* of the M interpolation points reside on different grid points. To construct the ROM of the system, the state $\boldsymbol{u}$ is first approximated as a linear combination of its basis functions:

$$\boldsymbol{u} \approx \boldsymbol{\Phi} \boldsymbol{u}_r \tag{3.14}$$

where

$$\mathbf{\Phi} = [\boldsymbol{\phi}_1, \boldsymbol{\phi}_2, \ldots, \boldsymbol{\phi}_K] \in \mathbb{R}^{2N \times K}, \quad \mathbf{u}_r = [\tilde{u}_1, \tilde{u}_2, \ldots, \tilde{u}_K] \in \mathbb{R}^{K \times 1} \tag{3.15}$$

Substituting the approximation above into the FOM (3.4) and apply Galerkin projection, the POD-Galerkin ROM is obtained as follows:

$$\frac{d\boldsymbol{u}_r}{d\tau} = \underbrace{\mathbf{\Phi}^T \mathbf{A} \mathbf{\Phi}}_{\mathbf{A}_r} \boldsymbol{u}_r + \underbrace{\mathbf{\Phi}^T \boldsymbol{b}}_{\boldsymbol{b}_r} + \underbrace{\mathbf{\Phi}^T \boldsymbol{F}(\mathbf{\Phi} \boldsymbol{u}_r; \mathcal{D})}_{\boldsymbol{F}_r} \tag{3.16}$$

where $\mathbf{A}_r = \mathbf{\Phi}^T \mathbf{A} \mathbf{\Phi} \in \mathbb{R}^{K \times K}$, $\boldsymbol{b}_r = \mathbf{\Phi}^T \boldsymbol{b} \in \mathbb{R}^{K \times 1}$ and $\boldsymbol{F}_r = \mathbf{\Phi}^T \mathbf{F}(\mathbf{\Phi} \boldsymbol{u}_r; \mathcal{D}) \in \mathbb{R}^{K \times 1}$. The initial condition (3.13) is also projected onto the reduced basis:

$$\boldsymbol{u}_r(\tau = 0) = \mathbf{\Phi}^T \boldsymbol{u}_0 \tag{3.17}$$

To obtain an efficient ROM, we further approximate the reduced nonlinear term using DEIM as shown in (2.23). The POD-DEIM reduced-order model can then be expressed as:

$$\frac{d\boldsymbol{u}_r}{d\tau} = \underbrace{\mathbf{A}_r}_{K \times K} \boldsymbol{u}_r + \boldsymbol{b}_r + \underbrace{\mathbf{B}_r}_{K \times M} \underbrace{\boldsymbol{F}_{\vec{\mathbf{z}}}(\underbrace{\mathbf{\Phi}_{\vec{\mathbf{z}}'} \boldsymbol{u}_r}_{M' \times 1}; \mathcal{D})}_{M \times 1} \tag{3.18}$$

where

$$\mathbf{B}_r = \mathbf{\Phi}^T \mathbf{\Psi} \mathbf{\Psi}_{\vec{\mathbf{z}}}^{-1} \in \mathbb{R}^{K \times M} \tag{3.19}$$

and $\boldsymbol{F}_{\vec{\mathbf{z}}}$ is the nonlinear term evaluated at M interpolation points specified by $\vec{\mathbf{z}}$, $\mathbf{\Psi}_{\vec{\mathbf{z}}}$ contains the corresponding M rows of $\mathbf{\Psi}$. $\mathbf{\Phi}_{\vec{\mathbf{z}}'}$ contains M' rows of $\mathbf{\Phi}$ specified by $\vec{\mathbf{z}}'$. Given a particular Damköhler number $\mathcal{D}$, the ROM (3.18) can be time-integrated forward using the explicit RK-4 method described in Section 3.1.2. Note that the parameter independent matrices $\mathbf{A}_r$ and $\mathbf{B}_r$ are both formed in the offline phase, immediately after the $\mathbf{\Phi}$, $\mathbf{\Psi}$ and $\vec{\mathbf{z}}$ have been computed from the snapshots. The online computation of the reduced nonlinear term involves the evaluations of M out of a total of $2N$ components of the full-order nonlinear term. To do so, M' components of the

state solution must also be reconstructed online. Since $K, M, M' \ll 2N$, the online evaluation of the K-dimensional ROM (3.18) constructed with the original POD-DEIM methodology can be performed efficiently at a computational cost independent of the FOM dimension.

3.2.2 Modified POD-DEIM methodology

A different ROM can be constructed using the modified POD-DEIM methodology outlined in Section 2.2 with scalar-valued POD modes and DEIM over-sampling. The snapshot matrices for the state ($\mathbb{U}$) and the nonlinear term ($\mathbb{F}$) can be populated in the same manner as discussed in the previous section by simulating the FOM. $\mathbb{U}$ and $\mathbb{F}$ are then separated into 2 smaller scalar-valued matrices for each unknown variable:

$$\mathbb{U} \in \mathbb{R}^{2N \times n_s} \quad \longmapsto \quad \mathbb{U}^y, \mathbb{U}^\theta \in \mathbb{R}^{N \times n_s} \tag{3.20}$$

$$\mathbb{F} \in \mathbb{R}^{2N \times n_s} \quad \longmapsto \quad \mathbb{F}^y, \mathbb{F}^\theta \in \mathbb{R}^{N \times n_s} \tag{3.21}$$

Scalar-valued POD modes for the state and the nonlinear term are generated from these snapshot matrices using the POD method:

$$\mathbb{U}^y \quad \longmapsto \quad \boldsymbol{\Phi}^y \in \mathbb{R}^{N \times K_y}, \quad \mathbb{U}^\theta \quad \longmapsto \quad \boldsymbol{\Phi}^\theta \in \mathbb{R}^{N \times K_\theta} \tag{3.22}$$

$$\mathbb{F}^y \quad \longmapsto \quad \boldsymbol{\Psi}^y \in \mathbb{R}^{N \times M_y}, \quad \mathbb{F}^\theta \quad \longmapsto \quad \boldsymbol{\Psi}^\theta \in \mathbb{R}^{N \times M_\theta} \tag{3.23}$$

where the numbers of POD basis vectors for the state (K_y and K_θ) and the nonlinear term (M_y and M_θ) are all determined by their respective 'relative omitted energy' criterion (2.17). The state $\boldsymbol{u}$ as defined in Section 3.1.2 can be approximated as follows:

$$\boldsymbol{u} \approx \tilde{\boldsymbol{\Phi}} \boldsymbol{u}_r \tag{3.24}$$

where

$$\tilde{\boldsymbol{\Phi}} = diag\{\boldsymbol{\Phi}^y, \boldsymbol{\Phi}^\theta\} \in \mathbb{R}^{2N \times \tilde{K}} \tag{3.25}$$

$$\boldsymbol{u}_r = \begin{bmatrix} \boldsymbol{u}_r^y \\ \boldsymbol{u}_r^\theta \end{bmatrix} \in \mathbb{R}^{\tilde{K} \times 1} \tag{3.26}$$

and $\tilde{K} = K_y + K_\theta$. To formulate an efficient approximation of the nonlinear term, the DEIM interpolation point section algorithm from Section 2.1.2 is applied to each scalar-valued POD basis for the nonlinear terms $\boldsymbol{\Psi}^y$ and $\boldsymbol{\Psi}^\theta$, generating two sets of interpolation indices:

$$\boldsymbol{\Psi}^y \longmapsto \vec{\mathbf{z}}_y \in \mathbb{R}^{M_y \times 1}, \quad \boldsymbol{\Psi}^\theta \longmapsto \vec{\mathbf{z}}_\theta \in \mathbb{R}^{M_\theta \times 1} \tag{3.27}$$

Using the 'node-based' selection method described in Section 2.2.2, we require both components of the nonlinear term at a particular node to be selected as long as one of them is selected by either $\vec{\mathbf{z}}_y$ or $\vec{\mathbf{z}}_\theta$. Therefore, the interpolation indices for both variables of the nonlinear term are:

$$\hat{\mathbf{z}} = \vec{\mathbf{z}}_y \bigcup \vec{\mathbf{z}}_\theta \ \in \mathbb{R}^{\hat{M} \times 1} \tag{3.28}$$

where $M_y, M_\theta \leq \hat{M} \ll 2N$, resulting in more sample points than the number of POD modes within each variable of the nonlinear term. The nonlinear term $\boldsymbol{F}$ can then be approximated under the over-sampling framework (Section 2.2.2) as follows:

$$\boldsymbol{F} = \begin{bmatrix} \boldsymbol{F}^y \\ \boldsymbol{F}^\theta \end{bmatrix} \approx \begin{bmatrix} \boldsymbol{\Psi}^y (\boldsymbol{\Psi}^y_{\hat{\mathbf{z}}})^+ \boldsymbol{F}^y_{\hat{\mathbf{z}}} \\ \boldsymbol{\Psi}^\theta (\boldsymbol{\Psi}^\theta_{\hat{\mathbf{z}}})^+ \boldsymbol{F}^\theta_{\hat{\mathbf{z}}} \end{bmatrix} = \begin{bmatrix} \boldsymbol{\Psi}^y (\boldsymbol{\Psi}^y_{\hat{\mathbf{z}}})^+ & 0 \\ 0 & \boldsymbol{\Psi}^\theta (\boldsymbol{\Psi}^\theta_{\hat{\mathbf{z}}})^+ \end{bmatrix} \begin{bmatrix} \boldsymbol{F}^y_{\hat{\mathbf{z}}} \\ \boldsymbol{F}^\theta_{\hat{\mathbf{z}}} \end{bmatrix} \tag{3.29}$$

Substituting the approximations (3.24) and (3.29) into the FOM (3.4) and performing Galerkin projection, the modified POD-DEIM ROM with scalar-valued POD modes

and over-sampling is:

$$\frac{d\boldsymbol{u}_r}{d\tau} = \underbrace{\hat{\mathbf{A}}_r}_{\tilde{K}\times\tilde{K}}\boldsymbol{u}_r + \tilde{\boldsymbol{b}}_r + \underbrace{\hat{\mathbf{B}}_r}_{\tilde{K}\times 2\hat{M}} \underbrace{\boldsymbol{F}_{\hat{\mathbf{z}}}(\underbrace{\tilde{\boldsymbol{\Phi}}_{(\hat{\mathbf{z}}')_g}\boldsymbol{u}_r}_{\hat{M}'\times 1};\mathcal{D})}_{2\hat{M}\times 1} \tag{3.30}$$

where

$$\hat{\mathbf{A}}_r = \tilde{\boldsymbol{\Phi}}^T\mathbf{A}\tilde{\boldsymbol{\Phi}} \in \mathbb{R}^{\tilde{K}\times\tilde{K}} \tag{3.31}$$

$$\hat{\mathbf{B}}_r = \tilde{\boldsymbol{\Phi}}^T diag\{\boldsymbol{\Psi}^y(\boldsymbol{\Psi}^y_{\hat{\mathbf{z}}})^+, \boldsymbol{\Psi}^\theta(\boldsymbol{\Psi}^\theta_{\hat{\mathbf{z}}})^+\} \in \mathbb{R}^{\tilde{K}\times 2\hat{M}} \tag{3.32}$$

$$\tilde{\boldsymbol{b}}_r = \tilde{\boldsymbol{\Phi}}^T\boldsymbol{b} \in \mathbb{R}^{\tilde{K}\times 1} \tag{3.33}$$

$$\boldsymbol{F}_{\hat{\mathbf{z}}} = \begin{bmatrix}\boldsymbol{F}^y_{\hat{\mathbf{z}}}\\ \boldsymbol{F}^\theta_{\hat{\mathbf{z}}}\end{bmatrix} \in \mathbb{R}^{2\hat{M}\times 1} \tag{3.34}$$

and $(\hat{\mathbf{z}}')_g \in \mathbb{R}^{\hat{M}'\times 1}$ contains the global indices of the all the state variables that must be reconstructed online as determined from $\hat{\mathbf{z}}$ based on nodal connectivity. Note that in this problem, both components of the nonlinear term at a given node are only a function of the two state components at that node. Therefore, $\hat{M}' = 2\hat{M}$. The cost of the online evaluation of this ROM is a function of $\tilde{K}, \hat{M} \ll 2N$. This ROM is to be compared with the original POD-DEIM ROM (3.18) derived in the last subsection. In the next section, we compare the performances of the two ROMs for problems with equal and disparate magnitudes in the two unknown variables.

3.3 Numerical Results

In this section, both the original and modified POD-DEIM methodologies derived in Section 3.2 are applied to perform model reduction on the nonlinear CDR system described in Section 3.1. Two test cases are considered here. In the first case, the ROM is constructed for a system with equal magnitudes in both unknown variables ($\mu = 1$). In the second test case, the scaling parameter μ is set to 10^{-4}, making the temperature variable (θ) four orders of magnitude larger than the concentration (y).

In both cases, the system parameters $Pe = 5$, $\gamma = 25$, $B = 0.5$, $\beta = 2.5$ and $\theta_0 = 1$ are held constant while the Damköhler number $\mathcal{D}$ varies in the range $[0.16, 0.17]$. The spatial domain is discretized into 100 equal intervals, resulting in the FOM dimension of $2N = 198$. A constant step-size of $\Delta\tau_{FOM} = 2.5 \times 10^{-4}$ for the FOM is used for the RK-4 time-marching scheme, in order to maintain numerical stability.

The accuracies of both ROMs are quantified by comparing its outputs of interest — the LCO amplitudes and equilibrium positions with those of the FOM. To that effect, we compute the absolute relative error as:

$$|\epsilon_{rel}| = \frac{|\ell^{ROM} - \ell^{FOM}|}{|\ell^{FOM}|} \tag{3.35}$$

where ℓ denotes an output of interest.

3.3.1 Unknown variables with equal magnitudes ($\mu = 1$)

The ROMs (3.18) and (3.30) are constructed with two sets of snapshots obtained by simulating the FOM at the two extreme points of its parameter domain: $\mathcal{D} = 0.16$ and 0.17. For each unsteady simulation, the FOM is time-marched using the RK-4 scheme at $\Delta\tau_{FOM} = 2.5 \times 10^{-4}$ until the solution converges to either a steady state or a stable limit cycle. The snapshots of the state and nonlinear term are stored at every 1000 time steps. For the original POD-DEIM ROM, a tolerance on the relative omitted energy $\epsilon_u = 10^{-11}$ is imposed for the state while $\epsilon_f = 10^{-10}$ is given for the nonlinear term, resulting in the inclusions of $K = 10$ state POD modes and $M = 10$

POD modes for the nonlinear term. For the modified POD-DEIM ROM, the relative omitted energy levels imposed for the scalar-valued POD modes of the state and the nonlinear term are: $\epsilon_u^y = \epsilon_u^\theta = 10^{-11}$ and $\epsilon_f^y = \epsilon_f^\theta = 10^{-10}$. As a result, $K_y = 8$, $K_\theta = 7$, $M_y = 10$, and $M_\theta = 10$. A '$\mathcal{D}$-sweep' is performed in which the FOM and the ROMs are solved at 20 equi-spaced $\mathcal{D}$ values in the interval $\mathcal{D} \in [0.16, 0.17]$. Note that due to the truncation of high-frequency modes, a larger stepsize of $\Delta\tau_{ROM} = 1.0 \times 10^{-2}$ can be used in the time-integration of the two ROMs. Figure 3-3 shows the maximum exit temperatures and equilibrium positions at each $\mathcal{D}$ value computed using FOM and the original POD-DEIM ROM. A Hopf-bifurcation can be observed around $\mathcal{D}^* = 0.165$. For $\mathcal{D} > \mathcal{D}^*$, stable oscillatory solutions are obtained. The LCO amplitude is the difference between the maximum exit temperature and the equilibrium position. The FOM and ROM results are observed to be in excellent agreement for all points within $\mathcal{D} \in [0.16, 0.17]$, even though the ROM is generated only with snapshots taken at $\mathcal{D} = 0.16$ and 0.17. Figure 3-4(a) shows that all outputs except for the two closest to the bifurcation point are computed with relative errors below 10^{-4}. The errors are slightly higher around $\mathcal{D}^* = 0.165$ because the convergence towards a stable limit cycle at these points takes many thousands of time steps to achieve, giving rise to long-time integration errors in the ROM. The ROM constructed using the original POD-DEIM methodology reduces the computational time by two orders of magnitude from the FOM, as shown on Figure 3-4(b). Note that the ability to use a larger step-size ($\Delta\tau_{ROM} = 40\Delta\tau_{FOM}$) for the explicit time-marching scheme is a major contributor to the speed-up in this problem. The speed-up effected by the reductions in system dimensions ($2N = 198$ in FOM vs. $K = 10$ in ROM) is less significant as the FOM dimension is already rather small.

Note that in this test case, both ROMs yield the same order of accuracy with the modified POD-DEIM ROM having marginally lower speed-up factors. For simplicity, only the comparison results between the FOM and the original POD-DEIM ROM are shown here. We defer the comparisons involving the modified POD-DEIM ROM for the next test case in which the difference in performance between the two ROMs is more apparent.

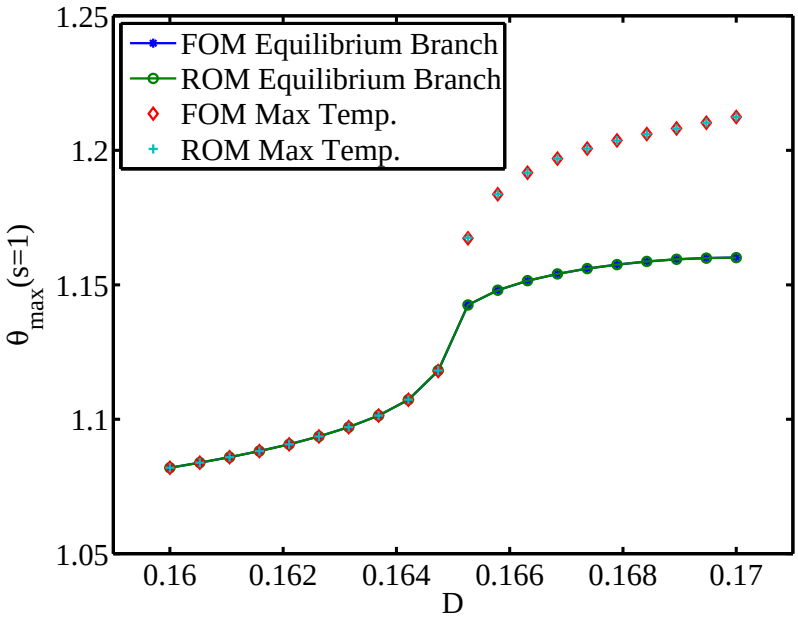

Figure 3-3: Comparison between the bifurcation diagrams computed using the FOM ($\mu = 1$) and the original POD-DEIM ROM ($K = 10, M = 10$) for the tubular reactor system with $Pe = 5$, $\gamma = 25$, $B = 0.5$, $\beta = 2.5$ and $\theta_0 = 1$, in $\mathcal{D} \in [0.16, 0.17]$

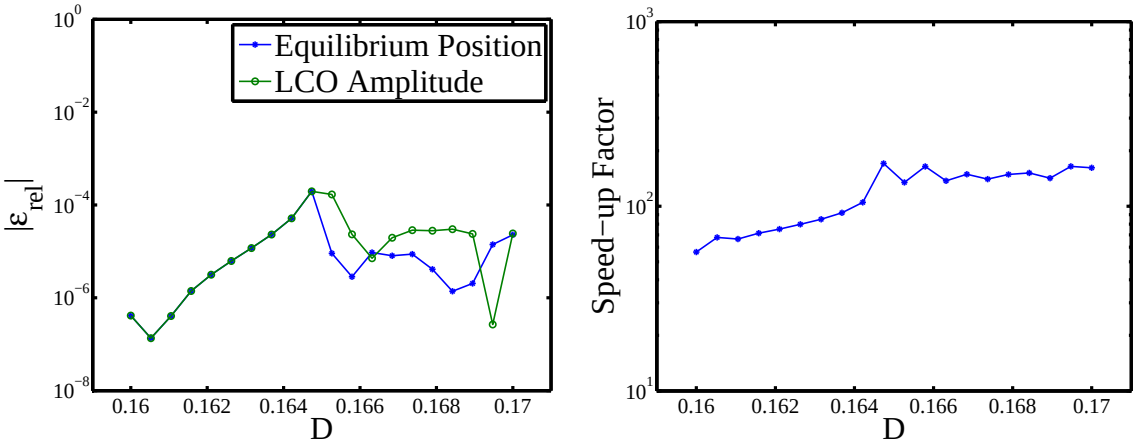

(a) Relative Error

(b) Speed-up

Figure 3-4: Relative error and speed-up over FOM ($\mu = 1$) in computing the LCO amplitudes and equilibrium positions, using the original POD-DEIM ROM with $K = 10$ and $M = 10$.

3.3.2 Unknown variables with different magnitudes ($\mu = 10^{-4}$)

In this test case, the scaling parameter μ is set to 10^{-4}, resulting in four orders of magnitude difference between the temperature and concentration variables. The snapshots are collected in the same manner as described in the previous test case. The numbers of POD modes for the state and the nonlinear term for both ROMs are also the same as the first test case. The degradation of accuracy in the original POD-DEIM ROM is shown on the bifurcation diagram on Figure 3-5 where significant discrepancies between the FOM and ROM results are apparent, especially in the predicted equilibrium positions. Comparing the accuracy of the original POD-DEIM ROM in the equal-magnitude case ($\mu = 1$) in Figure 3-6(a) to the $\mu = 10^{-4}$ case in Figure 3-6(b), it can be observed that the relative errors increase two orders of magnitude due to the disparate magnitudes between the temperature and concentration. The speed-up factors are the same as the first test case (see Figure 3-4(b)) since the same step-size and numbers of POD modes are used. On the other hand, the results obtained using the modified POD-DEIM ROM are in excellent agreement with those of the FOM, as shown on Figure 3-7. The relative errors, as shown on Figure 3-8(a) are all of $O(10^{-4})$ — the same order as the equal-magnitude case. Figure 3-8(b) shows that the speed-up factors of $O(10^2)$ are achieved for all points tested, only marginally lower than the original POD-DEIM ROM (see Figure 3-4(b)). This test case demonstrates that the modified POD-DEIM ROM with scalar-valued POD modes and over-sampling is more robust for problems in which disparate magnitudes exist among unknown variables.

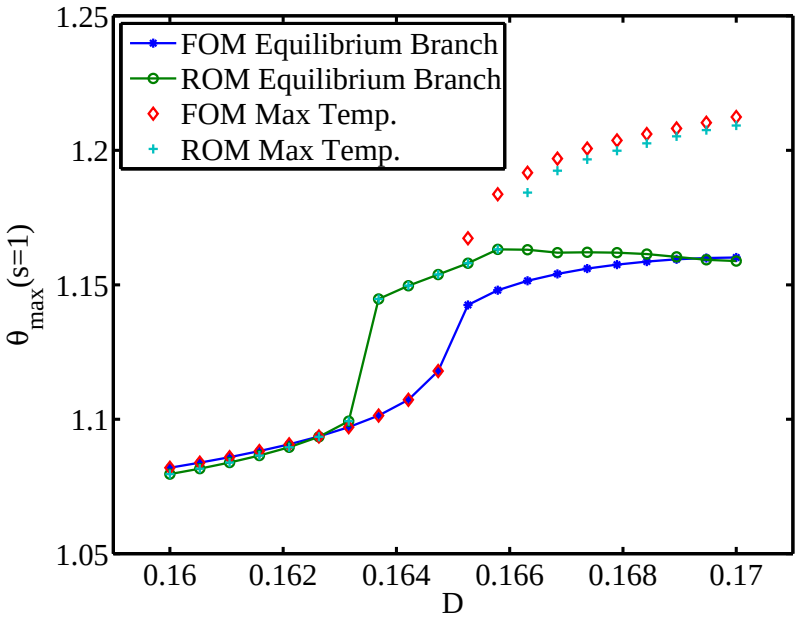

Figure 3-5: Comparison between the bifurcation diagrams computed using the FOM ($\mu = 10^{-4}$) and the original POD-DEIM ROM ($K = 10, M = 10$) for the tubular reactor system with $Pe = 5$, $\gamma = 25$, $B = 0.5$, $\beta = 2.5$ and $\theta_0 = 1$, in $\mathcal{D} \in [0.16, 0.17]$

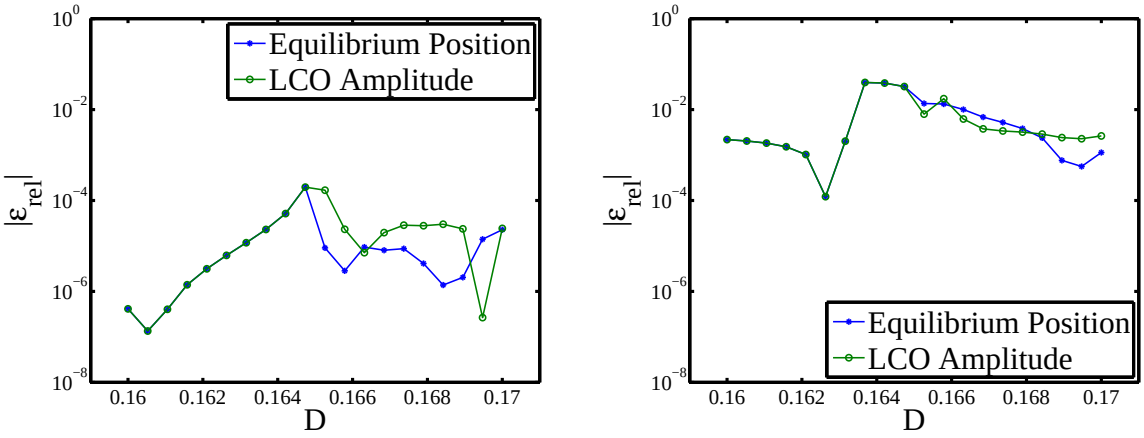

(a) $\mu = 1$ (b) $\mu = 10^{-4}$

Figure 3-6: Relative errors in computing the LCO amplitudes and equilibrium positions using the original POD-DEIM ROM for the equal-magnitude case ($\mu = 1$) and the different-magnitude case ($\mu = 10^{-4}$)

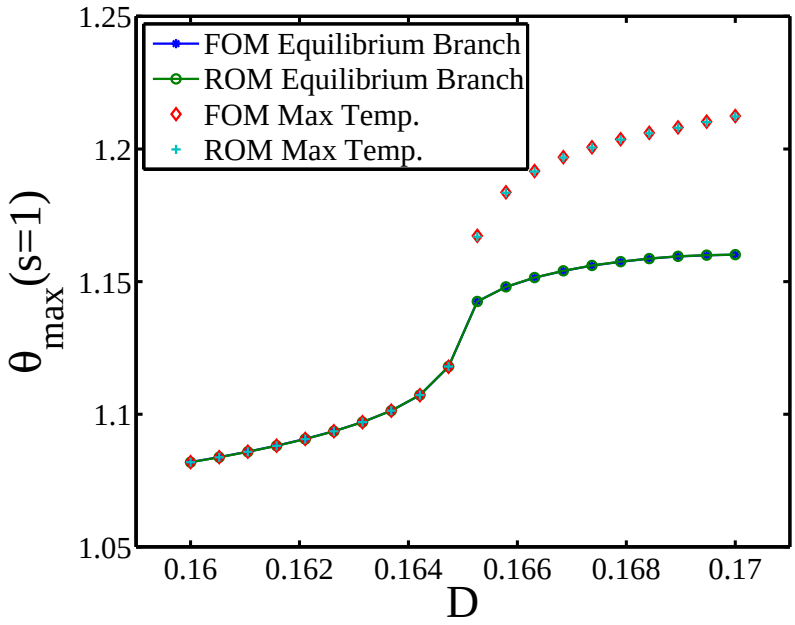

Figure 3-7: Comparison between the bifurcation diagrams computed using the FOM ($\mu = 10^{-4}$) and the modified POD-DEIM ROM ($K_y = 8$, $K_\theta = 7$, $M_y = 10$, $M_\theta = 10$) for the tubular reactor system with $Pe = 5$, $\gamma = 25$, $B = 0.5$, $\beta = 2.5$ and $\theta_0 = 1$, in $\mathcal{D} \in [0.16, 0.17]$

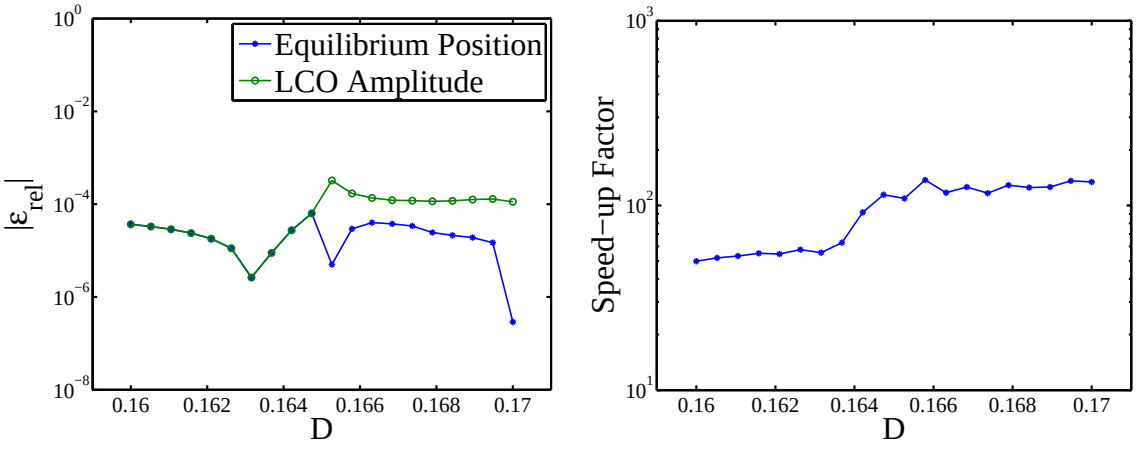

(a) Relative Error

(b) Speed-up

Figure 3-8: Relative error and speed-up over FOM ($\mu = 10^{-4}$) in computing the LCO amplitudes and equilibrium positions, using the modified POD-DEIM ROM with $K_y = 8$, $K_\theta = 7$, $M_y = 10$ and $M_\theta = 10$.

Chapter 4

Aeroelastic Limit Cycle Oscillations

This chapter applies the modified POD-DEIM model reduction methodology developed in the Chapter 2 to an aeroelastic system that exhibits limit cycle oscillations (LCO). The problem set-up and governing equations are described in Section 4.1.1. An implicit time-integration scheme is presented in Section 4.1.2 to solve the equations of motion to obtain time-asymptotic values such as the LCO amplitudes and equilibrium positions. In Section 4.1.3, the 'direct flutter computation' is introduced to obtain the flutter points via eigen-analysis of the aeroelastic system. Section 4.2 applies the modified POD-DEIM model reduction approach to reduce the computational costs of the two aforementioned tasks. Finally, numerical results involving systems with fixed parameters, as well as one, two and three parameters are presented in Section 4.3.

4.1 Full Order Model

To simulate the aeroelastic LCO behaviour, a simplified aero-structural model consisting of a rectangular cantilevered plate in quasi-steady supersonic flow is considered in this work. Figure 4-1 shows a schematic of the model. The rectangular plate has a uniform thickness of h, a width (chord length) c and a length (semi-span) L in the x and y directions respectively. The incoming supersonic flow is along the x direction. This is the same model that has been considered in the works by [32] and [75].

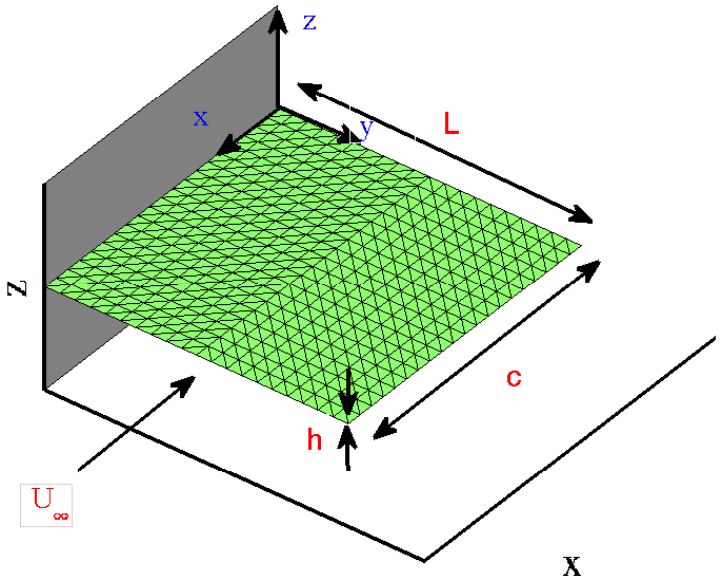

Figure 4-1: Cantilevered plate in supersonic flow

4.1.1 Governing Equations

The equations of motion that govern the out-of-plane displacement w of a thin plate are [29]:

$$\rho_s h\frac{\partial^2 w}{\partial t^2}+D\nabla^4 w=\frac{12D}{h^2}\left[(\varepsilon_{xx}+\nu\varepsilon_{yy})\frac{\partial^2 w}{\partial x^2}+2(1-\nu)\varepsilon_{xy}\frac{\partial^2 w}{\partial x\partial y}+(\varepsilon_{yy}+\nu\varepsilon_{xx})\frac{\partial^2 w}{\partial y^2}\right]+p_{aero} \tag{4.1}$$

$$\frac{\partial}{\partial x}(\varepsilon_{xx}+\nu\varepsilon_{yy})+(1-\nu)\frac{\partial \varepsilon_{xy}}{\partial y}=0 \tag{4.2}$$

$$\frac{\partial}{\partial y}(\varepsilon_{yy}+\nu\varepsilon_{xy})+(1-\nu)\frac{\partial \varepsilon_{xy}}{\partial x}=0 \tag{4.3}$$

where ρ_s is the density of the plate, $D=Eh^3/(12(1-\nu^2))$ is the plate rigidity, E is the modulus of elasticity, h is the plate thickness, ν is the Poisson's ratio, p_{aero} is the external loading exerted by aerodynamic pressure, and ε_{xx}, ε_{yy} and ε_{xy} are the internal strains. As discussed in Section 1.1, for the system to exhibit LCO behaviour, nonlinearities in the flow and/or the structure must be present to limit the growth of vibrational amplitude after an initial disturbance. In this model, such nonlinear mechanism is represented by the von Kármán strains in the plate which couple the in-plane and out-of-plane deformations as follows:

$$\varepsilon_{xx} = \frac{\partial u}{\partial x}+\frac{1}{2}\left(\frac{\partial w}{\partial x}\right)^2 \tag{4.4}$$

$$\varepsilon_{yy} = \frac{\partial v}{\partial y}+\frac{1}{2}\left(\frac{\partial w}{\partial y}\right)^2 \tag{4.5}$$

$$\varepsilon_{xy} = \frac{1}{2}\left(\frac{\partial v}{\partial x}+\frac{\partial u}{\partial y}+\frac{\partial w}{\partial x}\frac{\partial w}{\partial y}\right)^2 \tag{4.6}$$

where u, v and w are displacements in the x, y and z directions respectively.

The aerodynamic pressure p_{aero} is modeled by the linearized supersonic piston theory originally formulated by Ashley and Zartarian in [3]:

$$p_{aero}=\frac{2\rho_\infty U_\infty^2}{\sqrt{M_\infty^2-1}}\frac{\partial w}{\partial x}+\frac{2\rho_\infty U_\infty(M_\infty^2-2)}{(M_\infty^2-1)^{3/2}}\frac{\partial w}{\partial t} \tag{4.7}$$

where ρ_∞, U_∞ and M_∞ are freestream flow density, velocity and Mach number respectively. Spatial discretization using the finite element method results in the following system of nonlinear second-order ODEs:

$$\boldsymbol{M}\ddot{\boldsymbol{u}} + \boldsymbol{C}_s\dot{\boldsymbol{u}} + \boldsymbol{f}(\boldsymbol{u}) = \boldsymbol{f}_{aero}(\boldsymbol{u}, \dot{\boldsymbol{u}}) \tag{4.8}$$

where the plate is discretized into triangular elements. Each node on the computational grid contains 6 degrees of freedom (DOF). Therefore the generalized displacement vector is organized such that

$$\boldsymbol{u} = \begin{bmatrix} \boldsymbol{u^1} \\ \vdots \\ \boldsymbol{u^6} \end{bmatrix} \in \mathbb{R}^{6\mathcal{N}\times 1} \tag{4.9}$$

where $\boldsymbol{u}^i \in \mathbb{R}^{\mathcal{N}\times 1}$ and $\mathcal{N}$ is the number of finite element nodes. Note that for the generalized displacement, these 6 DOFs correspond to the displacements from undeflected position in the x, y and z directions and the rotations about the x, y and z axes. In particular, for the i-th DOF, $\boldsymbol{u}^i$ contains the generalized displacement of that DOF evaluated at all $\mathcal{N}$ grid points. Within each triangular element, the in-plane response is modeled by the linear strain triangle (LST) while the out-of-plane bending response is modeled by the discrete Kirchhoff triangle (DKT). Thus discretized, $\boldsymbol{M}$ is the resultant consistent mass matrix, $\boldsymbol{C}_s$ is the structural damping matrix. In this structural model, proportional damping is assumed such that $\boldsymbol{C}_s = \beta_s\boldsymbol{M}$, where β_s is the structural damping coefficient. $\boldsymbol{f(u)}$ is a vector of nonlinear internal forces due to the von Kármán strains which couple the in-plane stretching and out-of-plane bending responses as shown in (4.4)–(4.6). It is assembled as a global vector from $\mathcal{N}$ nodal forces in the same manner as the state $\boldsymbol{u}$:

$$\boldsymbol{f} = \begin{bmatrix} \boldsymbol{f^1} \\ \vdots \\ \boldsymbol{f^6} \end{bmatrix} \in \mathbb{R}^{6\mathcal{N}\times 1} \tag{4.10}$$

where $\boldsymbol{f}^i \in \mathbb{R}^{\mathcal{N}\times 1}$. The 6 DOFs of $\boldsymbol{f}$ correspond to the forces in the x, y and z directions and the moments about the x, y and z axes.

The aerodynamic pressure force vector $\boldsymbol{f_{aero}(u, \dot{u})}$ can be approximated from (4.7) as:

$$\boldsymbol{f}_{aero}(\boldsymbol{u}, \dot{\boldsymbol{u}}) = -\underbrace{\frac{2\rho_\infty U_\infty^2}{\sqrt{M_\infty^2 - 1}}\boldsymbol{A_x}}_{\boldsymbol{K}_{aero}}\boldsymbol{u} - \underbrace{\frac{2\rho_\infty U_\infty (M_\infty^2 - 2)}{(M_\infty^2 - 1)^{3/2}}\boldsymbol{A_t}}_{\boldsymbol{C}_{aero}}\dot{\boldsymbol{u}} \tag{4.11}$$

where $\boldsymbol{A_x}$ and $\boldsymbol{A_t}$ are matrices that approximate the gradient and time derivative terms in (4.7) at the center of each triangular element and distribute the integrated pressure at each node. Moreover, $\boldsymbol{K}_{aero}$ and $\boldsymbol{C}_{aero}$ are defined as the aerodynamic stiffness and damping matrices. Substituting (4.11) into (4.8), the equations of motion can be expressed as:

$$\boldsymbol{M}\ddot{\boldsymbol{u}} + (\boldsymbol{C}_s + \boldsymbol{C}_{aero})\dot{\boldsymbol{u}} + \boldsymbol{K}_{aero}\boldsymbol{u} + \boldsymbol{f}(\boldsymbol{u}) = \boldsymbol{0} \tag{4.12}$$

The above equation of motion was used in the design-for-reliability study by [75] to model the same supersonic plate problem in which the incoming flow was assumed to be parallel to the undeformed plate. This numerical model can be extended to include the effect of a steady angle of attack[2] (α_o) by the addition of the following constant aerodynamic forcing term:

$$\boldsymbol{f}_\alpha = -\boldsymbol{K}_{aero}^{\alpha}\alpha_o \tag{4.13}$$

where $\boldsymbol{K}_{aero}^{\alpha}$ is a matrix that projects the aerodynamic forces onto the vertical axis through an angle α_o. Note that the angle of attack here is assumed to be small and that $\boldsymbol{f}_\alpha$ is a constant forcing vector at a given α_o. The equation of motion of a nonlinear cantilevered plate in supersonic flow inclined at a small steady angle of attack is:

$$\boldsymbol{M}\ddot{\boldsymbol{u}} + (\boldsymbol{C}_s + \boldsymbol{C}_{aero})\dot{\boldsymbol{u}} + \boldsymbol{K}_{aero}\boldsymbol{u} + \boldsymbol{f}_\alpha + \boldsymbol{f}(\boldsymbol{u}) = \boldsymbol{0} \tag{4.14}$$

[2]initial angle of attack of the undeformed plate

It is worthwhile to point out the functional dependence of the terms in the equation above on various flow and structural parameters. First, we introduce the following non-dimensional parameters:

$$\lambda = \frac{2\rho_\infty U_\infty^2 c^3}{D_o\sqrt{M_\infty^2-1}} \tag{4.15}$$

$$\mu = \frac{2\rho_\infty c}{\rho_s h_o} \tag{4.16}$$

where λ is the non-dimensional dynamic pressure parameter and μ is the mass ratio. Note that $D_o = Eh_o^3/(12(1-\nu^2))$ is the plate rigidity defined based on a fixed baseline uniform plate thickness h_o. Using these non-dimensional parameters, the functional relationships of different terms in (4.14) can be expressed as follows:

$$\boldsymbol{M}, \boldsymbol{C_s} = f(h, \rho_s, \beta) \tag{4.17}$$

$$\boldsymbol{K_{aero}}, \boldsymbol{C_{aero}} = f(M_\infty, \lambda, \mu, c) \tag{4.18}$$

$$\boldsymbol{f(u)} = f(D, \boldsymbol{u}) \tag{4.19}$$

Note that the nonlinear internal force $\boldsymbol{f(u)}$ is a function of both plate rigidity D and state $\boldsymbol{u}$. The latter is in turn dependent on all other flow and structural parameters. As will be shown in the following sections, the LCO amplitude of the plate is a function of the λ parameter. In particular, when all other system parameters are held constant, there exists a critical dynamic pressure λ^*, also known as the Hopf-bifurcation point or the flutter point, which marks the change of stability. For $\lambda < \lambda^*$, the ensuing oscillation after an initial disturbance will eventually damp out to a steady state, establishing a static equilibrium. For $\lambda > \lambda^*$, the system will tend towards a stable limit cycle, the amplitude of which is controlled by λ. In this work, we take the LCO amplitude to be the amplitude of the vertical deflection δw at the trailing-edge tip node. Figure 4-2 shows a typical time history of such LCO behaviour.

Note that to compute the LCO amplitude at a given λ, the equations of motion (4.14) must be integrated forward in time. In the next subsection, we present the a 'generalized-α' time-marching scheme for this purpose.

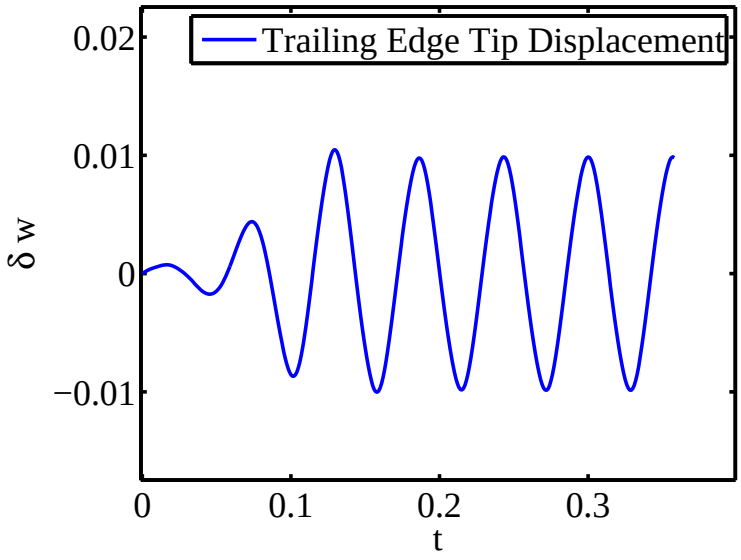

Figure 4-2: Time history of the vertical displacement of the trailing-edge tip node

4.1.2 Solution Method

To solve for the long-term dynamics of a structures problem such as (4.14), time-integration methods with numerical dissipations are typically required to eliminate the high-frequency modes so as to maintain numerical stability. To that end, a popular family of methods for structural dynamic problems is that of Newmark [60]. However, Newmark algorithms are known to be too dissipative for low-frequency modes and therefore only first-order accurate. In this work, we use instead the second-order accurate, unconditionally stable generalized-α method formulated by Chung and Hulbert in [27]. Let $\boldsymbol{u}_n$, $\dot{\boldsymbol{u}}_n$ and $\ddot{\boldsymbol{u}}_n$ denote the generalized displacement, velocity and acceleration vectors at time level n respectively. Between the time levels n and $n+1$, the equations of motion can be expressed at the 'generalized mid-point' $n+1-\alpha_m$ as follows:

$$\boldsymbol{M}\ddot{\boldsymbol{u}}_{n+1-\alpha_m} + (\boldsymbol{C}_s + \boldsymbol{C}_{\boldsymbol{aero}})\dot{\boldsymbol{u}}_{n+1-\alpha_m} + \boldsymbol{K}_{\boldsymbol{aero}}\boldsymbol{u}_{n+1-\alpha_m} + \boldsymbol{f}_\alpha + \boldsymbol{f}_{n+1-\alpha_m}(\boldsymbol{u}_{n+1-\alpha_m}) = \boldsymbol{0} \tag{4.20}$$

where the 'generalized mid-point' displacement ($\boldsymbol{u}_{n+1-\alpha_f}$), velocity ($\dot{\boldsymbol{u}}_{n+1-\alpha_f}$), acceleration ($\ddot{\boldsymbol{u}}_{n+1-\alpha_m}$) and nonlinear internal forces ($\boldsymbol{f}_{n+1-\alpha_f}(\boldsymbol{u}_{n+1-\alpha_m})$) are:

$$\begin{aligned}
\boldsymbol{u}_{n+1-\alpha_f} &= (1-\alpha_f)\boldsymbol{u}_{n+1} + \alpha_f \boldsymbol{u}_n && (4.21)\\
\dot{\boldsymbol{u}}_{n+1-\alpha_f} &= (1-\alpha_f)\dot{\boldsymbol{u}}_{n+1} + \alpha_f \dot{\boldsymbol{u}}_n && (4.22)\\
\ddot{\boldsymbol{u}}_{n+1-\alpha_m} &= (1-\alpha_m)\ddot{\boldsymbol{u}}_{n+1} + \alpha_m \ddot{\boldsymbol{u}}_n && (4.23)\\
\boldsymbol{f}_{n+1-\alpha_f}(\boldsymbol{u}_{n+1-\alpha_m}) &= (1-\alpha_f)\boldsymbol{f}(\boldsymbol{u}_{n+1}) + \alpha_f \boldsymbol{f}(\boldsymbol{u}_n) && (4.24)
\end{aligned}$$

Expressing the displacement $\dot{\boldsymbol{u}}_{n+1}$ and velocity $\ddot{\boldsymbol{u}}_{n+1}$ as functions of a single unknown $\boldsymbol{u}_{n+1}$ via the Newmark approximations [60]:

$$\begin{aligned}
\dot{\boldsymbol{u}}_{n+1} &= \frac{\gamma}{\beta\Delta t}(\boldsymbol{u}_{n+1} - \boldsymbol{u}_n) - \frac{\gamma-\beta}{\beta}\dot{\boldsymbol{u}}_n - \frac{\gamma-2\beta}{2\beta}\Delta t\ddot{\boldsymbol{u}}_n && (4.25)\\
\ddot{\boldsymbol{u}}_{n+1} &= \frac{1}{\beta\Delta t^2}(\boldsymbol{u}_{n+1} - \boldsymbol{u}_n) - \frac{1}{\beta\Delta t}\dot{\boldsymbol{u}}_n - \frac{1-2\beta}{2\beta}\ddot{\boldsymbol{u}}_n && (4.26)
\end{aligned}$$

Substituting (4.25) and (4.26) into (4.22) and (4.23), the generalized mid-point velocity and acceleration can be expressed in terms of the values at time-level n and $n+1$:

$$\dot{\boldsymbol{u}}_{n+1-\alpha_m} = \frac{(1-\alpha_f)\gamma}{\beta\Delta t}(\boldsymbol{u}_{n+1}-\boldsymbol{u}_n) - \frac{(1-\alpha_f)\gamma-\beta}{\beta}\dot{\boldsymbol{u}}_n - \frac{(1-\alpha_f)(\gamma-2\beta)}{2\beta}\Delta t\ddot{\boldsymbol{u}}_n \quad (4.27)$$

$$\ddot{\boldsymbol{u}}_{n+1-\alpha_m} = \frac{1-\alpha_m}{\beta\Delta t^2}(\boldsymbol{u}_{n+1}-\boldsymbol{u}_n) - \frac{(1-\alpha_m)}{\beta\Delta t}\ddot{\boldsymbol{u}}_n - \frac{1-\alpha_m-2\beta}{2\beta}\ddot{\boldsymbol{u}}_n \quad (4.28)$$

where α_m, α_f, β and γ are algorithmic damping parameters, which can be derived in terms of the spectral radius ρ of the amplification matrix arising from stability analysis of the algorithm as follows:

$$\alpha_m = \frac{2\rho-1}{\rho+1} \quad (4.29)$$

$$\alpha_f = \frac{\rho}{\rho+1} \quad (4.30)$$

$$\beta = \frac{1}{4}(1-\alpha_m+\alpha_f)^2 \quad (4.31)$$

$$\gamma = \frac{1}{2}-\alpha_m+\alpha_f \quad (4.32)$$

It has been shown in [27] that α_m, α_f, β and γ which satisfy the above relations produce optimal algorithmic damping with low dissipation on low-frequency modes and high dissiplation on high-frequency modes. In this work, $\rho = 0.2$ is used. The generalized-α method thus constructed is second-order accurate and unconditionally stable. For detailed analysis of this method and the derivations of these relations, the readers are referred to [27]. Substituting (4.27), (4.28), (4.21) and (4.24) into the governing equation (4.20), the equation of the residual which is nonlinear in the unknown displacement $\boldsymbol{u}_{n+1}$ is obtained:

$$\boldsymbol{R}(\boldsymbol{u}_{n+1}) = \boldsymbol{A}\boldsymbol{u}_{n+1} + (1-\alpha_f)\boldsymbol{f}(\boldsymbol{u}_{n+1}) + \boldsymbol{Q}(\boldsymbol{u}_n) = \boldsymbol{0} \quad (4.33)$$

where

$$\boldsymbol{A} = \frac{1-\alpha_m}{\beta\Delta t^2}\boldsymbol{M} + \frac{(1-\alpha_f)\gamma}{\beta\Delta t}(\boldsymbol{C}_s + \boldsymbol{C_{aero}}) + (1-\alpha_f)\boldsymbol{K_{aero}} \tag{4.34}$$

$$\begin{aligned}\boldsymbol{Q}(\boldsymbol{u}_n) &= (1-\alpha_m)\boldsymbol{M}\left[\frac{1}{\beta\Delta t^2}(-\boldsymbol{u}_n - \Delta t\dot{\boldsymbol{u}}_n) - \frac{1-2\beta}{2\beta}\ddot{\boldsymbol{u}}_n\right] + \alpha_m\boldsymbol{M}\ddot{\boldsymbol{u}}_n \\ &\quad +(1-\alpha_f)(\boldsymbol{C}_s + \boldsymbol{C_{aero}})\left[\frac{-\gamma}{\beta\Delta t}\boldsymbol{u}_n - \frac{\gamma-\beta}{\beta}\dot{\boldsymbol{u}}_n - \frac{\gamma-2\beta}{2\beta}\Delta t\ddot{\boldsymbol{u}}_n\right] \\ &\quad +\alpha_f(\boldsymbol{C}_s + \boldsymbol{C_{aero}})\dot{\boldsymbol{u}}_n + \alpha_f\boldsymbol{K_{aero}}\boldsymbol{u}_n + \alpha_f\boldsymbol{f}(\boldsymbol{u}_n) + \boldsymbol{f}_\alpha\end{aligned} \tag{4.35}$$

Note that $\boldsymbol{Q}$ is a function of $\boldsymbol{u}_n$ only and is therefore a constant matrix at time-level $n+1$. $\boldsymbol{A}$ is a constant matrix throughout the simulation. The nonlinearity in the residual is due to the internal force $\boldsymbol{f}(\boldsymbol{u}_{n+1})$. At time-level $n+1$, to solve the nonlinear residual for the unknown displacement $\boldsymbol{u}_{n+1}$, we use Newton's method. The Jacobian of the residual must then be computed:

$$\boldsymbol{J}(\boldsymbol{u}) = \frac{\partial\boldsymbol{R}(\boldsymbol{u})}{\partial\boldsymbol{u}} = \boldsymbol{A} + (1-\alpha_f)\boldsymbol{J}^{\boldsymbol{f}}(\boldsymbol{u}) \tag{4.36}$$

where

$$\boldsymbol{J}^{\boldsymbol{f}}(\boldsymbol{u}) = \frac{\partial\boldsymbol{f}(\boldsymbol{u})}{\partial\boldsymbol{u}} \tag{4.37}$$

and $\boldsymbol{J}^{\boldsymbol{f}}$ is the Jacobian of the nonlinear force, also known as the tangent stiffness matrix in computational mechanics. Knowing the displacement at time level n, one can solve (4.33) iteratively for $\boldsymbol{u}_{n+1}$ using Newton's method as follows:

$$\boldsymbol{J}(\boldsymbol{u}^p_{n+1})(\boldsymbol{u}^{p+1}_{n+1} - \boldsymbol{u}^p_{n+1}) = -\boldsymbol{R}(\boldsymbol{u}^p_{n+1}) \tag{4.38}$$

where p denotes the number of sub-iterations. At $p=0$, an initial guess for $\boldsymbol{u}^{p=0}_{n+1}$ is required. In this work, we use the solution at the previous time step such that $\boldsymbol{u}^{p=0}_{n+1} = \boldsymbol{u}_n$. Furthermore, the sub-iterations are terminated when the magnitude of the residual $\boldsymbol{R}$ has been reduced by a specific order of magnitude from its initial value, such that:

$$\frac{\|\boldsymbol{R}(\boldsymbol{u}^p_{n+1})\|_2}{\|\boldsymbol{R}(\boldsymbol{u}^{p=0}_{n+1})\|_2} \leq \epsilon \tag{4.39}$$

where ϵ is a small number between 10^{-5} to 10^{-10} depending on the desired level of convergence.

Note that at each time level, to solve the nonlinear residual equation (4.33) via Newton iterations (4.38), the nonlinear force $\boldsymbol{f}(\boldsymbol{u})$ and Jacobian $\boldsymbol{J}(\boldsymbol{u})$ must be formed multiple times. At each sub-iteration, the Jacobian matrix must also be inverted to solve for $\boldsymbol{u}_{n+1}^{p}$. For large-scale problems in which long-term dynamics must be simulated, this can be very computationally intensive. If the effects of parametric variabilities are to be studied, it becomes a computationally prohibitive task. In Section 4.2, we apply the POD-DEIM model reduction approach presented in Section 2.2 to alleviate such computational burden.

To start the time-integration, the initially undeflected plate ($\boldsymbol{u}_{n=0} = \boldsymbol{0}$) is given an updwards velocity $\dot{\boldsymbol{u}}_{n=0}$. The initial acceleration $\ddot{\boldsymbol{u}}_{n=0}$ can be computed as:

$$\ddot{\boldsymbol{u}}_{n=0} = -\boldsymbol{M}^{-1}\left[(\boldsymbol{C}_s + \boldsymbol{C}_{aero})\dot{\boldsymbol{u}}_{n=0} + \boldsymbol{K}_{aero}\boldsymbol{u}_{n=0} + \boldsymbol{f}_{\alpha} + \boldsymbol{f}(\boldsymbol{u}_{n=0})\right] \tag{4.40}$$

The solution can then be time-marched forward by solving (4.33) iteratively. The time-integration proceeds until a stable limit cycle is fully developed for the trailing-edge tip vertical displacement. To that end, a convergence criterion is imposed such that the absolute differences between the last and the second-last peaks as well as the last and third-last peaks of the displacement history (see for example, Figure 4-2) is below a certain tolerance ϵ_{LCO}. For this study, $\epsilon_{LCO} = 10^{-2}$ is used.

4.1.3 Direct Flutter Computation

The generalized-α method presented in Section 4.1.2 can be used to integrate the equations of motion forward in time to obtain time-asymptotic informations such as the LCO amplitude and equilibrium positions. Another crucial characteristic of the system that is often of interest for aeroelastic designs is the Hopf-bifurcation point or the flutter speed.

The generalized-α method can be used to bracket the flutter point within a small interval by solving the unsteady governing equations at discrete λ values. However, if the flutter point must be predicted at high accuracy, this method becomes inefficient as simulations near the true flutter point may take extremely long to converge. Therefore, to predict the flutter point, a direct method which does not involve time-integration is desired. In this section, we present a direct flutter computation method via eigen-analysis of the system based on the works of [76] and [59].

The flutter point (λ^*) or Hopf-bifurcation point is a point above which the aeroelastic system loses stability to infinitesimal disturbances, resulting in time-dependent responses such as LCO instead of settling back to an equilibrium position. Mathematically, such 'exchange of stability' which occurs when λ is increased beyond the flutter point, is due to a pair of complex conjugate eigenvalues of the system (4.14) crossing the imaginary axis of the complex plane. That is, at the flutter point, a single pair of complex eigenvalues becomes purely imaginary while all other eigenvalues of the system have negative real parts. In particular, define $\gamma(\lambda)$ such that it is the real component of the eigenvalue with the largest real part:

$$\gamma(\lambda) = max(Re(\beta_j)) \tag{4.41}$$

where β_j is the j-th eigenvalue of the system. The task of predicting λ^* is then equivalent to solving for $\gamma(\lambda^*) = 0$ such that the eigenvalue associated with the least stable eigenmode has a vanishing real part. To that end, Newton's method can be

used to solve for λ^* iteratively:

$$\frac{\partial \gamma(\lambda^n)}{\partial \lambda}(\Delta^{n+1}\lambda) = -\gamma(\lambda^n) \tag{4.42}$$

where $\Delta^{n+1}\lambda = \lambda^{n+1} - \lambda^n$ and λ^n is the non-dimensional dynamic pressure at the n-th step. To improve convergence, a relaxation parameter $\omega_{hopf} = 0.8$ is used in the Newton update:

$$\lambda^{n+1} = \lambda^n + \omega_{hopf}\Delta^{n+1}\lambda \tag{4.43}$$

To examine the stability of the aeroelastic system at a given λ value and compute the associated eignvalues, the equations of motion (4.14) are re-written in the first-order form as follows:

$$\begin{bmatrix} \boldsymbol{I}_{N\times N} & \boldsymbol{0} \\ \boldsymbol{0} & \boldsymbol{M} \end{bmatrix} \begin{bmatrix} \dot{\boldsymbol{u}} \\ \ddot{\boldsymbol{u}} \end{bmatrix} + \begin{bmatrix} \boldsymbol{0} & -\boldsymbol{I}_{N\times N} \\ \lambda\tilde{\boldsymbol{K}}_{aero} & \boldsymbol{C}_s + \sqrt{\lambda}\tilde{\boldsymbol{C}}_{aero} \end{bmatrix} \begin{bmatrix} \boldsymbol{u} \\ \dot{\boldsymbol{u}} \end{bmatrix} + \begin{bmatrix} \boldsymbol{0} \\ \boldsymbol{f}(\boldsymbol{u}) \end{bmatrix} + \begin{bmatrix} \boldsymbol{0} \\ \boldsymbol{f}_\alpha \end{bmatrix} = \boldsymbol{0} \tag{4.44}$$

where $\boldsymbol{I}_{N\times N}$ is the $N \times N$ identity matrix and λ is factored out of the aerodynamic stiffness and damping matrices such that $\boldsymbol{K}_{aero} = \lambda\tilde{\boldsymbol{K}}_{aero}$ and $\boldsymbol{C}_{aero} = \sqrt{\lambda}\tilde{\boldsymbol{C}}_{aero}$. Furthermore, define:

$$\boldsymbol{q} = \begin{bmatrix} \boldsymbol{q}_1 \\ \boldsymbol{q}_2 \end{bmatrix} = \begin{bmatrix} \boldsymbol{u} \\ \dot{\boldsymbol{u}} \end{bmatrix} \tag{4.45}$$

The first-order equations of motion (4.44) can then be expressed as follows:

$$\boldsymbol{A}\dot{\boldsymbol{q}} = \boldsymbol{B}\boldsymbol{q} + \boldsymbol{f}(\boldsymbol{q}) \tag{4.46}$$

where

$$\boldsymbol{A} = \begin{bmatrix} \boldsymbol{I}_{N\times N} & \boldsymbol{0} \\ \boldsymbol{0} & \boldsymbol{M} \end{bmatrix}, \quad \boldsymbol{B} = \begin{bmatrix} \boldsymbol{0} & \boldsymbol{I}_{N\times N} \\ -\lambda\tilde{\boldsymbol{K}}_{aero} & -(\boldsymbol{C}_s + \sqrt{\lambda}\tilde{\boldsymbol{C}}_{aero}) \end{bmatrix}, \quad \boldsymbol{f}(\boldsymbol{q}) = \begin{bmatrix} \boldsymbol{0} \\ -\boldsymbol{f}_\alpha - \boldsymbol{f}(\boldsymbol{u}) \end{bmatrix} \tag{4.47}$$

The generalized eigenvalue problem associated with this system is:

$$\tilde{\boldsymbol{B}}\boldsymbol{P}_j = \beta_j \boldsymbol{A}\boldsymbol{P}_j \tag{4.48}$$

where

$$\tilde{\boldsymbol{B}} = \begin{bmatrix} \boldsymbol{0} & \boldsymbol{I}_{N\times N} \\ -\lambda\tilde{\boldsymbol{K}}_{aero} & -(\boldsymbol{C}_s + \sqrt{\lambda}\tilde{\boldsymbol{C}}_{aero}) \end{bmatrix} + \begin{bmatrix} \boldsymbol{0} & \boldsymbol{0} \\ -\boldsymbol{J}^{\boldsymbol{f}}(\boldsymbol{u}_{eq}) & \boldsymbol{0} \end{bmatrix} \tag{4.49}$$

and $\boldsymbol{P}_j$ is the right eigenvector corresponding to the j-th eigenvalue β_j and $\boldsymbol{J}^{\boldsymbol{f}}(\boldsymbol{u}_{eq})$ is the Jacobian of the nonlinear force (as defined in (4.37)) evaluated at the equilibrium solution $\boldsymbol{u}_{eq}$. Take the derivative with respect to λ on both sides and multiply by the left eigenvector $\boldsymbol{Q}_j$ associated with the j-th eigenvalue β_j:

$$\boldsymbol{Q}_j^T \frac{\partial \tilde{\boldsymbol{B}}}{\partial \lambda} \boldsymbol{P}_j = \frac{\partial \beta_j}{\partial \lambda} \boldsymbol{Q}_j^T \boldsymbol{A} \boldsymbol{P}_j \tag{4.50}$$

The derivative of the j-th eigenvalue with respect to λ can be expressed as:

$$\frac{\partial \beta_j}{\partial \lambda} = \frac{\boldsymbol{Q}_j^T \frac{\partial \tilde{\boldsymbol{B}}}{\partial \lambda} \boldsymbol{P}_j}{\boldsymbol{Q}_j^T \boldsymbol{A} \boldsymbol{P}_j} \tag{4.51}$$

where the term $\frac{\partial \tilde{\boldsymbol{B}}}{\partial \lambda}$ can be derived analytically:

$$\frac{\partial \tilde{\boldsymbol{B}}}{\partial \lambda} = \begin{bmatrix} \boldsymbol{0} & \boldsymbol{0} \\ -\tilde{\boldsymbol{K}}_{aero} & -\frac{\tilde{\boldsymbol{C}}_{aero}}{2\sqrt{\lambda}} \end{bmatrix} \tag{4.52}$$

Let the eigenvalues β_j be arranged in the order of descending magnitude of their real parts such that $Re(\beta_1) > \ldots > Re(\beta_{2N})$. The gradient term in (4.42) is simply:

$$\frac{\partial \gamma(\lambda^n)}{\partial \lambda} = Re\left(\frac{\partial \beta_{j=1}(\lambda^n)}{\partial \lambda}\right) \tag{4.53}$$

Equations (4.42), (4.43), (4.48) and (4.53) can then be used in tandem to solve for the flutter point λ^*. Specifically, starting from an initial guess $\lambda^{n=0}$, the generalized eigenvalue problem of the system (4.48) is solved for $\beta_{j=1}$, $\boldsymbol{P}_{j=1}$ and $\boldsymbol{Q}_{j=1}$ with which the gradient term of (4.42) can be evaluated via (4.53). The Newton update (4.43) is then computed and the process repeated until λ converges to a certain prescribed tolerance ϵ_{fp} such that $|\Delta^{n+1}\lambda| < \epsilon_{fp}$. Note that as $\lambda^n \to \lambda^{n+1}$ in Newton iterations (4.42), the equilibrium position ($\boldsymbol{u}_{eq}$) is non-trivial for plates at non-zero angles of

attack ($\alpha_o \neq 0$), and varies from one iteration to another. Therefore for each λ, a new equilibrium position must be established in order to update the tangent stiffness matrix $\boldsymbol{J^f}$ in (4.49). To that end, the following nonlinear equilibrium equations must also be solved iteratively at each step n using Newton's method for $\boldsymbol{u}_{eq}$:

$$\lambda^n \tilde{\boldsymbol{K}}_{aero}\boldsymbol{u} + \boldsymbol{f}_\alpha + \boldsymbol{f}(\boldsymbol{u}) = \boldsymbol{0} \tag{4.54}$$

with the corresponding Jacobian:

$$\boldsymbol{J}(\boldsymbol{u}) = \lambda^n \tilde{\boldsymbol{K}}_{aero} + \boldsymbol{J^f}(\boldsymbol{u}), \quad \boldsymbol{J^f} = \frac{\partial \boldsymbol{f}(\boldsymbol{u})}{\partial \boldsymbol{u}} \tag{4.55}$$

The solution of (4.54) involves multiple evaluations and inversions of the $2N \times 2N$ nonlinear Jacobian in the same manner as the inner iterations of generalized-α method presented in Section 4.1.2. This process and the solution of the generalized eigenvalue problem (4.48) can both be computationally intensive for large-scale problems.

4.2 POD-DEIM Reduced Order Model

As discussed in Section 4.1.2, to time-integrate the equation of motion (4.14) using the implicit generalized-α algorithm, the resultant nonlinear system of equations at each time step must be solved iteratively by Newton's method. For large-scale systems, this is typically a computationally intensive task and therefore precludes any multi-query tasks such as uncertainty quantifications and optimizations.

To alleviate the computational burden, we apply the POD-DEIM methodology described in Chapter 2 to construct a reduced-order model (ROM) from from the system (4.14), the full-order model (FOM).

This model problem possesses the three challenging features discussed in Section 1.3. Firstly, the nonlinear term has a noncomponentwise dependence on the state. In particular, each grid point is surrounded by 6 triangular elements. The 6 DOFs of the nonlinear force at a particular node are computed not only using the 6 generalized displacements at the same node but also using the 36 generalized displacements at the 6 adjacent nodes. In addtion, the 6 DOFs in the nonlinear force $\boldsymbol{f}(\boldsymbol{u})$ have vastly different orders of magnitude in both the initial transient and the quasi-steady regions of the simulation as shown on Figure 4-3(a) . Note that DOF 3, which represents the dominant out-of-plane bending response is at least 6 orders of magnitude larger than the DOF 6, the moment about the z-axis. Furthermore, the singular values corresponding to each DOF do not decay in the same manner. This is illustrated by Figure 4-4, in terms of the 'omitted energy' in (2.17). The dashed line shows that to achieve the same level of accuracy across all 6 DOFs, different numbers of POD modes must be used for the DOFs of the nonlinear term. On the other hand, the difference in the magnitudes of the state DOFs are much more moderate as shown on Figure 4-3(b).

In Section 2.2, two modifications to the existing POD-DEIM methodology are developed to address the abovementioned challenges. Firstly, to construct the ROM, we use vector-valued state POD modes and scalar-valued ones for the nonlinear force; that is, a single, 'globalized' set of modes is used for $\boldsymbol{u}$ while the one set of scalar-

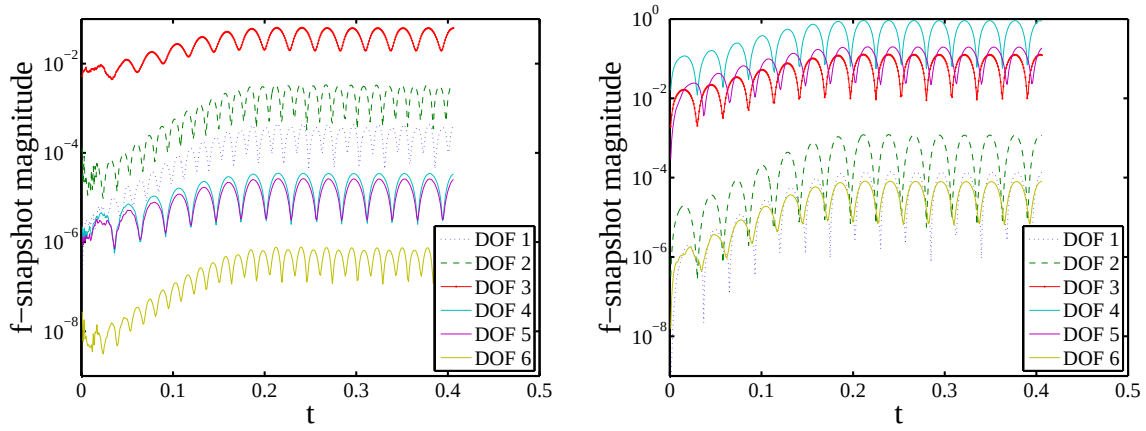

(a) Nonlinear Term (b) State

Figure 4-3: Evolution of the magnitudes of different DOFs of the nonlinear term and state over time

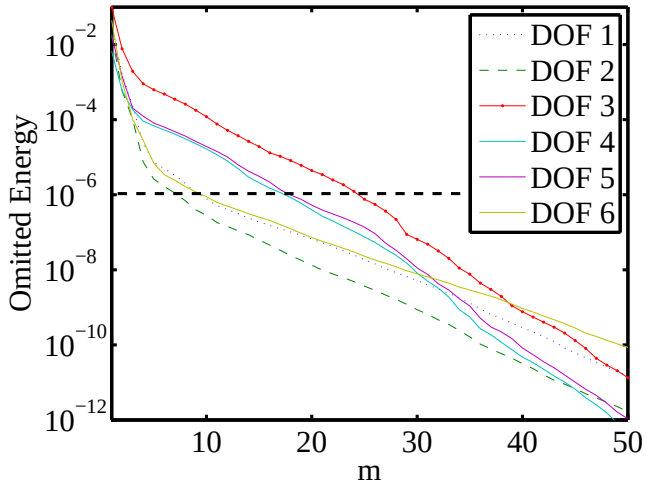

Figure 4-4: Omitted energy in each DOF of the nonlinear term as a function of the number of POD modes

valued POD modes is used for each of the 6 DOFs of $\boldsymbol{f}$.

As outlined in Chapter 2, we first approximate the state solution as a linear combination of state POD basis vectors:

$$\mathbf{u} \approx \mathbf{\Phi} \mathbf{u}_r \tag{4.56}$$

where

$$\boldsymbol{\Phi} = [\boldsymbol{\phi}_1, \boldsymbol{\phi}_2, \ldots, \boldsymbol{\phi}_K] \in \mathbb{R}^{N\times K}, \quad \mathbf{u}_r = [\tilde{u}_1, \tilde{u}_2, \ldots, \tilde{u}_K] \in \mathbb{R}^{K\times 1} \tag{4.57}$$

Substituting the expansion into the FOM (4.14) and project it onto the reduced space using the POD-Galerkin procedure outlined in Section 2.1.1:

$$\boldsymbol{M}_r\ddot{\boldsymbol{u}}_r + \boldsymbol{C}_r\dot{\boldsymbol{u}}_r + \boldsymbol{K}_r^{aero}\boldsymbol{u}_r + \boldsymbol{f}_r^{\alpha} + \boldsymbol{f}_r(\boldsymbol{\Phi}\boldsymbol{u}_r) = \mathbf{0} \tag{4.58}$$

where

$$\begin{aligned}
\boldsymbol{M}_r &= \boldsymbol{\Phi}^T\boldsymbol{M}\boldsymbol{\Phi} \in \mathbb{R}^{K\times K} && (4.59)\\
\boldsymbol{C}_r &= \boldsymbol{\Phi}^T(\boldsymbol{C}_s + \boldsymbol{C}_{aero})\boldsymbol{\Phi} \in \mathbb{R}^{K\times K} && (4.60)\\
\boldsymbol{K}_r^{aero} &= \boldsymbol{\Phi}^T\boldsymbol{K}_{aero}\boldsymbol{\Phi} \in \mathbb{R}^{K\times K} && (4.61)\\
\boldsymbol{f}_r^{\alpha} &= \boldsymbol{\Phi}^T\boldsymbol{f}_{\alpha} \in \mathbb{R}^{K\times 1} && (4.62)\\
\boldsymbol{f}_r(\boldsymbol{u}_r) &= \boldsymbol{\Phi}^T\boldsymbol{f}(\boldsymbol{\Phi}\boldsymbol{u}_r) \in \mathbb{R}^{K\times 1} && (4.63)
\end{aligned}$$

The inefficiencies of the POD-Galerkin ROM due to the online computation of the reduced nonlinear term (4.63) and its Jacobian have been discussed in detail in Section 2.1.1. To recover the ROM efficiency, we apply the DEIM approximation to the nonlinear force term. Furthermore, we employ the two modifications to the POD-DEIM methodology presented in Section 2.2; that is, we use scalar-valued POD modes as well as DEIM over-sampling for the nonlinear term. The resultant 'modified POD-DEIM' ROM is as follows:

$$\boldsymbol{M}_r\ddot{\boldsymbol{u}}_r + \boldsymbol{C}_r\dot{\boldsymbol{u}}_r + \boldsymbol{K}_r^{aero}\boldsymbol{u}_r + \boldsymbol{f}_r^{\alpha} + \hat{\mathbf{B}}_r\mathbf{f}_{\hat{\mathbf{z}}}(\boldsymbol{\Phi}_{(\hat{\mathbf{z}}')_g}\mathbf{u}_r) = \mathbf{0} \tag{4.64}$$

where

$$\begin{aligned}
\hat{\mathbf{B}}_r &= \boldsymbol{\Phi}^T diag\{\boldsymbol{\Psi}^1(\boldsymbol{\Psi}^1_{\hat{\mathbf{z}}})^+, \boldsymbol{\Psi}^2(\boldsymbol{\Psi}^2_{\hat{\mathbf{z}}})^+, \ldots, \boldsymbol{\Psi}^{N_v}(\boldsymbol{\Psi}^{N_v}_{\hat{\mathbf{z}}})^+\} \in \mathbb{R}^{K\times N_v\hat{M}} && (4.65)\\
\mathbf{f}_{\hat{\mathbf{z}}} &= [\mathbf{f}^1_{\hat{\mathbf{z}}}, \mathbf{f}^2_{\hat{\mathbf{z}}}, \ldots, \mathbf{f}^{N_v}_{\hat{\mathbf{z}}}]^T \in \mathbb{R}^{N_v\hat{M}\times 1} && (4.66)
\end{aligned}$$

and $N_v = 6$ in this problem, for the 6 DOFs of the generalized nonlinear force at each grid point. $\boldsymbol{\Psi}^i$ is the scalar-valued POD mode for the i-th DOF of the nonlinear force $\mathbf{f}^i$. $\mathbf{f}^i_{\hat{\mathbf{z}}}$ and $\boldsymbol{\Psi}^i_{\hat{\mathbf{z}}}$ contain the corresponding $\hat{M}$ rows of $\mathbf{f}^i$ and $\boldsymbol{\Psi}^i$ specified by the interpolation indices $\hat{\mathbf{z}} \in \mathbb{R}^{\hat{M}\times 1}$. $(\hat{\mathbf{z}}')_g$ contains the $\hat{M}'$ global indices of the all the state variables that must be reconstructed online as determined from $\hat{\mathbf{z}}$ based on nodal connectivity. This reduced system of equations can now be integrated forward in time using the implicit generalized-α method outlined in Section 4.1.2. The resultant nonlinear residual equation that must be solved at each time step for $\boldsymbol{u}_r^{n+1}$ is:

$$\underbrace{\boldsymbol{R}_r(\boldsymbol{u}_r^{n+1})}_{K\times K} = \boldsymbol{A}_r\boldsymbol{u}_r^{n+1} + (1-\alpha_f)\hat{\mathbf{B}}_r \underbrace{\mathbf{f}_{\hat{\mathbf{z}}}(\underbrace{\boldsymbol{\Phi}_{(\hat{\mathbf{z}}')_g}}_{\hat{M}'\times K}\mathbf{u}_r^{n+1})}_{6\hat{M}\times 1} + \boldsymbol{Q}(\boldsymbol{u}_r^n) = \mathbf{0} \tag{4.67}$$

where

$$\begin{aligned}
\boldsymbol{A}_r &= \frac{1-\alpha_m}{\beta\Delta t^2}\boldsymbol{M}_r + \frac{(1-\alpha_f)\gamma}{\beta\Delta t}\boldsymbol{C}_r + (1-\alpha_f)\boldsymbol{K}_r^{aero} && (4.68)\\
\boldsymbol{Q}(\boldsymbol{u}_r^n) &= (1-\alpha_m)\boldsymbol{M}_r\left[\frac{1}{\beta\Delta t^2}(-\boldsymbol{u}_r^n - \Delta t\dot{\boldsymbol{u}}_r^n) - \frac{1-2\beta}{2\beta}\ddot{\boldsymbol{u}}_r^n\right] + \alpha_m\boldsymbol{M}_r\ddot{\boldsymbol{u}}_r^n \\
&\quad +(1-\alpha_f)\boldsymbol{C}_r\left[\frac{-\gamma}{\beta\Delta t}\boldsymbol{u}_r^n - \frac{\gamma-\beta}{\beta}\dot{\boldsymbol{u}}_r^n - \frac{\gamma-2\beta}{2\beta}\Delta t\ddot{\boldsymbol{u}}_r^n\right] \\
&\quad +\alpha_f\boldsymbol{C}_r\dot{\boldsymbol{u}}_r^n + \alpha_f\boldsymbol{K}_r^{aero}\boldsymbol{u}_r^n + \alpha_f\boldsymbol{f}_r(\boldsymbol{u}_r^n) + \boldsymbol{f}_r^{\alpha} && (4.69)
\end{aligned}$$

The reduced system of nonlinear residual equation can be solved using Newton's method:

$$\boldsymbol{J}_r(\boldsymbol{u}_r^{n+1}\big|_p)(\boldsymbol{u}_r^{n+1}\big|_{p+1} - \boldsymbol{u}_r^{n+1}\big|_p) = -\boldsymbol{R}_r(\boldsymbol{u}_r^{n+1}\big|_p) \tag{4.70}$$

where the reduced Jacobian of the residual is:

$$\boldsymbol{J}_r(\boldsymbol{u}_r^{n+1}\big|_p) = \boldsymbol{A}_r + (1-\alpha_f)\hat{\mathbf{B}}_r \underbrace{\mathbf{J}^{\mathbf{f}}_{\hat{\mathbf{z}},(\hat{\mathbf{z}}')_g}(\boldsymbol{\Phi}_{(\hat{\mathbf{z}}')_g}\,\boldsymbol{u}_r^{n+1}\big|_p)}_{6\hat{M}\times\hat{M}'}\boldsymbol{\Phi}_{(\hat{\mathbf{z}}')_g} \tag{4.71}$$

Note that systems (4.67) and (4.71) are simply reduced formulations of (4.33) and (4.36) respectively. However, as will be shown by numerical results for various test

cases in Section 4.3, such formulations result in substantial computational savings over the FOM. This is largely due to the fact that $\hat{M} \ll N$ which means only a small fraction of the triangular elements in the computational domain needs to be reconstructed online for the necessary rows of $\mathbf{f}_{\hat{\mathbf{z}}}$ and $\mathbf{J}^{\mathbf{f}}{}_{\hat{\mathbf{z}},(\hat{\mathbf{z}}')_g}$. Also, as $K \ll N$, the inversion of $\boldsymbol{J}_r$ in each Newton iteration can be performed much more rapidly than its FOM counterpart.

Finally, to efficiently monitor the convergence towards a stable limit cycle, the time history of the vertical displacement in the trailing edge tip node is computed on-the-fly via an inexpensive partial state reconstruction $\mathbf{u}_{z^*} = \boldsymbol{\Phi}_{z^*}\mathbf{u}_r$, where z^* is the index corresponding to the desired state DOF.

The POD-DEIM model reduction methodology can also be applied to the equations that need to be solved in the direct flutter point computation presented in Section 4.1.3. In particular, the reduced-order version of the generalized eigenvalue problem (4.48) of the aeroelastic system is

$$\tilde{\boldsymbol{B}}_r \boldsymbol{P}_r^j = \beta_r^j \boldsymbol{A}_r \boldsymbol{P}_r^j \tag{4.72}$$

where

$$\boldsymbol{A}_r = \begin{bmatrix} \boldsymbol{I}_{K\times K} & \mathbf{0} \\ \mathbf{0} & \boldsymbol{M}_r \end{bmatrix} \tag{4.73}$$

$$\tilde{\boldsymbol{B}}_r = \begin{bmatrix} \mathbf{0} & \boldsymbol{I}_{K\times K} \\ -\lambda\tilde{\boldsymbol{K}}_r^{aero} & -(\boldsymbol{C}_r^s + \sqrt{\lambda}\tilde{\boldsymbol{C}}_r^{aero}) \end{bmatrix} + \begin{bmatrix} \mathbf{0} & \mathbf{0} \\ -\boldsymbol{J^f}_r(\boldsymbol{u}_r^{eq}) & \mathbf{0} \end{bmatrix} \tag{4.74}$$

and $\boldsymbol{I}_{K\times K}$ is the $K \times K$ identity matrix, $\boldsymbol{P}_r^j$ is the right eigenvector corresponding to the j-th eigenvalue β_r^j of the ROM and $\boldsymbol{J^f}_r$ is the reduced Jacobian of the nonlinear force:

$$\boldsymbol{J^f}_r(\boldsymbol{u}_r^{eq}) = \hat{\mathbf{B}}_r \mathbf{J}^{\mathbf{f}}{}_{\hat{\mathbf{z}},(\hat{\mathbf{z}}')_g}(\boldsymbol{\Phi}_{(\hat{\mathbf{z}}')_g}\boldsymbol{u}_r^{eq})\boldsymbol{\Phi}_{(\hat{\mathbf{z}}')_g} \tag{4.75}$$

To obtain the equilibrium solution $\boldsymbol{u}_r^{eq}$, the reduced version of (4.54) that must be

solved for each λ^n value during the Newton iterations (4.42) is as follows:

$$\lambda^n \tilde{\boldsymbol{K}}_r^{aero} \boldsymbol{u}_r + \boldsymbol{f}_r^{\alpha} + \hat{\mathbf{B}}_r \mathbf{f}_{\hat{\mathbf{z}}}(\boldsymbol{\Phi}_{(\hat{\mathbf{z}}')_g} \mathbf{u}_r) = \mathbf{0} \tag{4.76}$$

with the corresponding reduced Jacobian:

$$\boldsymbol{J}_r(\boldsymbol{u}_r) = \lambda^n \tilde{\boldsymbol{K}}_r^{aero} + \boldsymbol{J^f}_r(\boldsymbol{u}_r) \tag{4.77}$$

4.3 Numerical Results

In this section, the modified POD-DEIM methodology is applied to perform model reduction on the aeroelastic system described in Section 4.1. A total of four numerical test cases are considered here. In the first test case, the ROM is constructed for a system with fixed parameters. The second test case considers the same system with the non-dimensional dynamic pressure λ as the sole input parameter while the plate thickness h is introduced as an additional input parameter in the third test case. Finally, the last test case considers the system with three input parameters: λ, h, and steady angle of attack α_o.

4.3.1 Problem Setup

In all cases considered in this work, the time-integration of the equations of motion is performed using the generalized-α method with a time step of 0.001s. The time-dependent aeroelastic response is initiated by prescribing an upwards velocity initial condition as described in Section 4.1.2, simulating a sudden gust encounter. For the spatial discretization of the FOM, 49 spatial grid points are used in both x and y directions, resulting in 4608 triangular finite elements and a total of $N = 14112$ unknowns.

Table 4.1 below summarizes the fluid and structural parameter values that are used in all four test cases in this section:

Parameter	Symbol	Value
chord	c	$0.3m$
semi-span	L	$0.3m$
nominal plate thickness	h_o	$0.001m$
plate density	ρ_s	$2800kg/m^3$
modulus of elasticity	E	$70GPa$
Poisson's ratio	ν	0.3
structural damping coefficient	β_s	20
mass ratio	μ	0.2
freestream Mach number	M_∞	2.0

Table 4.1: Flow and structural parameters for the aeroelastic system

The accuracy of the ROM is quantified by comparing its outputs of interest — LCO amplitude and flutter point with those of the FOM. In particular, for solutions in the LCO region as well as the direct flutter point computations, we calculate the absolute relative error as:

$$|\epsilon_{rel}| = \frac{|\ell^{ROM} - \ell^{FOM}|}{|\ell^{FOM}|} \tag{4.78}$$

where ℓ denotes an output of interest. For LCO amplitudes that are damped out to trivial solutions (cases with $\alpha_o = 0°$), absolute error is computed instead to avoid divisions by small numbers:

$$|\epsilon| = |\ell^{ROM} - \ell^{FOM}| \tag{4.79}$$

4.3.2 Fixed Parameter Case

In this section, we apply the modified POD-DEIM methodology presented in Section 4.2 to an aeroelastic simulation with fixed input parameters. The dynamic pressure parameter λ which controls the LCO amplitude is set to 90. The plate is cantilevered with zero steady angle of attack ($\alpha_o = 0$) while its thickness is held at the nominal value of $0.001m$. The goal of this exercise is not to merely reproduce the results of a single time-dependent FOM simulation, but rather to benchmark this modified POD-DEIM methodology for the simplest model reduction task and compare its performance against ROMs constructed using the orignial POD-DEIM and the POD-only[3] methodologies.

As shown on Figure 4-5, FOM solution converges to a stable limit cycle in 0.46 seconds, producing 460 snapshots for the state and nonlinear force. These snapshots are used to construct the modified POD-DEIM reduced-order model following the prodecures outlined in Section 4.2. The ROM is then evaluated at the same set of intput parameters to reproduce the FOM result. $K = 25$ vector-valued state POD modes are used, corresponding to the relative omitted energy Ω_u of 6.1×10^{-13} in the approximating the state snapshots. A tolerance of $\epsilon_f = 10^{-9}$ in relative omitted

[3]POD-only methodology: refers to the POD-Galerkin method presented in Section 2.1.1 with no special treatment for nonlinearity

energy Ω_f is imposed on all 6 scalar-valued POD modes for the nonlinear term. As a result, the nonlinear term and its Jacobian at $\hat{M} = 79$ out of a total of 2352 nodes on the computational domain must be evaluated on-line from the $\hat{M}' = 2200$ reconstructed state components (out of a total of $N = 14112$ components). Figure 4-5 shows that the time histories of the vertical displacement of the trailing-edge tip node computed using the FOM and ROM are in excellent agreement. Furthermore, the LCO amplitude is computed at a 0.24% relative error with the ROM. The speed-up of the ROM over the FOM in performing the same simulation is a factor of 40.

It is possible to trade off speed-up for higher accuracy by imposing more stringent tolerance values ϵ_f on the relative omitted energy of the POD modes for the nonlinear term, as shown on Figure 4-6. The previous result is the left-most data point on this plot with $\epsilon_f = 10^{-9}$. By decreasing the tolerance to $\epsilon_f = 10^{-11}$, marked by the right-most point on the plot, it is possible to reduce the relative error in LCO amplitude by a factor of 10 at the cost of a lower speed-up factor of 28. At this point, $\hat{M} = 114$ and $\hat{M}' = 3138$.

Note that $\boldsymbol{f}$ and $\boldsymbol{J}$ are assembled by their corresponding elemental force vectors and Jacobian matrices. To evaluate selected rows of $\boldsymbol{f}$ and $\boldsymbol{J}$ in the DEIM approximation, all triangular finite elements directly adjacent to the the required nodes on the computational domain must be evaluated. Therefore the number of elemental vector and matrices that must be evaluated online directly affects speed-up of this POD-DEIM ROM, as shown on Figure 4-6.

The advantage of the modified POD-DEIM methodology over the original POD-DEIM and POD-only methodologies is demonstrated by Figure 4-7. The existence of disparate magnitudes in different DOFs of the nonlinear term as well as its highly oscillatory nature in this problem makes the nonlinear term and its Jacobian difficult to approximate using the original DEIM methodology. As a result, a large number of interpolation points must be used – so large that almost all the components of the nonlinear term and all of the state components must be evaluated in the online process (i.e. $\hat{M} \sim N, \hat{M}' = N$). This reduces the efficiency of the original POD-DEIM methodology to that of the POD-only approach whose limitations in the presence of

nonlinearities are discussed in Section 2.1.1. Consequently, both approaches only achieve a speed-up factor of approximately 3 over the FOM. In comparison, the modified POD-DEIM methodology with $\epsilon_f = 10^{-11}$ achieves speed-up factors between 25 to 30 for all six dimensions of the ROM examined, as shown on Figure 4-7.

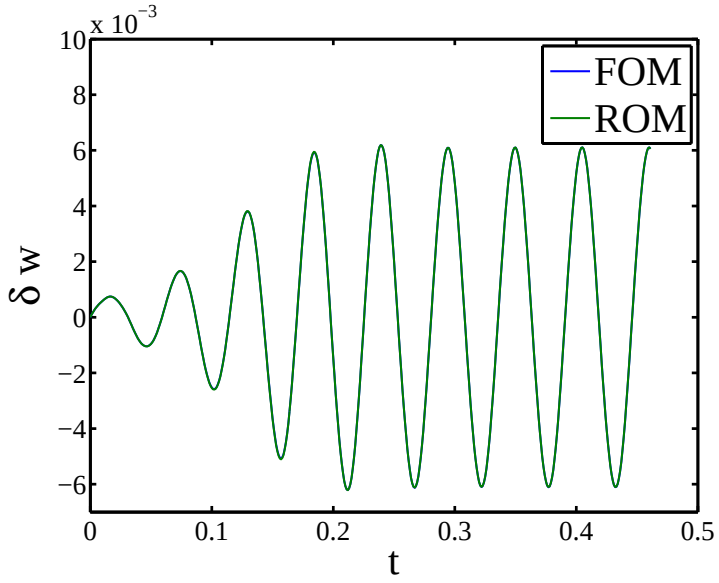

Figure 4-5: Time history of the vertical displacement of the trailing-edge tip node of the plate

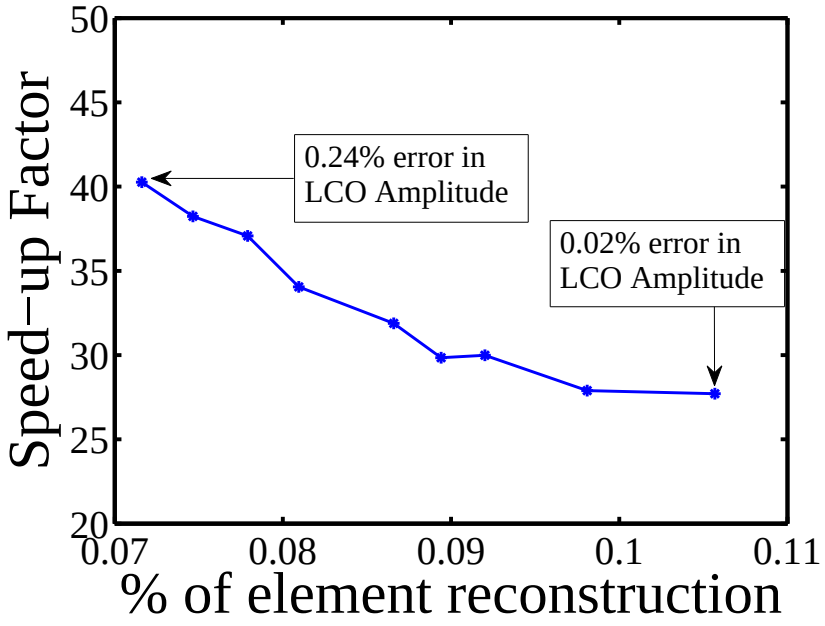

Figure 4-6: Speed-up of the modified POD-DEIM ROM over the FOM for the fixed parameter case

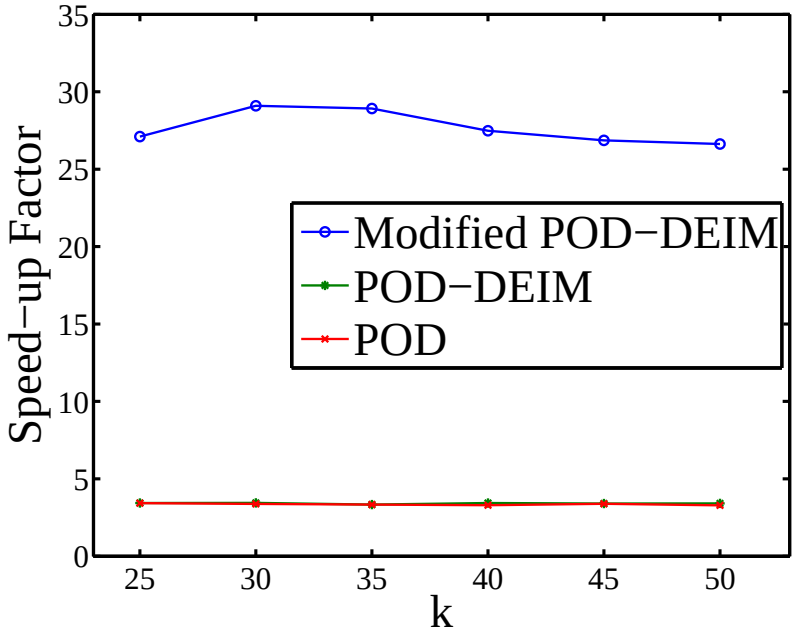

Figure 4-7: Comparison of speed-up factor between the modified POD-DEIM, original POD-DEIM and the POD-only. methodologies

4.3.3 1-Parameter Case: Variable Dynamic Pressure λ

In this section, we examine the performance of the modified POD-DEIM ROM on the same aeroelastic system with a single input parameter λ, which is allowed to vary in the interval $\lambda \in [60, 120]$. All other parameters are the same as the fixed-parameter case. It is of particular interest to assess the efficacy of the ROM at 'intermediate points' within this range of variation at which no snapshots have been collected during sampling.

As discussed before, if λ is above the flutter point λ^*, it controls the LCO amplitude. For all $\lambda < \lambda^*$, the solution will eventually damp out to a trivial equilibrium solution for $\alpha_o = 0$, after an initial transient.

The ROM is constructed with 3 sets of snapshots obtained by simulating the FOM at $\lambda = 60, 90$ and 120. For each simulation, the time-integration is performed until either the steady state solution or a stable limit cycle has been established. A tolerance on the relative omitted energy $\epsilon_u = 10^{-12}$ is imposed, resulting in the inclusion of $K = 31$ state POD modes. For the scalar-valued POD modes of the nonlinear term, $\epsilon_f = 10^{-9}$ is imposed. As a result, $\hat{M} = 96$ and $\hat{M}' = 2904$, requiring the evaluation of 9.4% of all the triangular elements in the online stage. A 'λ-sweep' is then performed to solve both FOM and ROM at λ values in the interval $[60, 120]$ at increments of $\Delta\lambda = 5$. A bifurcation diagram showing the thickness-normalized LCO amplitudes at each λ value are plotted on Figure 4-8. Excellent agreement is obtained between the FOM and ROM results. It can also be observed from the figure that a bifurcation or flutter point exists between $\lambda = 65$ and $\lambda = 70$. This flutter point is solved by the direct flutter computation using both FOM and ROM as outlined in Sections 4.1.3 and 4.2 respectively and plotted on Figure 4-8 ($\lambda^*_{FOM} = 69.02, \lambda^*_{ROM} = 69.05$). The relative errors in LCO amplitudes for $\lambda > \lambda^*$ is plotted on Figure 4-9(a). Note that for all points far away from the flutter point ($\lambda > 70$), the relative error is $O(10^{-3})$. The error is high at $\lambda = 70$ because it is very close to the Hopf bifurcation point. The convergence to a stable limit cycle at $\lambda = 70$ takes over 1500 time steps for both FOM and ROM. The accumulation of approximation error during such long-time in-

tegration process results in high ROM error. Since $\lambda = 60$ and $\lambda = 65$ correspond to damped trivial solutions, the absolute errors are computed and plotted on Figure 4-9(a) instead to avoid division by near-zero numbers. Indeed, ROM correctly predicts these damped solutions. Figure 4-9(a) also shows that between the LCO and damped solutions, the flutter point is predicted at a relative error below 10^{-3}. Finally, Figure 4-9(b) shows that the ROM in this case is a factor of 30 to 40 times faster than the FOM in computing the LCO amplitudes at various λ values.

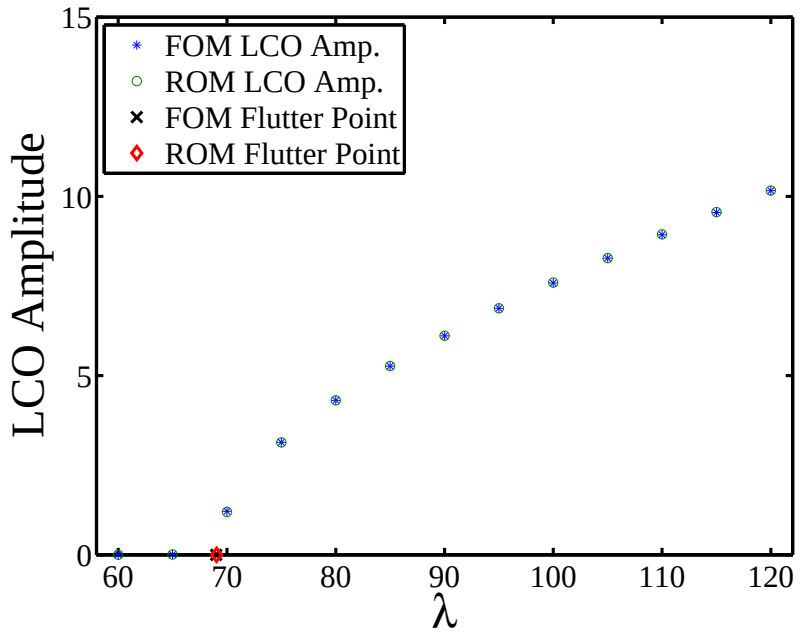

Figure 4-8: Comparison between the bifurcation diagrams with respect to the non-dimensional dynamic pressure λ, computed using the FOM and the modified POD-DEIM ROM ($K = 31$, $\hat{M} = 96$, $\hat{M}' = 2904$) via time-integrations. Also plotted are the flutter points computed using the FOM ($\times, \lambda^*_{FOM} = 69.02$) and ROM ($\diamond, \lambda^*_{ROM} = 69.05$) via the direct flutter computation

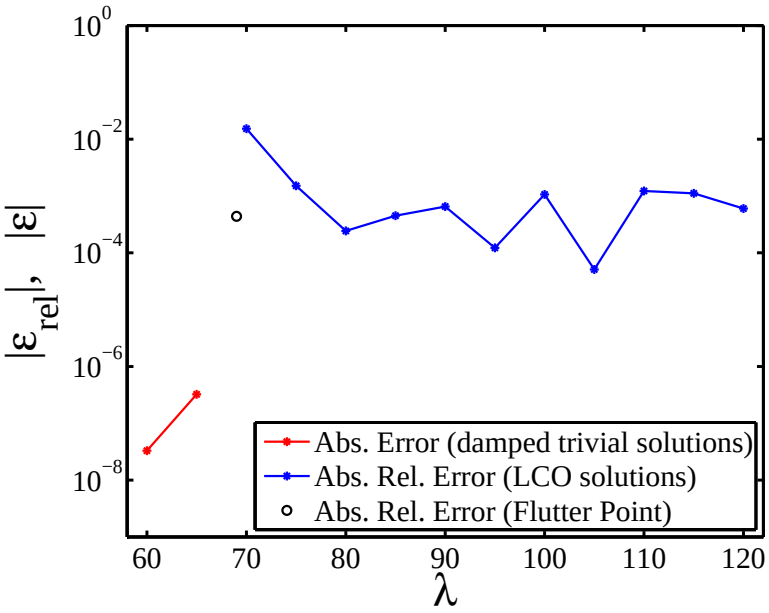

(a) Relative Error

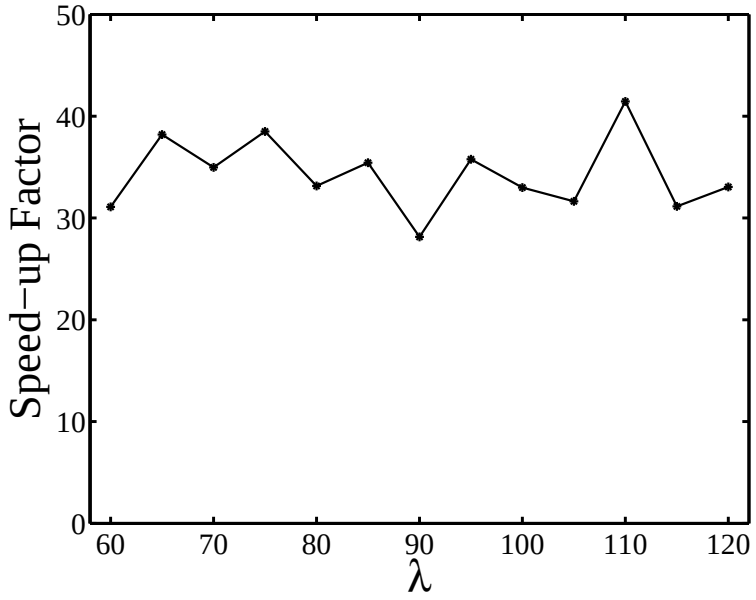

(b) Speed-up

Figure 4-9: Error and speed-up over the FOM in computing LCO amplitudes, using the modified POD-DEIM ROM with $K = 31$, $\hat{M} = 96$, and $\hat{M}' = 2904$

4.3.4 2-Parameter Case: Variable Dynamic Pressure λ and Plate Thickness h

In this section, we introduce a second input parameter — the plate thickness h and allow it to vary $\pm 15\%$ from the nominal thickness h_o. λ varies between 60 and 120 as before while all other system parameters remain the same as the fixed-parameter case. At different plate thicknesses, the flutter point λ^* shifts, forming a flutter boundary, as illustrated on the 2-D input parameter space on Figure 4-10. The tasks for the ROM in this case are to efficiently compute the bifurcation diagram with respect to λ at various h values as well as predicting the flutter boundary.

The ROM is constructed by 9 sets of unsteady solution snapshots uniformly spaced in the parameter domain, marked by the blue crosses on Figure 4-10. A tolerance on the relative omitted energy of $\epsilon_u = 10^{-13}$ is imposed, resulting in the inclusion of $K = 49$ state POD modes. For the scalar-valued POD modes of the nonlinear term, $\epsilon_f = 10^{-11}$ is imposed. As a result, $\hat{M} = 198$ and $\hat{M}' = 5544$, requiring the evaluation of 19.6% of all the triangular elements in the online stage. λ-sweeps at three thickness values: $h = 0.9h_o, 1.0h_o$ and $h = 1.1h_o$ are performed using both FOM and ROM in which they are solved at λ values in the interval $[60, 120]$ at increments of $\Delta\lambda = 5$.

For each thickness value, the thickness-normalized LCO amplitudes at each λ value are plotted on Figure 4-11. Note that for all three thickness values, the bifurcation diagrams computed using the ROM are in excellent agreement with those computed by the FOM. Errors in LCO amplitudes in the three cases are presented on Figure 4-12(a). As in the 1-parameter case, relative errors are computed for LCO solutions while the absolute errors are computed for the damped trivial solutions. Note that for the thin-plate case ($h = 0.9h_o$), all 13 points correspond to LCO solutions, since $\lambda^* < 60$ at this thickness. The relative errors for solutions far away from the flutter points are all $O(10^{-3})$, the same as the 1-parameter case. Larger errors are again observed near the flutter points of the $h = 1.0h_o$ and $h = 1.1h_o$ cases, as marked on Figure 4-12(a), due to long-time integration. Figure 4-12(b) shows that the speed-up over the FOM for all three thickness values are mostly between 13 to 20 times – half

as high as the 1-parameter case. This reduction is a result of having to integrate over twice as many triangular elements online than the 1-parameter case (9.4% vs. 19.6%).

Next, the same ROM is applied to compute flutter points at different thickness values in the range $[0.85h_o, 1.15h_o]$. The resultant flutter boundary is plotted on Figure 4-13 with the FOM results and are observed to be in excellent agreement. Figure 4-14(a) shows that the relative errors in predicting all the points on the flutter boundary are just below 10^{-4}. The speed-up over the FOM at these points are all around 130 times. The speed-up is significantly higher than all other cases considered thus far because the plate is held at zero steady angle of attack. Consequently, the equilibrium solution required at every iteration of the direct flutter computation is always a trivial one ($\boldsymbol{u}_{eq} = \mathbf{0}$) and the solutions of the nonlinear equilibrium equations (4.54) and its ROM counterpart (4.76) are not necessary. That is to say, once the ROM is constructed, the ensuing root-finding problem (4.42) solving $\gamma(\lambda^*) = 0$ is linear with respect to the state and therefore the online complexity is only a function of $K = 49 \ll N$ and not of $\hat{M}$ or $\hat{M}'$.

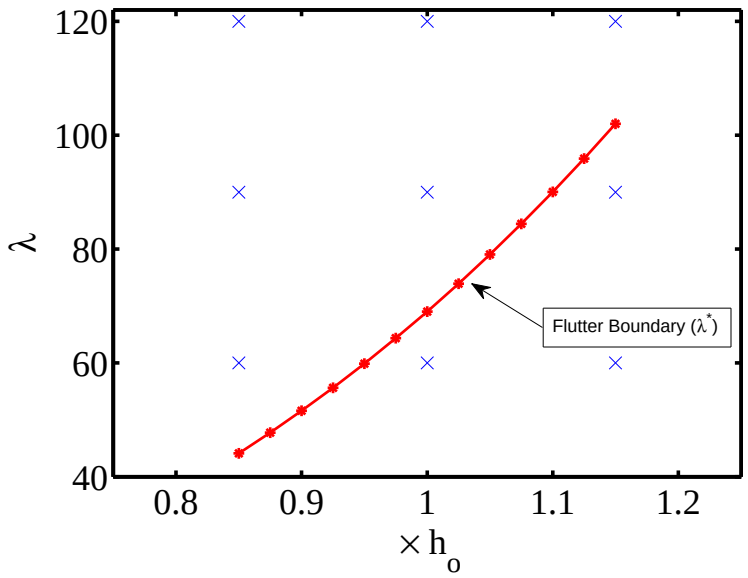

Figure 4-10: Flutter boundary in 2-D input paramter space. The locations of the 9 sets of unsteady solution samples used to generate the ROM are marked by the blue crosses

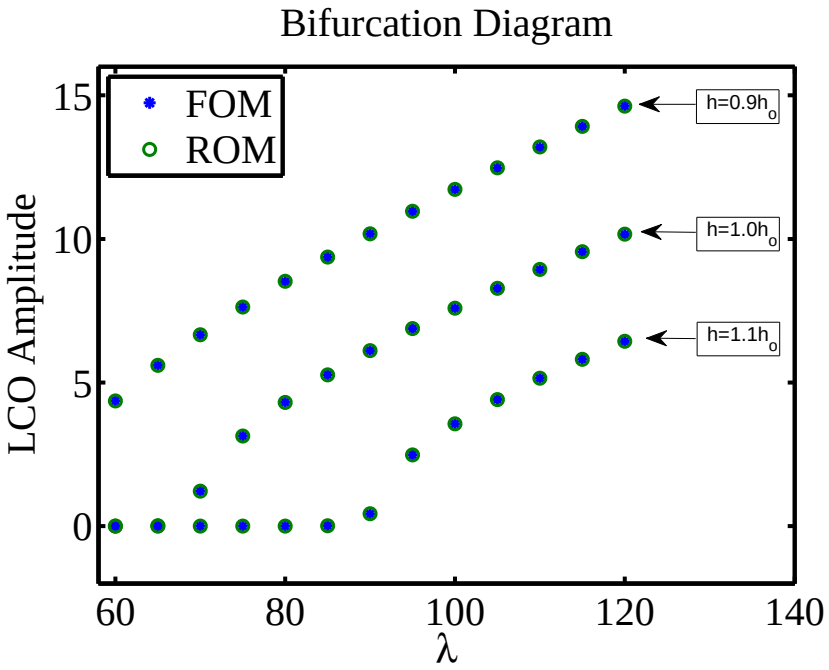

Figure 4-11: Comparison between the bifurcation diagrams with respect to λ at three thickness values: $h = 0.9h_o, 1.0h_o$ and $1.1h_o$, computed using the FOM and the modified POD-DEIM ROM ($K = 49$, $\hat{M} = 198$, $\hat{M}' = 5544$) via time-integrations.

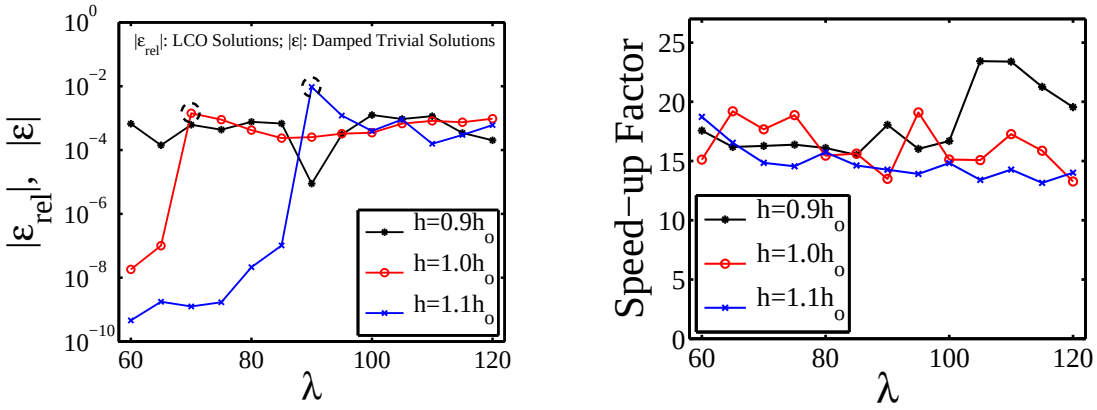

(a) Relative Error

(b) Speed-up

Figure 4-12: Relative error and speed-up over FOM in LCO amplitude at three thickness values using the modified POD-DEIM ROM ($K = 49$, $\hat{M} = 198$, $\hat{M}' = 5544$)

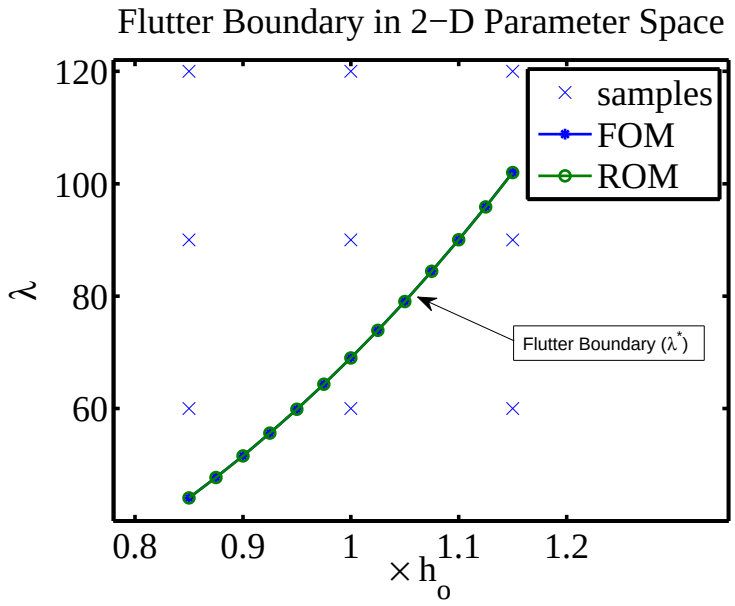

Figure 4-13: Comparison of the flutter boundaries computed by the FOM and the modified POD-DEIM ROM ($K = 49$, $\hat{M} = 198$, $\hat{M}' = 5544$) via the direct flutter computations. The locations of the 9 sets of unsteady solution samples used to generate the ROM are marked by the blue crosses

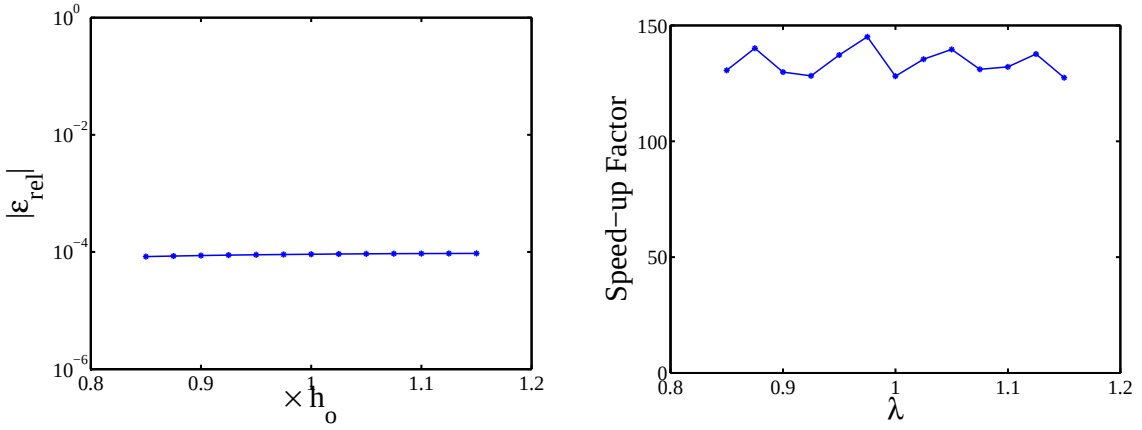

(a) Relative Error

(b) Speed-up

Figure 4-14: Relative error and speed-up over FOM in predicting flutter boundary using the modified POD-DEIM ROM ($K = 49$, $\hat{M} = 198$, $\hat{M}' = 5544$)

4.3.5 3-Parameter Case: Variable Dynamic Pressure λ, Plate Thickness h and Steady Angle of Attack α_o

In this section, the third input parameter is added to the system — the steady angle of attack α_o of the plate. It is allowed to vary between 0° and 0.3°. The plate thickness h is allowed to vary between h_o and $1.15h_o$. The range of variation for λ remains the same as the 2-parameter case, namely $\lambda \in [60, 120]$. Figure 4-15 shows the 3-D parameter space. The variations of the three input parameters are confined within the gray box.

To construct the ROM, 12 sets of unsteady snapshots are obtained by simulating the FOM until the convergence to a steady state or a stable limit cycle is achieved. The locations of these 12 sets of samples are marked by blue crosses on Figure 4-15. A tolerance on the relative omitted energy $\epsilon_u = 10^{-14}$ is imposed, resulting in the inclusion of $K = 55$ state POD modes. For the scalar-valued POD modes of the nonlinear term, $\epsilon_f = 10^{-9}$ is imposed. As a result, $\hat{M} = 160$ and $\hat{M}' = 4566$, requiring the evaluation of 15.8% of all the triangular elements in the online stage.

An α_o-sweep is performed at constant dynamic pressure ($\lambda = 110$) and plate thickness ($h = 1.05h_o$) in which both the FOM and ROM are solved at 11 equi-spaced α_o values in the interval $[0^\circ, 0.3^\circ]$ at increments of $\Delta\alpha_o = 0.03^\circ$. The results are plotted on Figure 4-16. Note that the response also exhibits Hopf-bifurcation with respect to the variations in α_o. For $\alpha_o > 0.185^\circ$, the solution damped out to a non-trivial equilibrium (static aeroelastic deflection), whereas for $\alpha_o < 0.185^\circ$, the solution oscillates on a stable limit cycle about a non-zero equilibrium position. For the equilibrium positions, the FOM and ROM results are in excellent agreement. For the LCO solutions, noticeable discrepancy for the maximum tip deflection exists between the FOM and ROM results at $\alpha_o = 0.18^\circ$ — the closest of the 11 test points to the bifurcation point, due to the long-time integration problem discussed in previous test cases. As shown on Figure 4-17(a), all other points are computed by the ROM at relative errors of $O(10^{-3})$. Note that the equilibrium position corresponding to $\alpha_o = 0^\circ$ appears to have a high relative error, which is due to the division by the

FOM result that is almost zero. The absolute error at this point is $O(10^{-7})$. The speed-up over FOM, as shown on Figure 4-17(b) is between 14 and 22 times.

Next, the ROM is applied to predict the flutter boundary at various α_o. Note that at increasing α_o values, the flutter boundary shifts towards higher dynamic pressures, forming a curved surface as shown on Figure 4-18. The flutter boundaries computed by the FOM and ROM are observed to be in good agreement within the parameter bounds represented by the gray box. Indeed, Figure 4-19(a) shows that for $\alpha_o \leq 0.2°$, the flutter boundaries are predicted with $O(10^{-3})$ relative error. The errors for large α_o cases are higher and the discrepancies between the two surfaces are observable on Figure 4-18. This is because the flutter points (λ^*) at higher α_o values are much higher than the maximum λ of 120 considered in constructing the ROM. As a result, when attempting to converge to these flutter points, the ROM must operate outside the pre-defined parameter bounds. The state and nonlinear terms at these points are less likely to be in the spans of their respective POD modes, giving rise to large approximation errors. The speed-up factors over the FOM for all α_o cases except for $\alpha_o \leq 0.3°$ are found to be between 12 and 14. The speed-up factors achieved by the largest α_o case is lower because it takes more iterations for these points to converge under the influence of high approximation errors. Note that in this case, unlike the 2-parameter case, the nonlinear equilibrium equations (4.54) and its ROM counterpart (4.76) must be solved at each iteration of the direct flutter computation. The online complexity depends not only on K but also on $\hat{M}$ and $\hat{M}'$. Consequently, the speed-up is similar to the bifurcation case involving time-integration.

Note that in this study, the maximum steady angle of attack considered is only 0.3°. The need to restrict to such a small range is mainly due to the thinness of the plate — 1/300-th of the length and the width of the plate. At larger α_o values, the plate deflections are too large for the linear supersonic theory in the aerodynamic forcing as well as the plate equations to be valid. If one uses a thicker plate, one may then widen the range of α_o and obtain characteristically similar responses in both bifurcation and flutter boundary as shown above. However, for thicker plates, the *absolute* tip displacements of the plate are again too large for the aerodynamic and

structural models to be valid. A more sophisticated aero-structural model is required to examine thicker plates with larger angles of attack.

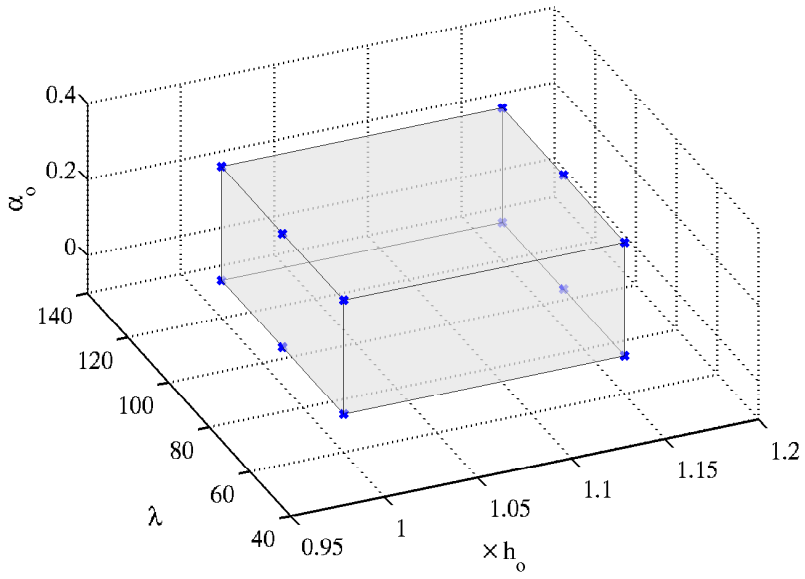

Figure 4-15: 3-D input parameter space. The locations of the 12 sets of unsteady solution samples used to generate the ROM are marked by the blue crosses

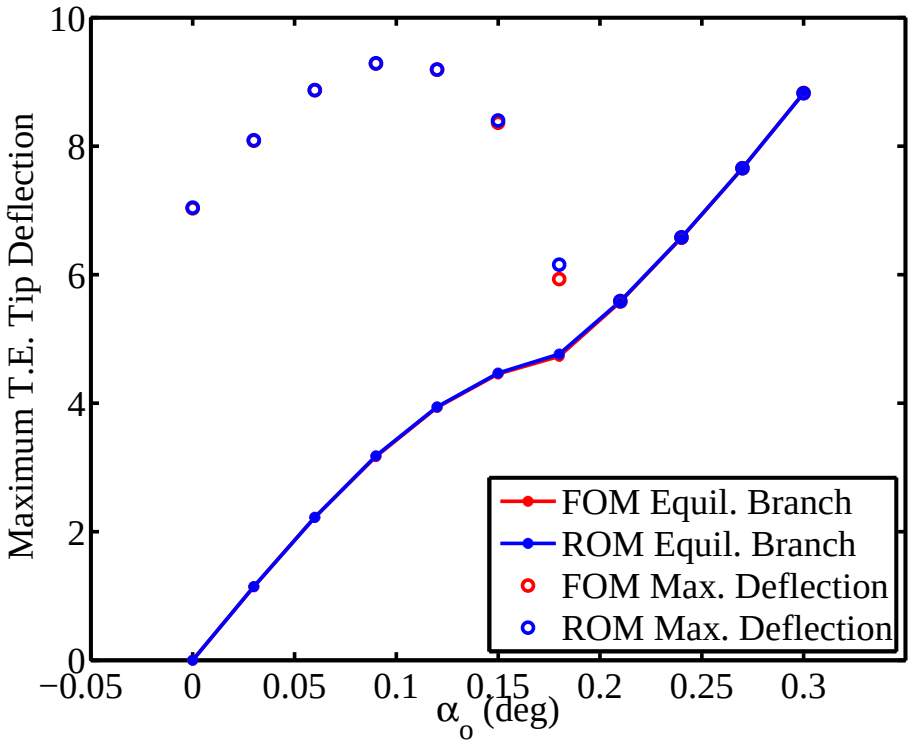

Figure 4-16: Comparison of bifurcation diagrams with respect to α_o at $\lambda = 110$ and $h = 1.05h_o$, computed using the FOM and the modified POD-DEIM ROM with $K = 55$, $\hat{M} = 160$ and $\hat{M}' = 4566$, via time-integrations

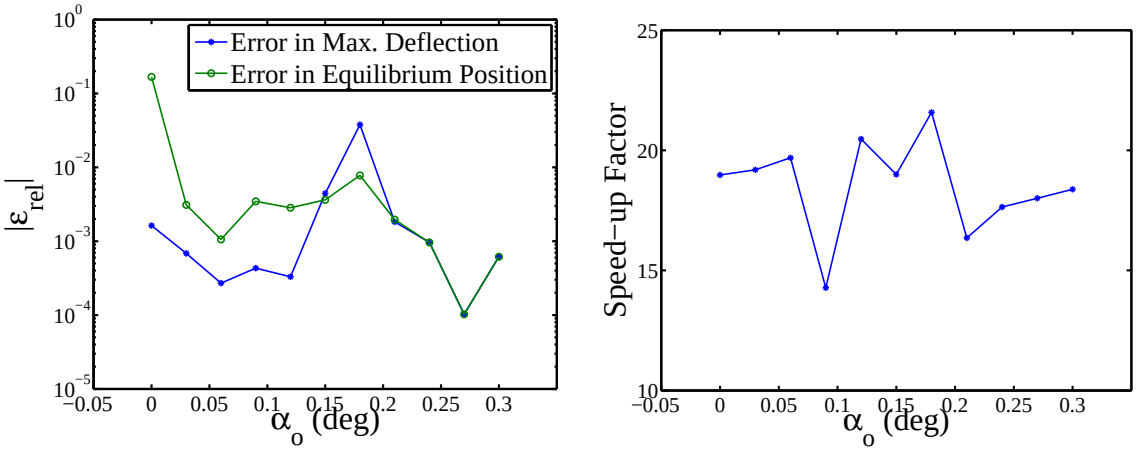

(a) Relative Error

(b) Speed-up

Figure 4-17: Relative error and speed-up over FOM in computing LCO amplitudes, using the modified POD-DEIM ROM with $K = 55$, $\hat{M} = 160$ and $\hat{M}' = 4566$

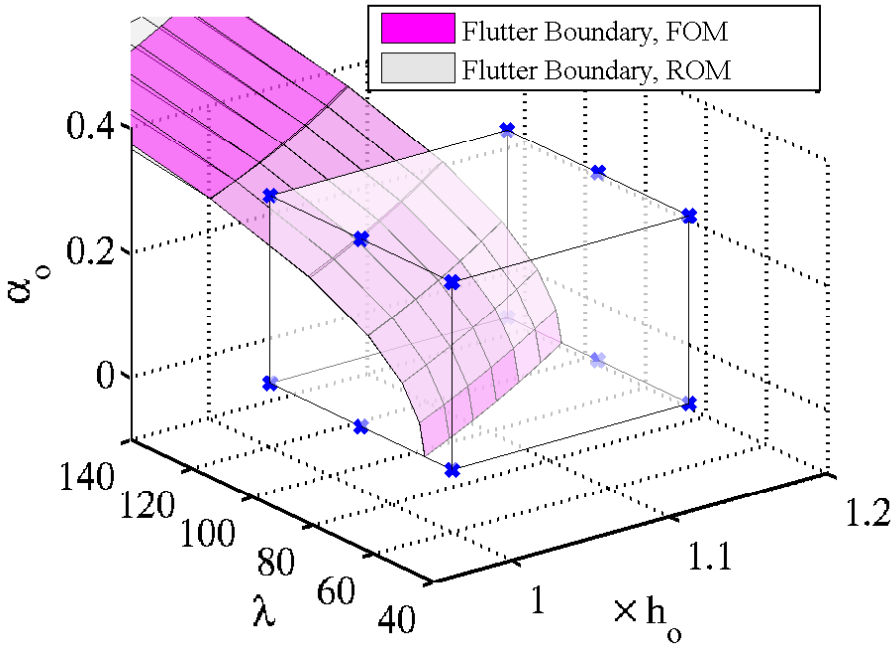

Figure 4-18: Comparison of flutter boundaries in the 3-D parameter space, computed using the FOM and the modified POD-DEIM ROM ($K = 55$, $\hat{M} = 160$ and $\hat{M}' = 4566$) via the direct flutter computations

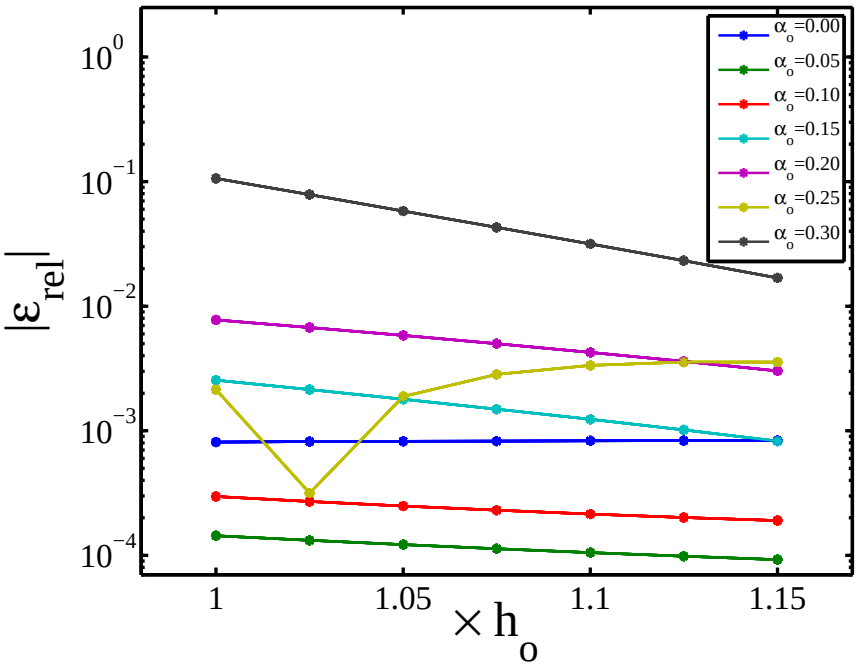

(a) Relative Error

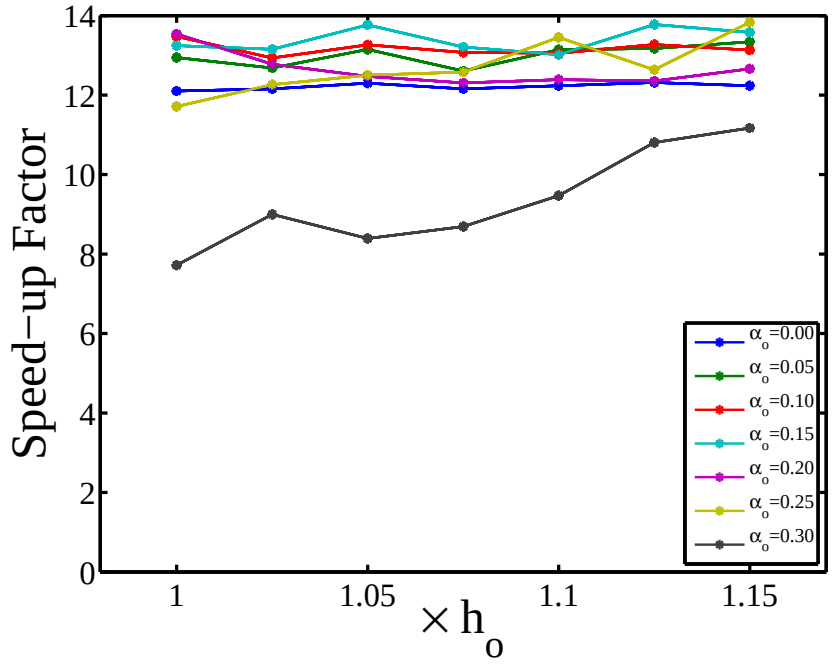

(b) Speed-up

Figure 4-19: Relative error and speed-up over FOM in predicting flutter boundaries at various α_o values using the modified POD-DEIM ROM ($K = 55$, $\hat{M} = 160$ and $\hat{M}' = 4566$)

Chapter 5

Conclusions and Future Work

5.1 Summary of Results and Contributions

The work presented in this thesis is focused on model order reduction for nonlinear dynamical systems with parametric uncertainties. In particular, an important class of such systems — one which exhibits limit cycle oscillations (LCO) is considered. LCO problems possess complex nonlinear dynamics such as autonomous periodic solutions and Hopf bifurcations which are known to be sensitive to input parameters. High-fidelity LCO simulations are typically a computationally intensive task owing to the large systems of nonlinear equations that must be solved at each time step and the long-time integrations required to fully establish the time-asymptotic system responses. Such challenges are intensified when the system is studied under a probabilistic setting, taking into account the effects of the uncertain input parameters.

The model reduction method used in this work is a projection-based approach, in which the proper orthogonal decomposition (POD) is used to derive the reduced basis while the discrete empirical interpolation method (DEIM) is employed to approximate the nonlinear term such that the repeated online evaluations of the reduced-order model (ROM) are independent of the full-order model (FOM) dimension. To address the new challenges introduced by the LCO-type nonlinear problems considered in this thesis (namely, vector-valued PDEs having highly oscillatory nonlinear terms with noncomponentwise dependence on the state), two modifications to the original

POD-DEIM methodology are proposed. The first involves the use of scalar-valued POD modes both for the state and the nonlinear term. The second replaces the pure interpolation of the DEIM approximation with a regression via over-sampling of the nonlinear term.

Both original and modified POD-DEIM methodologies are applied to model the LCO behaviour of a nonlinear tubular reactor problem with an uncertain Damköhler number. The results show that when the unknown variables are of approximately equal magnitudes, the ROMs constructed by both methodologies accurately predict the FOM response. In particular, uncertain dynamics over the entire range of variation of the Damköhler number are accurately characterized by the ROMs at relative errors of $O(10^{-4})$ via the bifurcation diagram, even though only two sets of samples, one at each end of the 1-D input parameter domain, are used in constructing the ROMs. Furthermore, the ROMs reduce the computational time for each unsteady simulation by two orders of magnitude from the FOM. In the case with disparate magnitudes among unknown variables, it is demonstrated that the ROM constructed by the modified POD-DEIM methodology using scalar-valued POD modes and DEIM oversampling is capable of maintaining its accuracy and speed-up while the original POD-DEIM ROM suffers significant degradation in accuracy due to its biase towards large-magnitude variables.

The second application considered in this work is the LCO of an aeroelastic system which consists of a nonlinear cantilevered plate in supersonic flow. This problem is challenging in that the nonlinear internal force term due to aerodynamic forcing is highly oscillatory in both space and time with noncomponentwise dependence on state. Furthermore, up to 3 uncertain input parameters are considered (dynamic pressure, plate thickness and steady angle of attack). The numerical results demonstrate that while the original POD-DEIM ROM requires such a large set of interpolation points that its efficiency is reduced to that of the POD-Galerkin approach, the modified POD-DEIM ROM yields accurate results with substantial speed-up over the FOM. In particular, the modified methodology is capable of predicting the LCO response and flutter boundary with relative errors of $O(10^{-4}) - O(10^{-3})$ and speed-up

factors between 10 to 40 over the FOM for all cases considered.

5.2 Future Work

A number of extensions of the POD-DEIM model reduction methodology presented in this thesis are envisioned to further improve its versatility and efficiency in addressing nonlinear dynamical problems.

Firstly, a more advanced sampling strategy in forming the snapshot matrices can be used in conjuction with the model reduction methodology developed here. In this work, uniform sampling is used in all test cases which is not necessarily optimal in that it does not concentrate sample points in important regions of the parameter space. For example, in the aeroelastic LCO test case, it is observed that the number of the requisite DEIM interpolation points to maintain satisfactory output accuracy of the ROM is driven by its poor performance in the high angle-of-attack region of the parameter space. Therefore, to improve the accuracy of the ROM, the placement of sample points should be biased towards this region. This can be achieved by replacing the uniform sampling with a more advance sampling technique such as the model-constrained sampling method proposed by Bui-Thanh et al. in [18] in which the computations for the sample locations in the parameter space are formulated as an optimization problem.

Secondly, the scalar-valued POD modes can be generalized to include multiple unknown variables (and the corresponding nonlinear terms). Currently, a set of scalar-valued POD modes is derived for each unknown variable. For systems with large numbers of unknowns, such as chemical reaction problems which may involve tens or even hundreds of species, having one set of POD modes for each unknown variable reduces the efficiency in both offline and online phases of the methodology. Instead, one may group the variables with similar orders of magnitude and use one scalar-valued POD basis for each of these groups. To that end, how to perform such 'clustering' without assuming prior knowledge of the full-order system is an important research question.

In addition, we note that the DEIM approximation is not a similarity transform in that the resultant reduced matrices do not preserve the stability properties of their full-order counterparts. In the aeroelastic LCO problem, although the tangent stiffness matrix of the FOM is positive definite (as it should be, since the plate is dynamically stable without aerodynamic forcing), it is observed that when insufficient number of DEIM interpolation points are used, the reduced tangent stiffness matrix fails to remain positive definite. This manifested in non-optimal search directions when the nonlinear system at each time level is solved by Newton's method and quickly results in convergence problems. Therefore, in addition to maximizing accuracy of snapshot approximations, the derivation of DEIM interpolation points should also be made with preserving the stability properties of the system in mind. To that effect, Petrov-Galerkin projection and the structure-preserving model reduction techniques presented by Carlberg et al. in [21] may be used in conjunction with the current methodology.

Finally, it is important to note that although appreciable reductions in computational times are achieved in the aeroelastic LCO problem, each unsteady evaluation of the ROM still requires several minutes on a dual-core (2.67GHz per core) desktop. This precludes the ROM from being used for probabilistic analyses with sampling-based uncertainty quantification (UQ) methods in which the model must be evaluated many thousands of times to obtain time-asymptotic statistics. Stochastic spectral methods using polynomial chaos expansion (PCE) constructs efficient representations of the solution in the random domain of the problem, fully replacing sampling-based UQ methods. Although the spectral expansion on each element of the state vector results in a much larger system of expansion coefficients to be solved forward in time, such computation only needs to be performed *once* before the time-dependent statistics can be recovered. In particular, Le Maître et al. [53] recently developed a PCE formulation with asynchronous time integration (A-PCE) which has been shown to be a promising technique in characterizing uncertain oscillatory dynamics. An interesting future direction to explore is the hybridization of the POD-DEIM and A-PCE methods whereby the spectral expansions of the A-PCE are

applied to the vector of reduced unknowns of the POD-DEIM ROM instead of the full state vector. Such hybrid would inherit the strength of A-PCE in that the expansion coefficients need only be solved once before essential time-dependent statistics can be extracted. At the same time, the resulting expansion of the system dimension is also likely to be moderate owing to the low-dimensional representation of the state achieved by the POD-DEIM.

Bibliography

[1] D. Amsallem and C. Farhat, *An interpolation method for adapting reduced-order models and application to aeroelasticity*, 46(7):18031813, 2008

[2] M. Allen and K. Maute, *Realiability-based shape optimization of structures undergoing fluid-structure interaction phenomena*, Computer Methods in Applied Mechanics and Engineering, 194(30):3472–3495, 2005

[3] H. Ashley, and G. Zartarian, *Piston Theory – A new aerodynamic tool for the aeroelastician*, Journal of the Aeronautical Sciences, 23(12):1109–1118, 1956

[4] P. Astrid, *Reduction of process simulation models: a proper orthogonal decomposition approach*, PhD thesis, Department of Electrical Engineering, Eindhoven University of Technology, November 2004.

[5] P. Astrid and S. Weiland, *On the construction of POD models from partial observations*, In CDC-ECC 05 44th IEEE Conference on Decision and Controland 2005 European Control Conference, pages 2272–2277, 2005.

[6] P. Astrid, S. Weiland, K. Willcox and T. Backx, *Missing point estimation in models described by proper orthogonal decomposition*, IEEE Transactions on Automatic Control, 53(10):2237–2251, 2008.

[7] D. Baker, *Means of compliance with Title 14 CFR, Part 23.629, Flutter*, Federal Aviation Administration, AC No:23.629-1B, 2004

[8] M. Barrault, Y. Maday, N.C. Nguyen and A.T. Patera, *An empirical interpolation method: application to efficient reduced-basis discretization of partial differential equations*, Comptes Rendus Mathematique, 339 (9): 667-672, 2004.

[9] T. Bechtold, M. Striebel, K. Mohaghegh and E. Maten, *Nonlinear model order reduction in nanoelectronics: combination of POD and TPWL*, Proceedings in Applied Mathematics and Mechanics, 8(1):10057–10060, 2008

[10] P.S. Beran, L.J. Huttsell, B.J. Buxton, C. Noll and G. Osswald, *Computational aeroelasticity techniques for viscous flow*, CEAS/AIAA/ICASE/NASA Langley International Forum for Aeroelasticity and Structural Dynamics, Williamsburg, VA, 1999

[11] P.S. Beran, D.J. Lucia, and C.L. Pettit, *Reduced-order modelling of limit-cycle oscillation for aeroelastic systems* , Journal of Fluids and Structures, 19, 575–590, 2004

[12] P.S. Beran, C.L. Pettit, and D. Millman, *Uncertainty quantification of limit-cycle oscillations*, Journal of Computational Physics, 217, 217–247, 2006

[13] M. Bergmann, L. Cordier and J. Brancher, *Optimal rotary control of the cylinder wake using proper orthogonal decomposition reduced-order model*, Physics of Fluids, 17, 2005

[14] P. Brenner and T. Breiten, *Krylov-subspace based model reduction of nonlinear circuit models using bilinear and quadratic-linear approximations*, Progress in Industrial Mathematics at ECMI 2010, Mathematics in Industry, 17(2):153–159, 2012

[15] M. Brøns, E.A. Christensen and J.N. Sorensen, *Evaluation of proper orthogonal decomposition-based decomposition techniques applied the parameter-dependent nonturbulent flows*, SIAM Journal on Scientific Computing, 21(4):1419-1434, 2000

[16] M. Brøns and J. Sturis, *Explosion of limit cycles and chaotic waves in a simple nonlinear chemical system*, Physical Review E, 64, 2001

[17] M. Buffoni and K. Willcox, *Projection-based model reduction for reacting flows*, 40th Fluid Dynamics Conference and Exhibit, June 2010, Chicago, Illinois, AIAA 2010-5008.

[18] T. Bui-Thanh, K. Willcox, and O. Ghattas, *Model reduction for large-scale systems with high-dimensional parametric input space*, SIAM Journal on Scientific Computing, 30(6):32703288, 2008.

[19] R.W. Bunton and C.M. Denegri Jr., *Limit cycle oscillation characteristics of fighter aircraft*, Journal of Aircraft, 37(5):916–918, 2000

[20] M. A. Cardoso, L. J. Durlofsky, and P. Sarma, *Development and application of reduced-order modeling procedures for subsurface flow simulation*, International Journal for Numerical Methods in Engineering, 77(9):1322–1350, 2009

[21] K. Carlberg, R. Tuminaro, and P. Boggs, *Efficient structure-preserving model reduction for nonlinear mechanical systems with application to structural dynamics*, 53rd AIAA/ASME/ASCE/AHS/ASC Structures, Structural Dynamics and Materials Conference, April 2012, Honolulu, Hawaii, AIAA 2012-1969

[22] M.P. Castanier, G. Ottarsson and C. Pierre, *A Reduced order modeling technique for mistuned bladed disks*, Journal of Vibration and Acoustics, 119(3):439447, 1997.

[23] S. Chaturantabut, *Nonlinear model reduction via discrete empirical interpolation*, Ph.D. Thesis, Department of Computational and Applied Mathematics, Rice University, 2011

[24] S. Chaturantabut and D. Sorensen, *Nonlinear model reduction via discrete empirical interpolation*, SIAM Journal of Scientific Computing, 32(5):2737–2764, 2010

[25] Y. Chen, *Model order reduction for nonlinear systems*, Masters thesis, Department of Mathematics, MIT, 1999

[26] F. Chinesta, A. Falco and M. Gonzalez, *Model reduction methods in option pricing*, CNRSENSAMESEM, IVIE Working Paper, 2006

[27] J. Chung and G.M. Hulbert, *A time integration algorithm for structural dynamics with improved numerical dissipation: the generalized-α method*, Journal of Applied Mechanics, 60:371–375, 1993

[28] M. Condon, G. Grahovski and R. Ivanov, *Balanced truncation of perturbative representations of nonlinear systems*, Proceedings 21st European Conference on Modelling and Simulation, 2007

[29] R. Cook, D. Malkus, M. Plesha and R. Witt, *Concepts and applications of finite element analysis*, Wiley, New York

[30] J. Croft, *Airbus Elevator Flutter: Annoying or Dangerous?*, Aviation Week and Space Technology, 155(9):41, 2001

[31] B. Danowsky, J. Chrstos, D. Klyde, C. Farhat and M. Brenner, *Evaluation of aeroelastic uncertainty analysis methods*, Journal of Aircraft, 47(5):1266–1273, 2010

[32] E. Dowell, *Nonlinear oscillations of a fluttering plate*, AIAA Journal, 4(7):1267–1275, 1966

[33] E. Dowell, J. Edwards and T. Strgnac, *Nonlinear Aeroelasticity*, Journal of Aircraft, 40(5):857–874, 2003

[34] E.H. Dowell, J.P. Thomas and K.C. Hall, *Transonic limit cycle oscillation analysis using reduced order aerodynamic models*, Journal of Fluids and Structures, 19, 17–27, 2004

[35] P. Feldmann and R.W. Freund, *Efficient linear circuit analysis by Pade approximation via the Lanczos process*, IEEE Transactions on Computer-Aided Design of Integrated Circuits and Systems, 14:639649, 1995.

[36] M. Frangos, Y. Marzouk, K. Willcox and B. van Bloemen Waanders, *Surrogate and reduced-order modeling: a comparison of approaches for large-scale statistical inverse problems*, Computational Methods for Large-Scale Inverse Problems and Quantification of Uncertainty, Wiley, 2010

[37] D. Galbally, K. Fidkowski, K. Willcox and O. Ghattas, *Non-linear model reduction for uncertainty quantification in large-scale inverse problems*, International Journal for Numerical Methods in Engineering, 81(12):15811608, 2010

[38] K. Gallivan, E. Grimme, and P. Van Dooren, *Pade approximation of large-scale dynamic systems with Lanczos methods*, In Proceedings of the 33rd IEEE Conference on Decision and Control, December 1994.

[39] D. Gratton, *Reduced-order, trajectory piecewise-linear models for nonlinear computational fluid dynamics*, Master's Thesis, Department of Aeronautics and Astronautics, MIT, 2004

[40] M.A. Grepl, Y. Maday, N.C. Nguyen, and A.T. Patera, *Efficient reduced-basis treatment of nonaffine and nonlinear partial differential equations*, Mathematical Modelling and Numerical Analysis, 41(3):575605, 2007

[41] E. Grimme, *Krylov projection methods for model reduction*, PhD thesis, Coordinated-Science Laboratory, University of Illinois at Urbana-Champaign, 1997.

[42] S. Gugercin and A. Antoulas, *A survey of model reduction by balanced truncation and some new results*, International Journal of Control 77, 748–766, 2004

[43] R. Heinemann and A. Poore, *Multiplicity, stability, and oscillatory dynamics of the tubular reactor*, Chemical Engineering Science, 36, 1411–1419, 1981

[44] M. Hinze, M. Kunkel, A. Steinbrecher and T. Stykel, *Model order reduction of coupled circuit-device systems*, International Journal for Numerical Methods in Engineering, 25:362377, 2012

[45] A. Hochman, B.N. Bond, and J.K. White, *A stabilized discrete empirical interpolation method for model reduction of electrical, thermal, and microelectromechanical systems*, Proceedings of the IEEE/ACM 48th Design Automation Conference, San Diego, CA, 6 pages, June 2011.

[46] P. Holmes, J.L. Lumley, and G. Berkooz, *Turbulence, coherent structures, dynamical systems and symmetry*, Cambridge University Press, Cambridge, UK, 1996.

[47] I. Kalashnikova and M.F. Barone, *Efficient non-linear proper orthogonal decomposition (POD)/Galerkin reduced order model with stable penalty enforcement of boundary conditions*, International Journal for Numerical Methods in Engineering, 00:1-28, 2011

[48] A.R. Kellems, S. Chaturantabut, D.C. Sorensen and S.J. Cox, *Morphologically accurate reduced order modeling of spiking neurons*, Journal of Computational Neuroscience, 28:477–494, 2010

[49] G. Kerschen, J. Golinval, A. Vakakis and L. Bergman, *The method of proper orthogonal decomposition for dynamical characterization and order reduction of mechanical systems: an overview*, Nonlinear Dynamics, 41, 147–169, 2005

[50] K. Kunisch and S. Volkwein, *Control of Burgers equation by reduced order approach using proper orthogonal decomposition*, Journal of Optimization Theory and Applications, 102, 345–371, 1999

[51] K. Kunisch and S. Volkwein, *Galerkin proper orthogonal decomposition methods for a general equation in fluid dynamics*, SIAM Journal of Numerical Analysis, 40(2):492–515, 2002

[52] S. Lall P. Krysl and J. E. Marsden, *dimensional model reduction in nonlinear finite element dynamics of solids and structures*, International Journal for Numerical Methods in Engineering, 51:479-504, 2001

[53] O. P. Le Maître, L. Mathelin, O. M. Knio, and M. Y. Hussaini, *Asynchronous time integration for polynomial chaos expansion of uncertain periodic dynamics*, Discrete and Continuous Dynamical Systems, 28 (2010), pp. 199–226.

[54] T. Lieu, C. Farhat and M. Lesoinne, *Adaptation of aeroelastic reduced-order models and applicatin to an F-16 configuration*, AIAA Journal, 45(6):1244–1269, 2007

[55] D.J. Lucia, P.S. Beran and P.I. King, *Reduced order modeling of an elastic panel in transonic flow*, Journal of Aircraft, 40(2):338–347, 2003

[56] Y. Maday, A. Patera and G. Turinici, *Global a priori convergence theory for reduced-basis approximations of single-parameter symmetric coercive elliptic partial differential equations*, Comptes Rendus Mathematique, 335 (3): 289-294, 2002

[57] B.C. Moore, *Principal component analysis in linear systems: controllability, observability, and model reduction*, IEEE Transactions on Automatic Control, AC-26(1):1731, 1981

[58] C.T. Mullis and R. A. Roberts, *Synthesis of minimum roundoff noise xed point digital lters*, IEEE Transactions on Circuits and Systems, CAS-23, 551562, 1976

[59] D. Murthy and R. Haftka, *Derivatives of eigenvalues and eigenvectors of a general complex matrix*, International Journal for Numerical Methods in Engineering, 26(2):293–311, 1988

[60] N.N. Newmark, *A method of computation for structural dynamics*, Journal of the Engineering Mechanic Division, Proceedings of the ASCE, 85:67–94, 1959

[61] N.C. Nguyen and J. Peraire, *An efficient reduced-order modeling approach for non-linear parametrized partial differential equations*, International Journal for Numerical Methods in Engineering, 76:27–55, 2008

[62] N.C. Nguyen, A.T. Pateraand J. Peraire, *A "best points" interpolation method for efficient approximation of parametrized functions*, IInternational Journal for Numerical Methods in Engineering, 73:521543, 2007.

[63] A. K. Noor and J. M. Peters, *Reduced basis technique for nonlinear analysis of structures*, AIAA Journal, 18(4):455–462, 1980

[64] P.S. Peterson, *The reduced-basis method for incompressible viscous flow calculations*, SIAM Journal of Scientific and Statistical Computing, 19:777–786, 1989

[65] C. Prudhomme, D. V. Rovas, K. Veroy, L. Machiels, Y. Maday, A. T. Patera and G. Turinici, *Reliable real-time solution of parametrized partial differential equations: Reduced-basis output bound methods*, Journal of Fluids Engineering, 124(1):7080, 2002

[66] C.L. Pettit, *Uncertainty quantification in aeroelasticity: recent results and research challenges*, Journal of Aircraft, 41(5):1217–1229, 2004

[67] M. Rewienski and J. White, *A trajectory piecewise-linear approach to model order reduction and fast simulation of nonlinear circuits and mircromachined devices*, Computer-Aided Design of Integrated Circuits and Systems, IEEE Transactions, 22(2):155–170, 2003

[68] R.H. Ricketts, *Structural testing for static failure, flutter, and other scary things*, NASA TM–84606, 1983

[69] C.W. Rowley, T. Colonius, and R.M. Murray, *Model reduction for compressible flows using POD and Galerkin projection*, Physica D. Nonlinear Phenomena, 189(1-2):115129, 2004.

[70] G. Rozza, *Shape design by optimal flow control and reduced basis technique: applications to bypass configurations in hemodynamics*, PhD thesis, MIT, 2005

[71] C. Runge, *Über empirische Funktionen und die Interpolation zwischen äquidistanten Ordinaten*, Zeitschrift für Mathematik und Physik 46, 1901

[72] M. Singer and W. Green, *UUsing adaptive proper orthogonal decomposition to solve the reaction-diffusion equation*, Applied Numerical Mathematics, 59(2):272–279, 2009

[73] L. Sirovich, *Turbulence and the dynamics of coherent structures. Part 1: Coherent structures*, Quarterly of Applied Mathematics, 45(3):561571, 1987

[74] B. Sportisse and R. Djouad, *Use of proper orthogonal decomposition for the reduction of atmospheric chemical kinetics*, Journal of Geophysics Research, 59(112), 2007

[75] B.K. Stanford and P.S. Beran, *Computational strategies for reliability-based structural optimization of aeroelastic limit cycle oscillations*, Structural and Multidisciplinary Optimization, 45, 83–99, 2012

[76] B.K. Stanford and P.S. Beran, *Minimum-mass panels under probabilistic aeroelastic flutter constraints*, Draft Paper, 2012

[77] A. Tan Yong Kwang, *Reduced basis methods for 2nd order wave equations: application to one dimensional seismic problem*, Master's Thesis, MIT, 2005

[78] D. Tang and E. Dowell, *Effects of angle of attack on nonlinear flutter of a delta wing*, Journal of Aircraft, 39(1):15–21, 2001

[79] K.T. Tang, W.R. Graham and J. Peraire, *Active flow control using a reduced order model and optimum control*, Fluid Dynamics Conference, 27th, New Orleans, LA, June 17-20, AIAA Paper 1996-1946, 1996

[80] J.P. Thomas, E.H. Dowell, K.C. Hall, and C.M. Denegri Jr., *An investigation of the sensitivity of F-16 ghter limit cycle oscillations to uncertainties*, 47th AIAA/ASCE/AHS/ASC Structures, Structural Dynamics, and Materials Conference, May 2006, AIAA 2006-1847.

[81] L.N. Trefethen and D. Bau III, *Numerical Linear Algebra*, SIAM, Philadelphia, 1997

[82] A. Vendl and H. Fassbender, *Missing point estimation for steady aerodynamic applications*, Proceedings in Applied Mathematics and Mechanics, 11, 839-840, 2011

[83] A. Verhoeven, *Redundancy reduction of IC models by multirate time-integration and model order reduction*, PhD thesis, Department of Mathematics and Computer Science, Eindhoven University of Technology, 2008.

[84] K. Veroy, C. Prudhomme and A.T. Patera, *Reduced-basis approximation of the viscous Burgers equation: rigorous a posteriori error bounds*, Comptes Rendus Mathematique, 337 (9): 619-624, 2003

[85] K. Veroy, D.V. Rovas and A.T. Patera, *A posteriori error estimation for reduced-basis approximation of parametrized elliptic coercive partial differential equations: 'convex inverse bound conditioners*, ESAIM: Control, Optimisation and Calculus of Variations, 8:10071028, 2002

[86] K. Willcox, *Reduced-order aerodynamic models for aeroelastic control of turbomachines*, PhD thesis, Department of Aeronautics and Astronautics, MIT, 2000

[87] D. Xiu, *Fast numerical methods for stochastic computations: a review*, Communications in Computational Physics, 5, 242–272, 2009

[88] D. Xiu, D. Lucor, C. Su and G. Karniadakis, *Stochastic modeling of owstructure interactions using generalized polynomial chaos*, Journal of Fluids Engineering, 124, 55–59, 2002